Spring 2018

Modeling and simulation of viscoplasticity, recrystallization, and softening of alloyed steel during hot rolling process

Xin Wang

Department: Mechanical and Aerospace Engineering

MODELING AND SIMULATION OF VISCOPLASTICITY, RECRYSTALLIZATION, AND SOFTENING OF ALLOYED STEEL DURING HOT ROLLING PROCESS

by

XIN WANG

A DISSERTATION

Presented to the Faculty of the Graduate School of the

MISSOURI UNIVERSITY OF SCIENCE AND TECHNOLOGY

In Partial Fulfillment of the Requirements for the Degree

DOCTOR OF PHILOSOPHY

in

MECHANICAL ENGINEERING

2018

Approved
K. Chandrashekhara, Advisor
Lokeswarappa Dharani
Xiaoping Du
David C. Van Aken
Ronald J. O'Malley

PUBLICATION DISSERTATION OPTION

This dissertation has been prepared in the form of four papers for publication as follows:

Paper I: pages 8-30 have been published in Journal of Materials Processing Technology

Paper II: pages 31-66 have been published in Journal of Materials Science

Paper III: pages 67-96 have been accepted by Journal of Steel Research International

Paper IV: pages 97-118 are intended for submission to Journal of Metallurgical and Materials Transactions B

ABSTRACT

Hot rolling is one of the most important and complex deformation processes in steel manufacturing and is essential to final product quality. The objective of this study is to investigate viscoplasticity, dynamic recrystallization, and static softening of alloyed metal during hot rolling process. Gleeble hot compression tests were performed to provide experimental stress-strain curves at different temperatures and strain rates. An inverse finite element analysis was performed to calibrate the experimental curves. Viscoplastic models including a Johnson-Cook (JC) model, a Zerilli-Armstrong (ZA) model, and a combined JC and ZA model were developed. Dynamic recrystallization behavior was investigated and modeled based on single hot compression test. Work hardening rate curve and dynamic recovery curve were modeled to calibrate the kinetics of dynamic recrystallization. Double hit tests were designed and performed and static softening model was developed at varying interpass time, pre-strain, temperature, and strain rate. Subroutines accounting for developed viscoplasticity, dynamic recrystallization, and static softening were developed and implemented into a three-dimensional finite element model of round bar hot rolling. The combined JC and ZA model demonstrated better agreement with experimental data than other traditional models. Dynamic recrystallization occurred throughout the round bar during hot rolling and is significantly influenced by the plastic strain and temperature. Static softening occurred rapidly in the beginning of interpass and then slowed down. Compared to rolling speed, rolling temperature demonstrated more significant influence on dynamic recrystallization and static softening during round bar hot rolling.

ACKNOWLEDGMENTS

I would like to express my sincere gratitude to Dr. K Chandrashekhara for his valuable guidance, assistance and encouragement during my graduate study at Missouri University of Science and Technology. I will never forget the countless hours of discussion he spent with us. Thank him for generous support of providing excellent working environment and teamwork. It has been a great pleasure working with him.

I also want to extend my genuine appreciation to my advisory committee members, Dr. Lokeswarappa Dharani, Dr. Xiaoping Du, Dr. David C. Van Aken, and Dr. Ronald J. O'Malley for their valuable time and advice.

Great appreciation goes to Dr. Haifeng Li and Dr. Zhen Huo for their important guidance and valuable training they provided prior to and during this research. I also wish to thank the assistance from my fellow colleagues: Dr. Simon Lekakh, Dr. Mario Buchely, and my research group members.

I would like to acknowledge the financial support from the Peaslee Steel Manufacturing Research Center at Missouri University of Science and Technology in the form of graduate research assistantship and teaching and guidance from Department of Mechanical and Aerospace Engineering at Missouri University of Science and Technology.

Finally, I wish to express my deepest gratitude to my wife Miao He, my family, and my friends for their company, understanding, and encouragement. Without their support, I would not be able to accomplish and fulfil my dreams.

TABLE OF CONTENTS

Page

LIST OF ILLUSTRATIONS

PAPER I Page

PAPER II

LIST OF TABLES

SECTION

1. INTRODUCTION

Hot rolling is an important steel manufacturing process operating above the non-recrystallization temperature to refine the microstructure, remove residual stress and strain, and improve thermo-mechanical properties of steel product. Due to high temperature above 900 °C, varying strain rate, and evolution of microstructure, hot rolling introduces complex phenomena including viscoplasticity, dynamic recrystallization, and static softening. These phenomena interact each other and control the macro and micro properties of steel product.

Viscoplastic deformation firstly occurs on steel products by rollers. Multiple parameters, such as plastic strain, strain rate, and temperature, demonstrate single and coupled effects on viscoplasticity of steel. Although plenty of viscoplastic models were proposed, it is necessary to revise current models since complex parameter effects. With viscoplastic deformation, recrystallization takes place to nucleate new grains and refined microstructure. Dynamic recrystallization occurs when the deformation exceeds the critical point. Dislocation density increases and new grains nucleate on the boundary of primary grains. Flow stress starts to exhibit softening behavior because of the refined microstructure. However, due to short compression time during hot rolling, the dynamic recrystallization usually is not completed and the newly nucleated grains are transferred to static softening. During static softening, new grains generated by dynamic recrystallization continues to grow and replace the large primary grains. Residual stress and strain are gradually removed by static softening since the dislocation density decreases and microstructure evolution. At

full static softening, the residual stress and strain is totally removed and equiaxed microstructure is achieved. These mechanisms cooperate with each other during hot rolling and it is necessary to develop comprehensive material models to investigate hot rolling.

2. LITERATURE REVIEW

Many constitutive models have been proposed to describe viscoplastic behavior of steel. These constitutive models are classified into three types: phenomenological models, physical models, and empirical models. The representative and mostly widely used phenomenological model is Johnson-Cook (JC) model [1] considering the effects of strain, strain rate, and temperature on flow stress. A lot of modified versions of Johnson-Cook model were proposed since the original JC model does not include the coupled effect of strain rate and temperature. Zhang et al. [2] proposed a modified Johnson-Cook model on Ni-based super alloy considering coupled effect of strain rate and temperature. Lin et al. [3] presented a modified Johnson-Cook model on a high-strength alloy steel considering combined effect of strain rate and temperature. The second type of constitutive model, physical model, is developed based on physical mechanism during deformation, which is different from phenomenological models. Zerilli–Armstrong (ZA) model [4] is widely used physical model based upon dislocation mechanisms. Similar to Johnson-Cook model, many revised versions of Zerilli–Armstrong model were proposed to represent complex stress-strain curves. A modified Zerilli–Armstrong model [5, 6] was developed to predict mass flow behavior of Ti-modified austenitic stainless steel. A combined Johnson-Cook model and Zerilli-Armstrong model [7] was proposed to predict stress-strain curves for a typical high strength steel.

In addition to viscoplastic models, modeling of dynamic recrystallization is an important topic during hot rolling and hot deformation. Different from the great diversity of viscoplastic models, the mathematic description of kinetics of dynamic recrystallization

is mainly Avrami Equation. Sellars [8] is one of pioneers on the study of modeling of recrystallization using Avrami kinetics and Jonas et al. [9] evaluated Avrami equation of varying steel grades and calculated kinetics of dynamic recrystallization. Based on Avrami kinetics, several steel grades were investigated on dynamic recrystallization. Dynamic recrystallization and microstructure evolution of 304 stainless steel [10] were modeled and simulated. A segmented model of dynamic recrystallization [11] of Ni-based super-alloy was developed. The effects of Mo [12] and Ti [13] on dynamic recrystallization of micro-alloyed steel were investigated and the results showed that Mo and Ti concentration impedes the progress of dynamic recrystallization. These literatures provide detailed information on dynamic recrystallization modeling used in the current study.

Similar to dynamic recrystallization occurring during deformation, static softening occurring mainly during interpass time was studied by many researchers. Avrami Equation is also used in static softening to investigate its effect on mechanical properties and microstructure [14, 15]. During interpass time, static softening includes static recrystallization and strain recovery [16, 17], working together to remove residual stress and strain and refine grain size. Due to limitation of traditional model of static softening, a revised static recrystallization model [18] was developed to represent complex stress-strain curves. Parametric study on static softening was performed by many researchers. Zhang et al. [19] studied static softening behavior using multiple hot deformation of alloyed aluminum and the results showed static softening of 5182 alloy is more sensitive to temperature and time than 1050 and 7075 alloys. Najafizadeh et al. [20] investigated postdynamic recrystallization behavior in stainless steel through double hit tests and the

results showed that fraction of the static softening significantly increases as pre-strain increases.

Besides mathematic material modeling, finite element method show critical effect in studying hot rolling. A shape rolling process [21] was modeled and investigated using finite element method and the non-uniform temperature distribution was simulated. Inverse finite element method [22] was used to simulate aluminum strip rolling. Blank size effect [23] on hot rolling of titanium alloy was investigated using finite element method. Mass flow behavior [24] of multi-pass hot rolling of micro-alloyed 38MnVS6 steel was developed and investigated using finite element analysis. Benasciutti et al. [25] developed a simplified finite element model considering both heating and cooling thermal load to predict thermal stresses during hot rolling. The nonlinear deformation of H-beam [26] during hot rolling was investigated using finite element method. Static softening simulation during hot rolling has also been modeled and simulated by many researchers. Static softening of bar hot rolling [27, 28] was simulated to predict the microstructure evolution. Multiple pass H-beam hot rolling [29], as well as hot strip rolling [30], was modeled to simulated recrystallization behavior, and a comprehensive modeling method [31] was proposed to study the static softening during hot rolling.

3. SCOPE AND OBJECTIVES

This dissertation comprises four papers corresponding to the following problems.

The first paper is titled “Inverse Finite Element Modeling of the Barreling Effect on Experimental Stress-Strain Curve for High Temperature Steel Compression Test.” In this paper, a methodology to correct experimental stress-strain curves for the barreling effect is presented. Gleeble hot compression testing was conducted to investigate material behavior for a low carbon structural steel over a range of temperatures (from 900°C to 1200°C) and strain rates (from $1s^{-1}$ to $30s^{-1}$). An inverse method combined with finite element analysis was developed to correct the experimental stress-strain curves for the observed barreling effect to obtain the actual stress-strain curves for the material. A comprehensive parametric study based on the revised stress-strain curves was performed to study barreling for a range of friction coefficients, temperatures, and strain rates.

The second paper is titled “Modeling of Mass Flow Behavior of Hot Rolled Low Alloy Steel based on Combined Johnson-Cook and Zerilli-Armstrong Model.” In this paper, Gleeble hot compression tests were carried out at high temperatures up to 1300 °C and varying strain rates for a medium carbon micro-alloyed steel. Based on experimental results, a combined JC and ZA model was introduced and calibrated through investigation of strain hardening, and the coupled effect of temperature and strain rate. An explicit subroutine of the proposed material model was coded and implemented into a finite element model simulating the industrial hot rolling. The simulated rolling torque was in good agreement with experimental data. Plastic strain and stress distributions were recorded to investigate nonlinear mass flow behavior of the steel bar.

The third paper is titled “Modeling and Simulation of Dynamic Recrystallization Behavior in Alloyed Steel 15V38 during Hot Rolling.” In this paper, single hot compression tests were performed at varying temperatures and strain rates to investigate dynamic recrystallization behavior of a 15V38 steel. Critical strains for initiation of dynamic recrystallization and peak strains were identified through the analysis of work hardening rate from the measured stress-strain results. Dynamic recrystallization was identified by the softening in the flow stress during plastic deformation and quantified as the difference between a calculated dynamic recovery curve and the measured stress-strain curve. Dynamic recrystallization was modeled using calculated critical strain, peak strain, Zener-Hollomon (Z) parameter, and volume fraction of dynamic recrystallization. Subroutines accounting for dynamic recrystallization were developed and implemented into a three-dimensional finite element model for hot rolling of a round bar.

The fourth paper is titled “Modeling and Simulation of Static Softening Behavior of Alloyed Steel Bar during Hot Rolling Process based on Modified Kinetics.” In this paper, double hit tests with varying temperature, strain rate, interpass time, and pre-strains were performed using Gleeble machine to investigate static softening behavior. Based on experimental results, a modified kinetics of static softening was developed to represent inerpass softening behavior during hot rolling. Explicit subroutines of developed static softening model was developed and implemented into a three-dimensional finite element model of steel bar hot rolling process. The static softening progress during hot rolling was simulated.

PAPER

I. INVERSE FINITE ELEMENT MODELING OF THE BARRELING EFFECT ON EXPERIMENTAL STRESS-STRAIN CURVE FOR HIGH TEMPERATURE STEEL COMPRESSION TEST

X. Wang, H. Li, and K. Chandrashekhara

Department of Mechanical and Aerospace Engineering

S. A. Rummel, S. Lekakh, D. C. Van Aken and R. J. O'Malley

Department of Materials Science and Engineering

Missouri University of Science and Technology, Rolla, MO 65409

ABSTRACT

Thermomechanical properties used in the modeling of steel forming processes that are determined using high temperature cylindrical coupon compression testing are subject to errors due to barreling of the test specimen. Barreling caused by the friction between specimen and platens reduces the accuracy of the mechanical property determination. In this study, Gleeble hot compression testing was conducted to investigate material behavior for a low carbon structural steel over a range of temperatures (from 900°C to 1200°C) and strain rates (from $1s^{-1}$ to $30s^{-1}$). An inverse method combined with finite element analysis was developed to correct the experimental stress-strain curves for the observed barreling effect to obtain the actual stress-strain curves for the material. In deformation simulations, the revised stress-strain curves produced barreling shape predictions that agreed well with

the barrel shapes observed in experiments. A comprehensive parametric study based on the revised stress-strain curves was performed to study barreling for a range of friction coefficients, temperatures, and strain rates. Results showed that the magnitude of barreling increases with increasing friction coefficient. For a specific friction coefficient, the magnitude of the barreling decreases with increasing temperature and varies non-linearly with strain rate.

1. INTRODUCTION

Compression tests are widely used to obtain elevated temperature mechanical properties for metals. Metal mechanics in the hot rolling process are complicated by high temperatures (up to 1300°C), strain rate, recrystallization and chemical composition sensitivity. Any change in these factors causes variations in mass flow behavior. Building a successful cylindrical compression test that accounts for these factors is critical, as it is a requirement for accurate simulation of comprehensive hot forming processes. Among these factors, barreling during cylinder compression poses a significant challenge to acquire the accurate material models needed for subsequent finite element analysis. Traditional methods used in calculating material properties from Gleeble compression tests do not account for the effects of non-uniform deformation. Experimental stress-strain data obtained from a barrel shaped specimen differs from the actual stress-strain curve obtained under a frictionless situation without barreling.

Initial dimensions of the compression specimen are represented by height (H), and diameter (D) (Fig. 1a). Barreling (Fig. 1b) occurs during uniaxial compression testing. The

barreling shape parameters include top and bottom surface diameter (d_{min}), the maximum diameter in barreling area (d_{max}), and specimen height after compression (h).

Barreling occurs due to friction between platens and specimen, causing a triaxial stress state, which differs from the ideal uniaxial stress condition. The experimental stress-strain curve calculated from a barreling specimen deviates from the actual stress-strain curve (Fig. 1c), which is based on ideal uniaxial stress conditions. Therefore, it is necessary to study the barreling effect on experimental stress-strain curves and correct these experiment results for the barreling condition. Unfortunately, friction between the platens and the specimen cannot be eliminated during hot compression testing to obtain the actual material properties. Finite element analysis (FEA) is necessary to correct for the barreling effect observed in high temperature compression testing.

Many researchers have investigated the barreling effect in compression tests using cylindrical specimens. Deviation of stress-strain curves under different barreling conditions is a prevalent topic in this research area. Martinez et al. [1] studied the barreling effect during compression test of alloy 2117-T4 at room temperatures (20°C-40°C) and quasi-static strain rates (10^{-3} s^{-1}-10^{-2} s^{-1}). Load-displacement curves under different deformation conditions were compared and concluded that material is not sensitive to studied range of temperature and strain rate. However, they did not study barreling at high temperatures and higher strain rates. Charkas et al. [2] proposed an inverse method to correct the local material response during finite element analysis, effectively increasing simulation accuracy of highly stressed element. Rasti et al. [3] used a finite element method to study the relationship between barreling shape and the parameters of their material model based on AISI 304 stainless steel. Chen and Chen [4] proposed a mathematical

method to calculate effective stress and effective strain of barreled specimen during hot compression process. However, effects of temperature and strain rate on barreled specimens were not considered in these literatures. Narayanasamy and Murthy [5] developed a relationship between barreling radius and applied load using solid cylinder compression of AISI 5120. In a more recent study [6], barreling effects on stress and strain distributions were studied by cold upset forming of magnesium alloy ZM-21 cylinders. Malayappan and Esakkimuthu [7] studied barreling shape during compression testing of pure aluminum and proposed a mathematical expression of barreling radius in an aluminum compression test. However, these literatures emphasized on barreling shape, lack of study of barreling effect on experimental results. Hervas et al. [8] investigated complex strain distributions in ductile cast iron compression testing, which included the effects of barreling. Their results show that the aspect ratio of graphite nodules in the iron could be used to predict local strains. Bao and Wierzbicki [9] conducted cylinder compression tests using Aluminum alloy 2024-T351 specimens of different height/diameter ratios. With increasing height/diameter ratio, the stress-strain curves converged to a stable state, which is assumed to be the actual stress-strain curve. In the previous studies, few researchers performed barreling effect on actual experimental data at high temperature and varying strain rate, at which high barreling shape is involved and has significant influence on experimentally measured stress-strain curves.

Friction between the specimen and platens is another widely studied topic by researchers. Ebrahimi and Najafizadeh [10] investigated the effect of friction on barreling shape during both cold and hot compression tests of Ti-IF steel, and proposed a mathematical relationship between barreling shape and the average friction factor. They

concluded that the maximum difference in flow stress under different friction conditions was approximately 8%. Li et al. [11] studied the barreling effect of IHS38MSV steel in an equivalent strain range, 0 to 1.8 using both experimental and finite element methods. Results showed that upper bound analysis of the friction condition during compression test is not accurate for large strains (>0.55). Yao et al. [12] developed an empirical model to predict the relationship between barreling factor and friction coefficient based on CuZn40 brass. A convenient expression relating the effect of friction to barreling shape for room temperature compression was proposed. On the other hand, Li et al. [13] studied the effect of friction in a hot compression test (800°C -1200°C) and concluded that the top radius of specimen after compression was affected significantly by friction. Based on these studies, Ebrahimi's equation is widely adopted and verified by researchers, providing an effective method to predict friction coefficient.

In the current study, a methodology to correct experimental stress-strain curves for the barreling effect is presented. The effect of increased temperatures as well as varying strain rates is also examined. Material testing was performed using Gleeble hot compression test at various strain rates and temperatures. Experimental stress-strain curves obtained from Gleeble testing were evaluated and revised stress-strain curves were obtained. A comprehensive parametric study was performed to study the effects of varying friction coefficients, temperatures, and strain rates on the barreling observed during compression testing.

2. EXPERIMENTS

A low carbon structural steel (C 0.075%, Mn 0.9%, Nb 0.016%, V 0.005%, Si 0.26%, Cr 0.11%) was used in the current study. Specimens (15 mm height and 10 mm diameter) for compression testing were machined from as-casted steel product. To investigate the effects of varying temperatures and strain rates on barreling and material properties, hot compression tests were performed at different temperatures (900°C, 1000°C, 1100°C and 1200°C) and strain rates ($1s^{-1}$, $5s^{-1}$, $15s^{-1}$, and $30s^{-1}$). Each combination was replicated three times, and a total of 48 specimens were tested. Compression tests at elevated temperatures were performed using a Gleeble thermo-mechanical tester. The experimental plan for hot compression test is shown and Fig. 2.

Specimens were first heated up to 1300°C at a rate of 260°C/min, and held for 3 minutes for austenitizing. The temperature of specimens was then lowered to the desired test temperature. After a brief holding period of 2 minutes, the compression test was performed. Tantalum foil with nickel paste was used to minimize the friction between platens and specimen. After compression, the specimen is cooled by water cooling. The raw Gleeble test results with experimental noise are plotted in Fig. 3. Smooth process was performed on these raw stress-strain curves to remove noise and provide material model for finite element analysis.

3. FINITE ELEMENT MODELING AND INVERSE METHOD

A nonlinear thermo-mechanical finite element model was built to investigate the effect of barreling. Triaxial stress distribution occurs due to friction between platen and specimen, and general three-dimensional analysis is used instead of axi-symmetric analysis. The governing equation for thermo-mechanical analysis can be written as:

$$[M^e]\{\ddot{\Delta}^e\} + [K^e]\{\Delta^e\} = \{F_M^e\} + \{F_T^e\} \quad (1)$$

where $[M^e]$ is mass matrix, $[K^e]$ is the stiffness matrix, and $\{F_M^e\}$ and $\{F_T^e\}$ are mechanical and thermal loadings respectively. Heat transfer during compression was also considered to simulate the Gleeble hot compression process. The formulation for heat transfer is expressed as:

$$[C_T^e]\{\dot{\theta}^e\} + [K_T^e]\{\theta^e\} = \{Q^e\} \quad (2)$$

where $[C_T^e]$ is specific heat capacity matrix, $[K_T^e]$ is conductivity matrix, and $\{Q^e\}$ is the external flux vector. The software package, ABAQUS 6.12, was used to build this finite element model. A cylindrical specimen model was built as a 3D isotropic cylinder with 15mm height and 10mm diameter. Two compression platens were modeled as 2D rigid plates. Eight-node deformable hexahedron element, C3D8R, was used to mesh the cylinder and the discrete rigid element, R3D4 was used to mesh the platens (Fig. 4).

Friction between each platen and the specimen was developed in the finite element model. Because of large deformation, both of sliding and sticking occurred between platen and specimen. A Coulomb's friction law used in current finite element model is defined as:

$$\tau = \begin{cases} \mu * p & when\ \tau < \tau_{yield} \\ \tau_{yield} & when\ \tau > \tau_{yield} \end{cases} \quad (3)$$

where τ is critical shear stress, τ_{yield} is yield shear stress, μ is friction coefficient, and p is contact pressure.

During high temperature compression test, it is very difficult to measure friction coefficient or friction force. The empirical friction coefficient at high temperature is around 0.3 to 0.6. To more accurately model the friction, an analytical method based on barreling shape is used to calculate the friction coefficient [10]:

$$\mu = m/\sqrt{3} \tag{4}$$

$$m = \frac{(r/h)b}{(4/\sqrt{3})-(2b/3\sqrt{3})} \tag{5}$$

where m is average friction factor, r is average radius of cylinder after compression, $r = r_0\sqrt{\frac{H}{h}}$, r_0 is initial radius of cylinder, H is initial height of cylinder, h is height of cylinder after compression, $b = 4\frac{\Delta r}{r}\frac{h}{\Delta H}$, ΔH is reduction in height, and Δr is difference between maximum radius and minimum radius. The friction coefficients of four specimens were calculated as 0.374, 0.365, 0.366, and 0.386 respectively. Average friction coefficient was set as 0.375 for these four specimens in finite element model.

The Gleeble hot compression test was simulated using a finite element model. For each specimen, both friction and frictionless conditions were simulated. Reaction force (P) and displacement (Δl) of platen were recorded in the finite element simulation. True strain, ϵ, and true stress, σ, were obtained by Eq. 6 and 7:

$$\epsilon = \ln(1 + \Delta l/H) \tag{6}$$

$$\sigma = 4\,P/\pi d^2\,(1 + \Delta l/H) \tag{7}$$

where d is initial diameter, and H is initial height of cylinder. An inverse method combined with finite element analysis (FEA) was applied to modify the experimental stress-strain

curves. An initial finite element model was built using the experimental stress-strain curves obtained from Gleeble tests and the hot compression process for each cylindrical specimen was simulated. Due to the effect of barreling, the simulated stress-strain curve differs from the experimental stress-strain curve. The initial error was determined from difference between the simulated stress-strain curve and experimental stress-strain curve. The error refined the input for the next run of finite element simulation. The material model is then modified to minimize the difference between simulated results and experimental results. This process was iterated until the coefficient of determination (R^2) between simulated stress-strain curve and experimental stress-strain curve was greater than 0.99. The schematic of this process is shown in Fig. 5.

4. RESULTS AND DISCUSSION

4.1 INVERSE FINITE ELEMENT ANALYSIS

Four tested specimens showing the typical barreled shape and one untested specimen are shown in Fig. 6. Since the analyzed material properties in this study are used for simulation of hot rolling process, the hot rolling conditions become research focus. The hot rolling temperature is 1000°C-1200°C, and strain rate is up to 50 s^{-1}. Selected specimens are at temperature 1000°C-1200°C and relatively high strain rate 15 s^{-1}-30 s^{-1} to avoid significant dynamic recrystallization. Due to the friction between platens and specimen, barreling is visible on the tested specimens. The shape of each specimen after hot compression testing was recorded, including top and bottom surface diameter (d_{min}), the maximum diameter in barreling area (d_{max}), and specimen height (h) after compression.

Dimensions, d_{max} and h, of these specimens were measured five times using a micrometer with a resolution of 0.001 inch (0.0254 mm). Dimension d_{min} was measured from specimen photographs using ImageJ software package. Dimensions of specimens 1-4 are shown in Table 1.

Ebrahimi and Najafizadeh [10] showed similar deformed specimen with different friction conditions and concluded that the difference between stress-strain curves with different friction conditions is approximately 8% based on theoretical analysis. However, it is difficult to represent this complex triaxial compression using pure analytical calculation with assumption and simplification. Finite element method shows advantage and can perform the barreling effect study under different friction conditions. Simulated equivalent plastic strain distributions of specimen 1 are plotted in Fig. 7. The frictionless situation shown in Fig. 7a, specimen 1 was deformed uniformly, showing ideal uniaxial strain distribution. On the other hand, for the friction condition shown in Fig. 7b, barreling is visible and a triaxial strain state is observed. Simulated stress-strain curves were calculated and compared in Fig. 7(c). In the frictionless condition, the simulated stress-strain curve was similar to the input material properties of FEA, which means that if friction is eliminated in practical hot compression test, the experimental stress-strain curve based on platen reacting force and displacement will be similar to actual stress-strain curve. For condition with friction, the simulated stress-strain curve deviates from the input material properties of FEA, proving that experimental stress-strain curve with barreling effect differs from actual stress-strain curve.

Charkas et al. [2] proposed inverse finite element method to effectively recover local material behavior by correcting load-displacement response of nodes during single

simulation process. Based on this method, inverse analysis was extended to revise input material properties during multiple simulation processes. Inverse finite element analysis results for specimen 1 are shown in Fig. 8(a). A revised stress-strain curve was calculated by iteration of the inverse method. Using this stress-strain curve as input of finite element model, the simulated stress-strain curve is shown to be close to the experimental stress-strain curve (R^2>0.99). Therefore, this revised stress-strain curve of FEA input is expected to accurately represent the actual stress-strain curve of the material. The simulated barreling shape based on the revised stress-strain curve and the actual barreling shape are shown in Fig. 8b and 8c. The simulated d_{max} (14.542 mm) based on revised stress-strain curve is close to actual d_{max} (14.887 mm).

4.2 REVISED STRESS-STRAIN CURVES

Experimental stress-strain curves were revised based on inverse finite element analyses (Fig. 9). The solid lines and dashed lines represent experimental stress-strain curves and revised stress-strain curves respectively. All dashed lines are lower than corresponding solid lines, due to friction between platen and specimen. The stress deviation between solid lines and dashed lines at low temperature is larger than at high temperature, and strain rate has relatively small effect on stress deviation. Inverse finite element analysis provides an effective method to revise experimental data to determine the actual material properties, which describes material flow behavior more accurately. Comparing to 8% difference in Ebrahimi's study [10], the differences between experimental and revised stress-strain curves in the current study vary from 2.5% to 7.5% at different temperature and strain rate.

4.3 PARAMETRIC STUDY RESULTS

A comprehensive parametric study was performed using inverse finite element analysis to investigate barreling effect on deviation between experimental stress-strain curve and actual stress-strain curve. The input material properties of the finite element model are the revised stress-strain curves plotted in Fig. 9. The parameters include friction coefficient (0, 0.125, 0.25, 0.375, and 0.5), temperature (900°C, 1000°C, 1100°C, and 1200°C), and strain rate ($1s^{-1}$, $5s^{-1}$, $15s^{-1}$, and $30s^{-1}$). Eighty hot compression simulation cases were performed. The flow stress is recorded at strain 0.15 (Fig. 10) where the stress deviation is visible and distinguishable among different parametric conditions. In the current study, material is sensitive to strain rate range 1 s^{-1} to 30 s^{-1} and high temperature range 900°C to 1200°C, comparing to the statement [1] that material is insensitive to low strain rate range 10^{-3} s^{-1} to 10^{-1} s^{-1} and room temperature range 20°C to 40°C.

4.3.1 Friction Effect. Friction is the main factor resulting in barreling during hot compression test. Flow stress at 0 friction coefficient in Fig. 10 is the actual material property and serves as the baseline for comparison. As friction coefficient increases, the flow stress increases proportionally with friction coefficient at constant temperature and strain rate, and reaches maximum at friction coefficient 0.5. Barreling effect can be represented by the differences of the flow stresses:

$$\text{Barreling Effect} = \sigma(\mu_i, T_i, \dot{\varepsilon}_i) - \sigma(\mu_0, T_i, \dot{\varepsilon}_i) \quad (8)$$

where σ is the flow stress, μ_i is friction coefficient, T_i is temperature, $\dot{\varepsilon}_i$ is strain rate, and μ_0 is frictionless condition. $\sigma(\mu_0, T_i, \dot{\varepsilon}_i)$ stands for actual material properties. Barreling was then calculated based on Fig. 10, and discussed in following sections.

4.3.2 Temperature Effect. The effect of temperature on barreling is shown in Fig. 11. At constant strain rate and friction coefficient, barreling effect decreases as temperature increases from 900°C to 1200°C. Temperature shows a uniformly negative relationship with barreling effect at all friction coefficients and strain rates. This can be due to the softening of material at elevated temperatures, which increases material flow behavior. Also, the effect of friction on barreling is smaller at elevated temperature. The effects of friction on material flow between platen and specimen is reduced by material softening.

4.3.3 Strain Rate Effect. The influence of strain rate on barreling is shown in Fig. 12. Unlike the temperature softening effect, the strain rate hardening effects on stress-strain curve is not uniform. At constant friction coefficient and temperature, barreling increases when strain rate is increased from $1s^{-1}$ to $5s^{-1}$ due to strain hardening. The softening of stress-strain curves mainly occurs from strain rate $5s^{-1}$ to $15s^{-1}$ and $15s^{-1}$ to $30s^{-1}$. The difference between experimental stress-strain curves and actual stress-strain curve is maximum at strain rates of $5s^{-1}$ and $15s^{-1}$.

5. CONCLUSION

In this paper, Gleeble hot compression tests were conducted to obtain experimental stress-strain curves under varying temperatures and strain rates. Barreling of the specimen during hot compression testing results in an experimental stress-strain curve that differs from actual stress-strain curve. An inverse method combined with finite element analysis was used to correct the experimental stress-strain curves for the barreling, and a comprehensive parametric study was performed to study the barreling effect. Revised

stress-strain curves were calculated based on inverse finite element analysis. It was found that inverse finite element analysis is an effective method to modify the experimental stress-strain curve to minimize errors from barreling on material properties. A parametric study was performed in order to investigate the effect of varying friction coefficient, temperature and strain rates. It was found that the friction coefficient has a significant effect on barreling effect. Barreling effect increases as friction coefficient increases. However, an increase in temperature reduces the deviation of experimental results from actual stress-strain curve due to the temperature softening effect. Strain rate has a complex influence on barreling effect. The barreling effect increases when strain rate is increased from $1s^{-1}$ to $5s^{-1}$ due to strain hardening. When strain rates are increased beyond $15s^{-1}$, barreling effect decreases. This study of the barreling effect on experimental stress-strain curves can be used to develop accurate material models for hot working simulation.

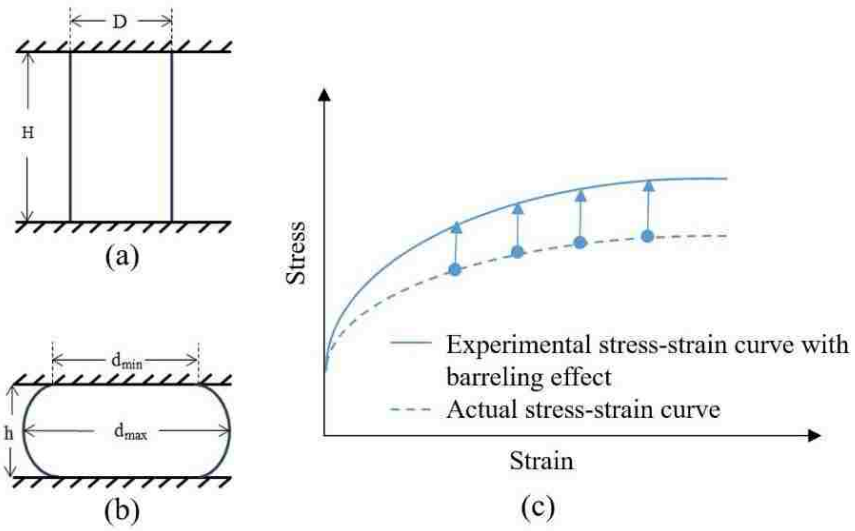

Fig. 1. (a) Dimension of cylinder before compression, (b) dimension of cylinder after compression, and (c) barreling effect on stress-strain curve

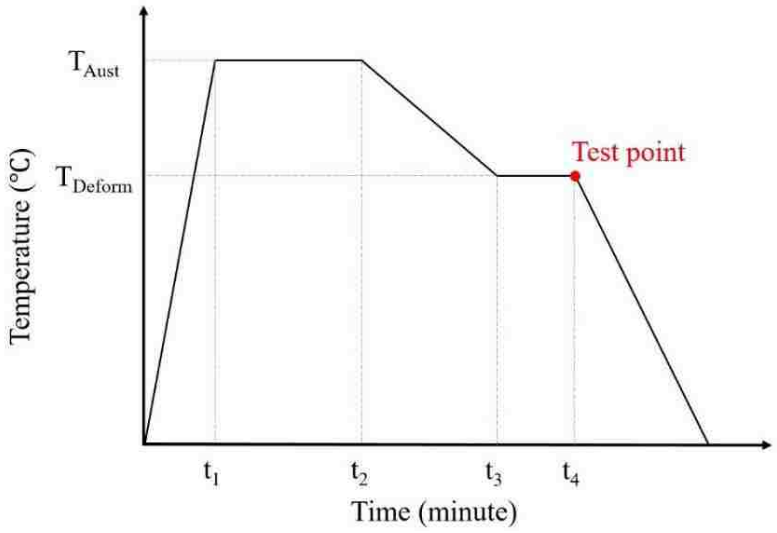

Fig. 2. Test profile for Gleeble hot compression test

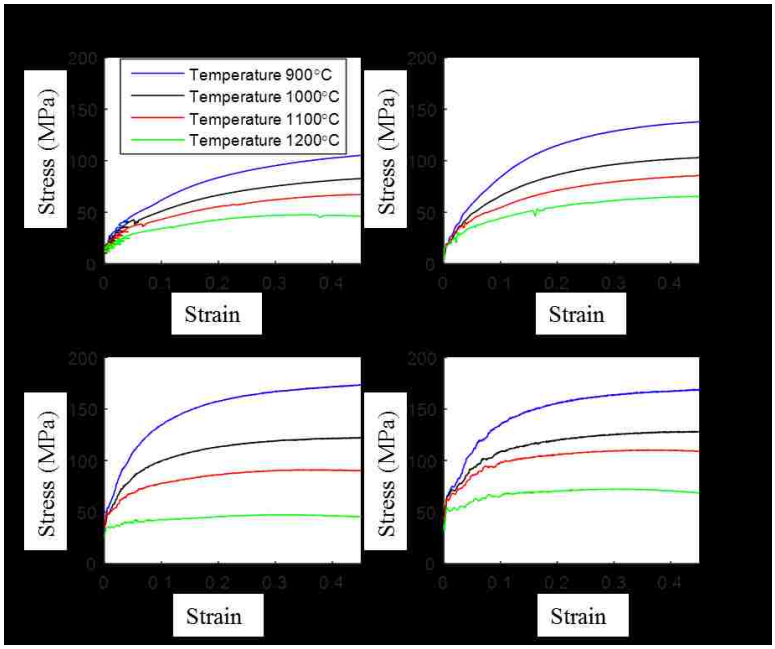

Fig. 3. Experimental stress-strain curves under varying temperatures and strain rates

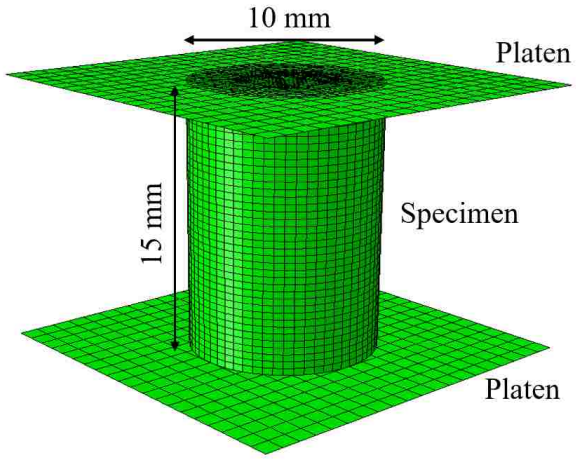

Fig. 4. Finite element model for Gleeble hot compression test

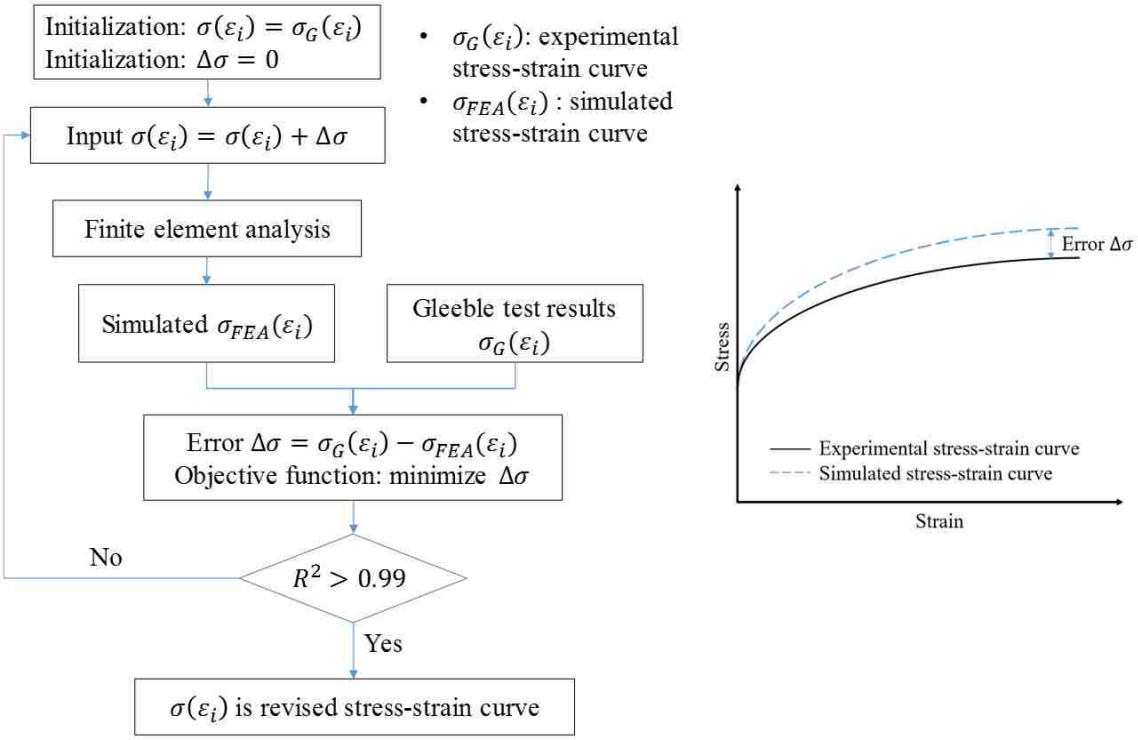

Fig. 5. Schematic of inverse method combined with FEA

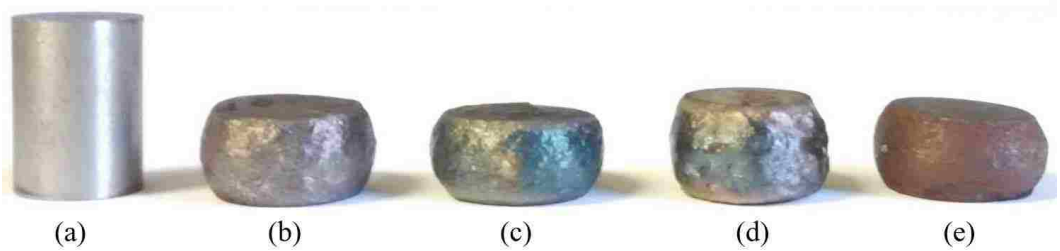

Fig. 6. Barreling shape after Gleeble hot compression tests of (a) initial specimen before compression (b) specimen 1 under 1000°C and $15s^{-1}$ (c) specimen 2 under 1100°C and $15s^{-1}$ (d) specimen 3 under 1100°C and $30s^{-1}$ (e) specimen 4 under 1200°C and $15s^{-1}$

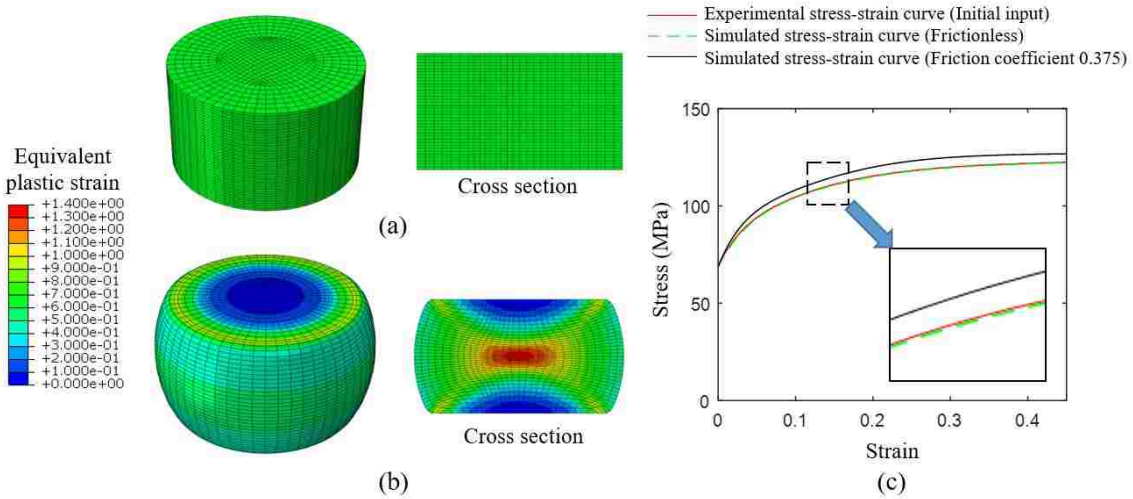

Fig. 7. (a) Simulation results of specimen 1 at frictionless condition, (b) friction coefficient 0.375, and (c) corresponding simulated stress-strain curves

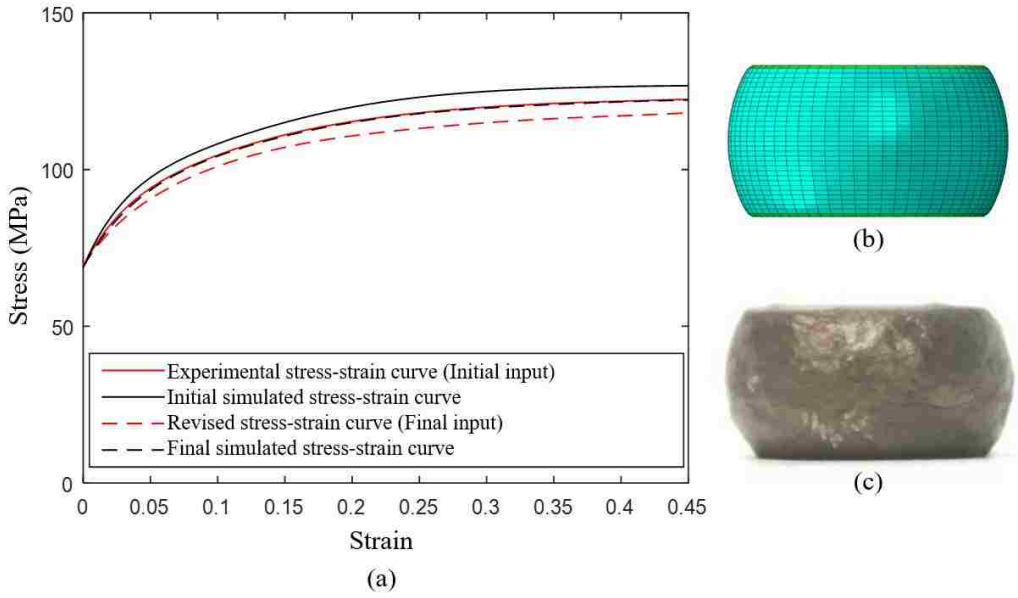

Fig. 8. (a) Inverse finite element analysis results of specimen 1, (b) simulated barreling shape using revised stress-strain curve, and (c) actual barreling shape

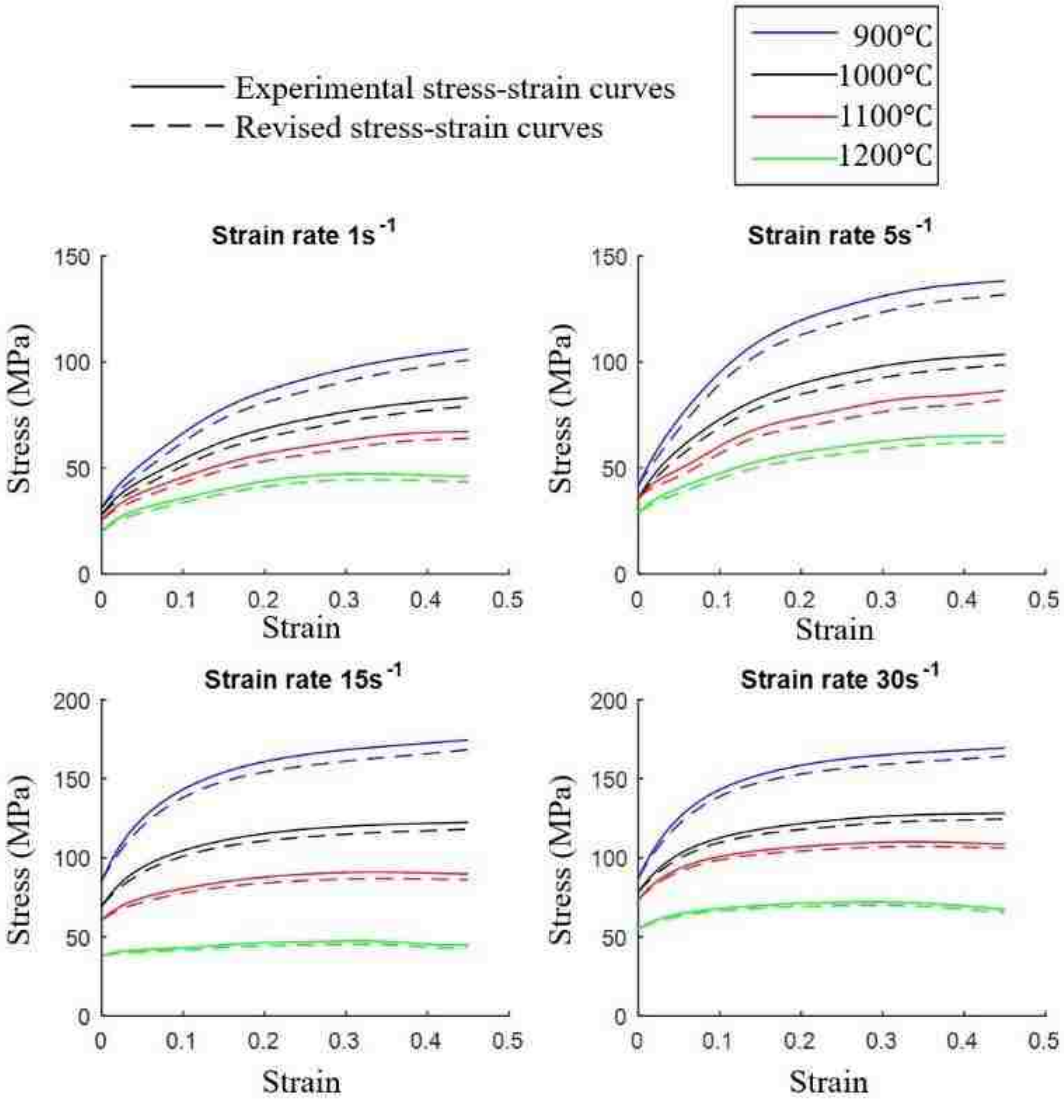

Fig. 9. Revised stress-strain curves using inverse finite element analysis

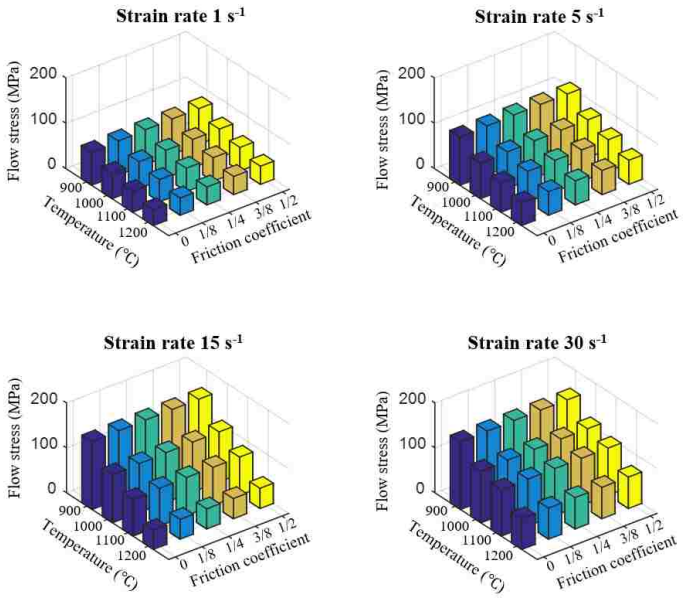

Fig. 10. Flow stress at different friction coefficients, temperatures and strain rates

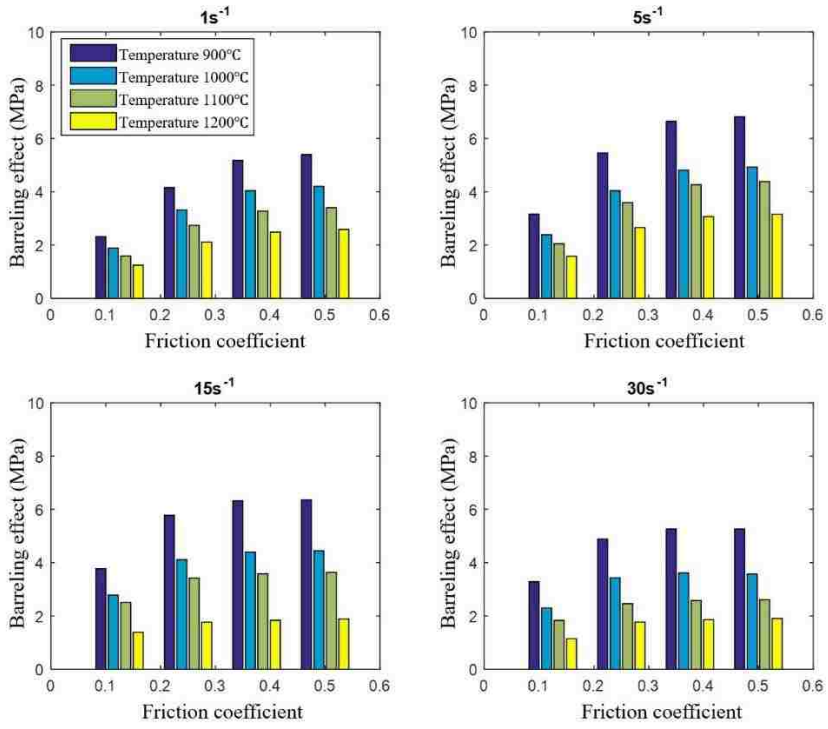

Fig. 11. Temperature effect on barreling effect

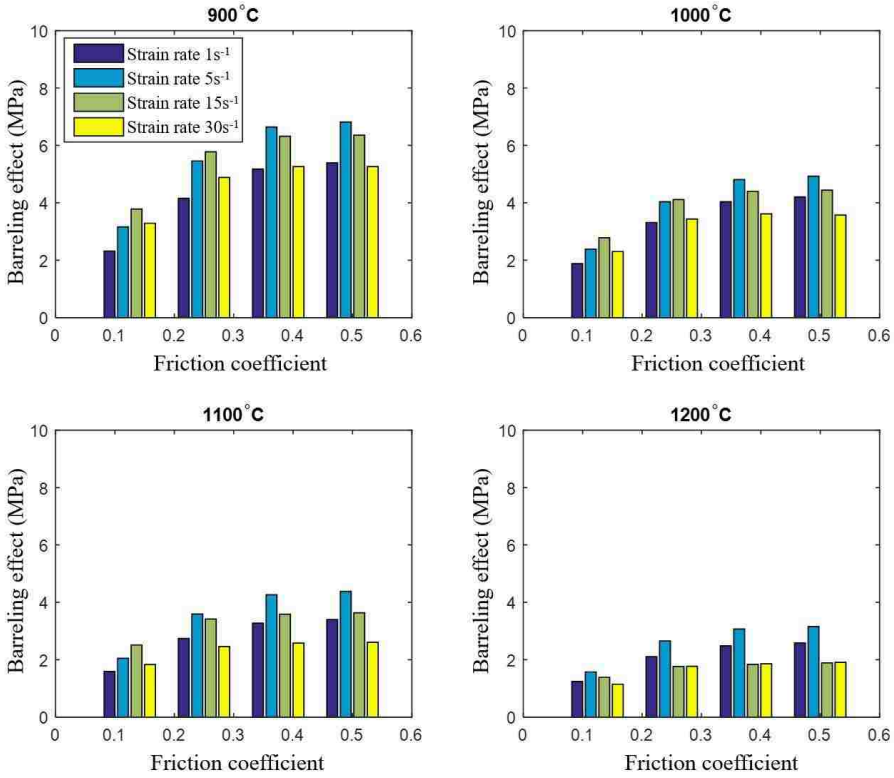

Fig. 12. Strain rate effect on barreling effect

Table 1. Barreling shapes and compression condition of specimens

Specimen number	Height (mm)	d_{max} (mm)	d_{min} (mm)	Temperature	Strain rate
1	7.826	14.887	12.527	1000°C	$15s^{-1}$
2	7.226	15.415	12.886	1100°C	$15s^{-1}$
3	8.550	14.239	12.198	1100°C	$30s^{-1}$
4	7.389	15.327	12.730	1200°C	$15s^{-1}$

REFERENCES

[1] H. V. Martinez, D. Coupard, and F. Girot, “Constitutive model of the alloy 2117-T4 at low strain rates and temperatures,” Journal of Materials Processing Technology, vol. 173, no. 3, pp. 252–259, 2006.

[2] H. Charkas, H. Rasheed, and Y. Najjar, “Calibrating a J2 plasticity material model using a 2D inverse finite element procedure,” International Journal of Solids and Structures, vol. 45, no. 5, pp. 1244–1263, 2008.

[3] J. Rasti, A. Najafizadeh, and M. Meratian, “Correcting the stress-strain curve in hot compression test using finite element analysis and Taguchi method,” International Journal of ISSI, vol. 8, no. 1, pp. 26–33, 2011.

[4] F. Chen and C. Chen, “On the nonuniform deformation of the cylinder compression test,” Journal of Engineering Materials and Technology, vol. 122, no. 2, pp. 192–197, 2000.

[5] R. Narayanasamy and R. Murthy, “Prediction of the barreling of solid cylinders under uniaxial compressive load,” Journal of Mechanical Working Technology, vol. 16, pp. 21–30, 1988.

[6] R. Narayanasamy, S. Sathiyanarayanan, and R. Ponalagusamy, “Study on barrelling in magnesium alloy solid cylinders during cold upset forming,” Journal of Materials Processing Technology, vol. 101, no. 1, pp. 64–69, 2000.

[7] S. Malayappan and G. Esakkimuthu, “Barrelling of aluminium solid cylinders during cold upsetting with differential frictional conditions at the faces,” The International Journal of Advanced Manufacturing Technology, vol. 29, no. 1–2, pp. 41–48, 2006.

[8] I. Hervas, M. Ben Bettaieb, A. Thuault, and E. Hug, “Graphite nodule morphology as an indicator of the local complex strain state in ductile cast iron,” Materials and Design, vol. 52, pp. 524–532, 2013.

[9] Y. Bao and T. Wierzbicki, “A comparative study on various ductile crack formation criteria,” Journal of Engineering Materials and Technology, vol. 126, no. 3, pp. 314-324, 2004.

[10] R. Ebrahimi and A. Najafizadeh, “A new method for evaluation of friction in bulk metal forming,” Journal of Materials Processing Technology, vol. 152, no. 2, pp. 136–143, 2004.

[11] Y. P. Li, E. Onodera, and A. Chiba, “Evaluation of friction coefficient by simulation in bulk metal forming process,” Metallurgical and Materials Transactions A, vol. 41, no. 1, pp. 224–232, 2010.

[12] Z. Yao, D. Mei, H. Shen, and Z. Chen, “A friction evaluation method based on barrel compression test,” Tribology Letters, vol. 51, no. 3, pp. 525–535, 2013.

[13] Y. Li, E. Onodera, and A. Chiba, “Friction coefficient in hot compression of cylindrical sample,” Materials Transactions, vol. 51, no. 7, pp. 1210–1215, 2010.

II. MODELING OF MASS FLOW BEHAVIOR OF HOT ROLLED LOW ALLOY STEEL BASED ON COMBINED JOHNSON-COOK AND ZERILLI-ARMSTRONG MODEL

X. Wang and K. Chandrashekhara

Department of Mechanical and Aerospace Engineering

S. A. Rummel, S. Lekakh, D. C. Van Aken and R. J. O'Malley

Department of Materials Science and Engineering

Missouri University of Science and Technology, Rolla, MO 65409

ABSTRACT

Accuracy and reliability of numerical simulation of hot rolling processes are dependent on a suitable material model, which describes metal flow behavior. In the present study, Gleeble hot compression tests were carried out at high temperatures up to 1300 °C and varying strain rates for a medium carbon micro-alloyed steel. Based on experimental results, a Johnson-Cook model (JC) and a Zerilli-Armstrong (ZA) model were developed and exhibited limitation in characterizing complex viscoplastic behavior. A combined JC and ZA model was introduced and calibrated through investigation of strain hardening, and the coupled effect of temperature and strain rate. Results showed that the combined JC and ZA model demonstrated better agreement with experimental data. An explicit subroutine of the proposed material model was coded and implemented into a finite element model simulating the industrial hot rolling. The simulated rolling torque was in good agreement with experimental data. Plastic strain and stress distributions were recorded to investigate

nonlinear mass flow behavior of the steel bar. Results showed that the maximum equivalent plastic strain occurred at 45° and 135° areas of the cross section. Stress increased with decreasing temperature, and the corresponding rolling torque was also increased. Due to the extent of plastic deformation, rolling speed had limited influence on the internal stress of the bar, but the relative rolling torque was increased due to strain rate hardening.

1. INTRODUCTION

Hot rolling is one of the most important and complex deformation processes in steel manufacturing. Metal forming phenomena, such as viscoplastic deformation, recrystallization, and recovery, occur during the hot rolling to endow metal with expected microstructure and mechanical properties. Among these phenomena, viscoplastic deformation foremost takes place to provide plastic strain and energy for microstructural development. Viscoplastic flow stress is significantly influenced by many factors, such as temperature and strain rate. These factors are not independent, but sufficiently interact and form complex relationships. Thus, an effective constitutive material model considering these parameters is essential for investigation of hot rolling processes. Meanwhile, unlike a strip hot rolling, an as-casted steel bar has more complex stress and strain distributions during hot rolling, and the contact region is a cambered surface with non-uniform compressive force. It is hard to employ traditional analytical methods to investigate this highly-nonlinear process. Finite element analysis (FEA) shows advantages to simulate and investigate steel bar hot rolling. Based on accurate constitutive model, FEA provides an effective way to study mass flow, optimize rolling designs, and enhance steel quality.

In order to describe viscoplastic behavior, a number of constitutive models for steel have been proposed in the last few decades. Johnson-Cook (JC) model [1] is one of most widely used phenomenological constitutive models that considers independently the effects of strain hardening, strain rate hardening, and temperature softening on flow stress. The simplified expression and easy implementation contribute the extensive use of Johnson-Cook model. However, it does not consider the coupled effect of strain rate and temperature on flow stress, causing limited capability of predicting material properties. A series of modified Johnson-Cook models were presented by researchers. Zhang et al. [2] considered the coupled effect of temperature and strain, and proposed a modified Johnson-Cook model on Ni-based super alloy. Lin et al. [3] conducted high temperature tensile tests on a high-strength alloy steel, and presented a modified Johnson-Cook model considering combined effect of strain rate and temperature. However, these modified Johnson-Cook models can be applied only for specific steel grades. Gambirasio and Rizzi [4] proposed a modified Johnson-Cook model using splitting strain rate and temperature effect, and effectively modeled complex material flow behavior. Another widely used phenomenological constitutive model is based upon the Arrhenius equation [5], in which Zener-Hollomon parameter is employed. Large numbers of parameters and polynomial fitting process of Arrhenius equation provide well prediction of flow stress, but implementation is tedious causing the Arrhenius equation not to be used as widely as the Johnson-Cook model. Different from phenomenological constitutive models, physical constitutive models are developed based on material microstructure behavior. Zerilli–Armstrong (ZA) model [6] is one of the widely used physical models based upon dislocation mechanisms. The ZA model does consider the coupled effect of temperature and strain rate, and exhibits more

flexibility than the Johnson-Cook model on predicting material properties. But the coupled effect of temperature and strain rate in Zerilli–Armstrong model is limited and numerous modified versions have been proposed. Samantaray et al [7][8] proposed a modified Zerilli–Armstrong model to predict mass flow behavior of Ti-modified austenitic stainless steel. Lin et al. [9] derived a modified material model by combining Johnson-Cook model and Zerilli-Armstrong model to predict stress-strain curves for a typical high strength steel. However, these modified Zerilli–Armstrong models are limited to specific steel grades and were not suitable for the current study. In addition to phenomenological and physical constitutive models, empirical constitutive models, such as Shida's equation [10], is also widely used. The inputs of Shida's equation are just the metal composition and thus avoids expensive experimental testing. However, the accuracy of Shida's equation is limited compared to other material models.

Hot rolling has been investigated for many years by means of numerical simulation. Kim [11] proposed a finite element model to simulate a shape rolling, and non-uniform temperature distribution during rolling was investigated. Duan and Sheppard [12] studied aluminum strip rolling using finite element method and inverse analysis by comparing simulated torque with measured data. Yang et al. [13] investigated hot rolling of titanium alloy ring using finite element method and the blank size effect on strain and temperature distribution was investigated. Rummel et al. [14] performed high strain rate compression test using split hopkinson pressure bar to gain high strain rate material properties, and incorporated into Johnson-Cook model. Nalawade et al. [15] investigated mass flow behavior of micro-alloyed 38MnVS6 steel during multi-pass hot rolling. Detailed strain distributions on regular cross section showed that both tension and compression existed

during hot rolling of the 38MnVS6 steel. Benasciutti et al. [16] developed a simplified finite element model considering both heating and cooling thermal load to predict thermal stresses during hot rolling, and the simulation results showed good agreement with theoretical solution. Li et al. [17] studied nonlinear deformation during H-beam hot rolling using finite element method and the proposed finite element model was verified by comparing simulated temperature with experimental data. Hosseini Kordkheili et al. [18] derived an implicit finite element subroutine for a rate-dependent constitutive model to describe mass flow behavior of 5052 aluminum. Gao et al. [19] proposed a procedure of developing explicit subroutine of a user-defined generalized material model. However, literatures of finite element analysis on three-dimensional steel bar hot rolling are limited, which involve highly nonlinear geometry and material model.

In the current study, Gleeble hot compression tests were conducted to generate experimental data for material modeling. By comparing to original Johnson-Cook and Zerilli-Armstrong models, a combined JC and ZA model was developed to predict flow stress at varying temperatures and strain rates. A three-dimensional nonlinear finite element model incorporating proposed material model was developed to simulate hot rolling. Plastic strain, stress, and rolling torque were recorded and investigated.

2. EXPERIMENTS

A medium carbon low alloy steel grade with a chemical composition given in percent mass of 0.38C-1.3Mn-0.57Si-0.13Cr-0.08V-0.018Al was investigated. Hot compression tests were performed using the Gleeble thermo-simulation system at varying

temperatures and strain rates to study the material flow behavior. Cylindrical specimens of 15 mm height and 10 mm diameter were machined from as-cast steel bar. A layer of tantalum foil with nickel paste was placed between the specimen and platens to minimize friction during compression. The experimental procedure for the hot compression test is summarized in Table 1 and Fig. 1. The specimens were heated up to 1300 °C at a heating rate of 260 °C/min, held for 3 minutes and cooled to the desired test temperature. An additional hold of 2 minutes was included to minimize temperature gradients, establish a fully austenitic microstructure, and then the compression test was performed at the selected temperature and strain rate. Four temperatures (1000 °C, 1100 °C, 1200 °C and 1300 °C) and four strain rates (0.01 s^{-1}, 1 s^{-1}, 5 s^{-1}, and 15 s^{-1}) were selected for Gleeble hot compression test based on actual hot rolling conditions. Each combination was replicated three times, and a total of 48 specimens were tested. The Gleeble tests were conducted at Gerdau-Spain facility. Experimental results at varying strain rates and temperatures are shown in Fig. 2.

3. CONSTITUTIVE MATERIAL MODELING

3.1 JOHNSON-COOK MODEL

The original Johnson-Cook model is expressed as:

$$\sigma = (A + B\varepsilon^n)(1 + C \ln \dot{\varepsilon}^*)(1 - T^{*m}) \quad (1)$$

where σ is equivalent stress, ε is equivalent plastic strain, $\dot{\varepsilon}^* = \dot{\varepsilon}/\dot{\varepsilon}_0$ is dimensionless strain rate, $\dot{\varepsilon}$ is strain rate, $\dot{\varepsilon}_0$ is reference strain rate, $T^* = (T - T_r)/(T_m - T_r)$ is homologous temperature, T is current temperature, T_r is reference temperature, and T_m is

metal melting temperature. Constants A, B, C, m and n are material parameters. Constant A is a yield stress at a user defined reference temperature and reference strain rate. Constants B and n are strain hardening parameters. Constant C is strain rate hardening parameter. Constant m is a temperature softening parameter. In the current study, the reference strain rate and temperature of Johnson-Cook model are chosen as 1 s^{-1}, and 1000 °C. The melting temperature of the steel grade tested is 1520 °C.

Two different methods are frequently used to determine the Johnson-Cook parameters. One is determining parameters one by one using curve fitting [20]; another is determining all five parameters simultaneously by an optimization method [21]. However, both methods have limitations: the former only considers partial experimental data when determining each parameter, and the latter is restricted usually into a local optimum. In the current study, initial parameters were determined by curve fitting, and then optimized by nonlinear least-square method.

3.1.1 Determination of Parameters using Curve Fitting. At reference temperature 1000 °C and reference strain rate 1 s^{-1}, $\ln \dot{\varepsilon}^*$ and T^{*m} in Eq. 1 become zero. The Johnson-Cook material model reduces to:

$$\sigma = A + B\varepsilon^n \tag{2}$$

Parameter A is calculated as the yield stress at the reference condition. Yield stress is defined at the point dividing linear part and nonlinear part on stress-strain curve. By substituting values of experimental stress σ and plastic strain ε into Eq. 2, initial values of parameter B and parameter n were calculated from plot of σ vs. ε using power law fitting (Fig. 3a). At the reference temperature, but varying strain rate, the Johnson-Cook model can be expressed as Eq. 3.

Under a series of strain points (0.1, 0.2, 0.3, and 0.4), the relationship of $\sigma/(A + B\varepsilon^n)$ and $\ln \dot{\varepsilon}^*$ was plotted at varying stress and strain rates (Fig. 3b). A linear fitting process was performed in Fig. 3b, and the initial value of parameter *C* was obtained from the slope of fitting line. Similarly, at reference strain rate 1 s^{-1} and varying temperatures, the Johnson-Cook model is expressed as Eq. 4.

$$\sigma/(A + B\varepsilon^n) = (1 + C \ln \dot{\varepsilon}^*) \quad (3)$$

$$\sigma/(A + B\varepsilon^n) = (1 - T^{*m}) \quad (4)$$

Initial value of parameter *m* was calculated from power law fitting process of $\sigma/(A + B\varepsilon^n)$ vs. T^{*m} (Fig. 3c).

3.1.2 Optimization of Parameters. A least-square optimization method was used to optimize parameters of Johnson-Cook model. The fitness function is shown in Eq. 5 which minimizes the sum of square error between experimental data and prediction of material model:

$$\min f(x) = \min \sum_{i=1}^{N} \left|\sigma_i^{exp} - \sigma_i^{JC}(X)\right|^2 \quad (5)$$

where *N* is the number of experimental data points, σ_i^{exp} is the experimental stress value at data point i, $\sigma_i^{JC}(X)$ is the prediction of the Johnson-Cook model, and $X = [A, B, n, C, m]$ is a vector of parameters, which is initialized by the results of the curve fitting process in section 3.1.1. A fitness function and the initial conditions were defined using MATLAB. The optimized parameters of Johnson-Cook model are shown in Table 2. The R^2 value between experimental data and prediction of Johnson-Cook model was calculated as 0.9078. Variance-covariance matrix of model parameters was used to evaluate

parameter uncertainty and parameter correlation. Jacobian matrix X of material model can be expressed as:

$$X = \begin{bmatrix} X_{11} & \cdots & X_{1n} \\ \vdots & \ddots & \vdots \\ X_{i1} & \cdots & X_{in} \end{bmatrix} = \begin{bmatrix} \frac{\partial \sigma_1}{\partial P_1} & \cdots & \frac{\partial \sigma_1}{\partial P_n} \\ \vdots & \ddots & \vdots \\ \frac{\partial \sigma_i}{\partial P_1} & \cdots & \frac{\partial \sigma_i}{\partial P_n} \end{bmatrix} \quad (6)$$

where X is Jacobian matrix, σ_i is calculated stress using parameter set P_n, i is the number of measured experimental data, n is the number of parameters. In current study, P_1~P_5 represent A, B, n, C, and m. The variance-covariance matrix Cov_{JC} is calculated as:

$$\mathrm{Cov}_{JC} = (\mathrm{X'X})^{-1} e^2 = \begin{bmatrix} JC_{11} & \cdots & JC_{15} \\ \vdots & \ddots & \vdots \\ JC_{51} & \cdots & JC_{55} \end{bmatrix} \quad (7)$$

where Cov_{JC} is the variance-covariance matrix of Johnson-Cook model parameters, X is Jacobian matrix, and e is the error between experiment and prediction of material model. A confidence interval for parameter P_i can be estimated using the ith diagonal element JC_{ii} of variance-covariance matrix (Table 2).

3.2 ZERILLI-ARMSTRONG MODEL

Zerilli-Armstrong (ZA) model, different from phenomenological-based Johnson-Cook model, is built based on dislocation mechanisms, which essentially determine the plastic flow behavior. The original Zerilli-Armstrong model can be expressed as [6]:

$$\sigma = C_0 + C_1 exp(-C_3 T + C_4 T ln\dot{\varepsilon}) + C_5 \varepsilon^n \quad \text{(BCC metals)} \quad (8)$$

$$\sigma = C_0 + C_2 \varepsilon^{0.5} exp(-C_3 T + C_4 T ln\dot{\varepsilon}) \quad \text{(FCC metals)} \quad (9)$$

where σ is the equivalent stress, ε is the equivalent plastic strain, $\dot{\varepsilon}$ is strain rate, T is temperature, and $C_0 \sim C_5$ are parameters of Zerilli-Armstrong model. Since high

temperature during hot rolling (above 1000 ℃), microstructures of steel change into austenite with FCC structure, and therefore Eq. 9 was used in the current study. In the original Zerilli-Armstrong model, temperature and strain rate are not normalized, causing a huge numerical differences among parameters (e.g. C_2 is up to 10^3 while parameter C_4 is low to 10^{-4}). This magnitude difference complicates the determination of parameters and the subsequent modeling of hot working processes. Therefore, a dimensionless temperature T^* and a normalized strain rate $\dot{\varepsilon}^*$ were introduced to Zerilli-Armstrong model, and Eq. 9 becomes:

$$\sigma = C_0 + C_2\varepsilon^{0.5} exp(-C_3T^* + C_4T^* \ln \dot{\varepsilon}^*) \quad (10)$$

where $T^*$is the homologous temperature and $\dot{\varepsilon}^*$ is dimensionless strain rate. Similar to the curve fitting process of Johnson-Cook model, parameters of Zerilli-Armstrong model in Eq. 10 were identified by curve fitting process and nonlinear least-square method. At reference temperature and strain rate, Eq. 10 can be expressed as:

$$\sigma = C_0 + C_2\varepsilon^{0.5} \quad (11)$$

In Eq. 11, C_0 is the yield stress at reference temperature and strain rate. C_2 was calculated using power law fitting process (Fig. 4a). At reference the strain rate and varying strains and temperature, Eq. 10 can be expressed as:

$$\ln[(\sigma - C_0)/C_2\varepsilon^{0.5}] = -C_3T^* \quad (12)$$

A linear fitting process of Eq. 12 was performed to determine C_3 (Fig. 4b). With determined parameters C_0, C_2, and C_3, Eq. 10 can be written as:

$$[\ln[(\sigma - C_0)/C_2\varepsilon^{0.5}] + C_3T^*]/T^* = C_4 \ln \dot{\varepsilon}^* \quad (13)$$

Parameter C_4 was obtained using linear fitting process at fixed strain and temperature (Fig. 4c). All four parameters were optimized by nonlinear least-square

method, and the optimized parameters are shown in Table 3. The R^2 value between experimental data and prediction of Zerilli-Armstrong model was calculated as 0.8685. The corresponding variance-covariance matrix diagonal elements ZA_{ii} are shown in Table 3.

3.3 COMBINED JC AND ZA MODEL

In the original Johnson-Cook (JC) model, a relationship between flow stress and plastic strain is established empirically by isolated effects of strain rate and temperature upon the flow stress. The concise formulation of the Johnson-Cook model facilitates calculation of the material model parameters using a limited amount of experiments. However, this simplification does not consider the coupled effect of temperature and strain rate on flow stress, which was observed from both current Gleeble test results and literature data [5]. On the other hand, the original Zerilli-Armstrong model takes into account the coupled effect of temperature and strain rate on flow stress. However, the actual coupled effect of temperature and strain rate is complex. The fixed yield stress C_0 at varying temperatures and strain rates in original Zerilli-Armstrong model is not reasonable according to actual situation.

To overcome these shortcomings, a combined JC and ZA model was proposed and is given by

$$\sigma = (A_1 + B_1\varepsilon + B_2\varepsilon^{n_1})((C_1 + C_2 * \ln\dot{\varepsilon}^*) + (C_3 + C_4 * \ln\dot{\varepsilon}^*) * (T^*)^{m_1+m_2*\ln\dot{\varepsilon}^*}) \quad (14)$$

Eq. 14 accounts for the modified strain hardening effect of Johnson-Cook model, and the coupled effect of strain rate and temperature based upon Zerilli-Armstrong model. The development process of this combined material model is discussed in following sections.

3.3.1 Strain Hardening Effect. A strain hardening effect ($A_1 + B_1\varepsilon + B_2\varepsilon^{n_1}$) was used in current study, which was based upon the work of Lin et al. [3] Lin et al. modified the strain hardening part of the Johnson-Cook model ($A + B\varepsilon^n$) into ($A_1 + B_1\varepsilon + B_2\varepsilon^{n_1}$). The introduction of $B_1\varepsilon$ enables the new model to describe actual complex stress-strain relationships. To evaluate this modified version, predictions of modified Johnson-Cook model were calculated and compared with original Johnson-Cook model (see Fig. 5 and Table 4). In the low strain range [0, 0.05] and high strain range [0.4, 0.45], the predictions of original Johnson-Cook model showed larger stress than actual test results, and at medium strain range [0.05, 0.4], the original Johnson-Cook model predicted lower stress than experimental results. The R-square (R^2) values of predictions of original and modified strain hardening effect are 0.964 and 0.999, respectively, which illustrates that the modified strain hardening effect predicted stress-strain curve closer to experimental data.

3.3.2 Coupled Effect of Temperature and Strain Rate. The coupled effect of temperature and strain rate was developed based on Johnson-Cook model and Zerilli-Armstrong model. The original Johnson-Cook model predicts a temperature softening effect on flow stress as ($1 - T^m$), but the actual Gleeble test results demonstrated that this temperature softening effect varied with different strain rate conditions. Multiplication of temperature and strain rate in original Zerilli-Armstrong model was used to present this coupled effect. A modified temperature softening effect with strain rate dependent parameters is shown in Eq. 15:

$$\sigma/(A_1 + B_1\varepsilon + B_2\varepsilon^{n_1}) = D_{01} + D_{02} * (T^*)^{m_0} \quad (15)$$

in which D_{01}, D_{02}, and m_0 are strain rate dependent parameters. Dimensionless stress is defined as $\sigma^* = \sigma/(A_1 + B_1\varepsilon + B_2\varepsilon^{n_1})$. Flow stress at four strains (0.1, 0.2, 0.3, and 0.4)

of varying strain rates and temperatures were chosen to determine these parameters (Fig. 6). Power function fitting was performed to determine the relationships between temperature and flow stress at different strain rates. The fitting parameters are shown in Table 5. Results showed that temperature softening parameters D_{01}, D_{02}, and m_0 were strongly dependent on strain rate.

A detailed study of strain rate hardening effect on flow stress was also performed. Temperature softening parameters (D_{01}, D_{02}, and m_0) vs. $\ln \dot{\varepsilon}^*$ were plotted in Fig. 7, where $\dot{\varepsilon}^* = \dot{\varepsilon}/\dot{\varepsilon}_0$ is dimensionless strain rate, $\dot{\varepsilon}$ is strain rate, and $\dot{\varepsilon}_0$ is reference strain rate set as 0.01 s^{-1}.

In Fig. 7(a) and (b), linear relationships were found between parameters (D_{01} and D_{02}) and $\ln \dot{\varepsilon}^*$. The relative expressions are shown in Eq. 16 and 17 with parameters $D_1 \sim D_4$. In Fig. 7(c), power function was used to build relationship between m_0 and $\ln \dot{\varepsilon}^*$ with parameters $m_1 \sim m_3$ (Eq. 18). These coupled effect parameters are shown on Table 6.

$$D_{01} = D_1 + D_2 * \ln \dot{\varepsilon}^* \quad (16)$$

$$D_{02} = D_3 + D_4 * \ln \dot{\varepsilon}^* \quad (17)$$

$$m_0 = m_1 + m_2 * (\ln \dot{\varepsilon}^*)^{m_3} \quad (18)$$

4. FINITE ELEMENT MODELING

A nonlinear three-dimensional finite element model was developed to study a steel bar hot rolling process. The complete hot rolling process was to repeatedly deform steel bar to reduce dimension of cross section by sequential and orthogonal rolling steps. In the current simulation, the first stand, Stand1, was simulated. Cross section of steel bar was

deformed from round to oval during Stand1. The initial length of bar was 4 m and had an initial diameter of 0.235 m. The round bar entered Stand1 with an initial speed of 0.14 m/s. The Coulomb friction was modeled between steel bar and rollers, and the coefficient of friction was set as 0.6 [22]. The initial temperatures for the steel bar and roller were 1100 °C and 150 °C, respectively. Rotation speed of the roller was 5.75 rpm with a roll gap of 33.1 mm, a pass depth of 60.3 mm, and a working diameters of 606 mm. Geometry modeling was processed using ABAQUS 6.12 (Fig. 8). The friction behavior between contact pairs was defined by Coulomb friction law with a friction coefficient 0.5. The steel bar was built as a three-dimensional deformable part using 8-node brick element (C3D8RT), and rollers were modeled as rigid parts using 4-node rigid element (R3D4). The governing equation for thermo-mechanical analysis and heat transfer during hot rolling can be written as:

$$[M^e]\{\ddot{\Delta}^e\} + [K^e]\{\Delta^e\} = \{F_M^e\} + \{F_T^e\} \tag{19}$$

$$[C_T^e]\{\dot{\theta}^e\} + [K_T^e]\{\theta^e\} = \{Q^e\} \tag{20}$$

where $[M^e]$ is mass matrix, $[K^e]$ is the stiffness matrix, and $\{F_M^e\}$ and $\{F_T^e\}$ are mechanical, thermal loadings respectively, $[C_T^e]$ is specific heat capacity matrix, $[K_T^e]$ is conductivity matrix, and $\{Q^e\}$ is the external flux vector. In the present study, combined JC and ZA material model was coded into subroutine VUMAT. For elastic calculation, Hooke's law was used and expressed in Green-Naghdi rate form:

$$\Delta\sigma_{ij} = \lambda\delta_{ij}\Delta\varepsilon_{kk}^e + 2\mu\Delta\varepsilon_{ij}^e \tag{21}$$

$$\Delta\varepsilon_{ij} = \Delta\varepsilon_{ij}^e + \Delta\varepsilon_{ij}^p \tag{22}$$

where $\Delta\sigma_{ij}$ is the stress increment, λ and μ are Lame parameters, δ_{ij} is Kronecker delta, $\Delta\varepsilon_{ij}^e$ is the elastic strain increment, $\Delta\varepsilon_{ij}^p$ is the plastic strain increment, and $\Delta\varepsilon_{ij}$ is the total

strain increment. For plastic strain calculation, the isotropic hardening law was adopted and the von Mises yield criterion for isotropic plasticity was used:

$$f = \sigma_v - \sigma_y = \sigma_{eq}^{tr} - 3\mu\Delta\bar{\varepsilon}^{pl} - \sigma_y = 0 \quad (23)$$

$$\sigma_{ij}^{tr} = \sigma_{ij} + \lambda\delta_{ij}\Delta\varepsilon_{kk} + 2\mu\Delta\varepsilon_{ij} \quad (24)$$

where σ_v is von Mises stress, and σ_y is yield stress provided by material model, σ_{eq}^{tr} is trial von Mises stress calculated by $\Delta\sigma_{ij}^{tr}$, and $\Delta\bar{\varepsilon}^{pl}$ is equivalent plastic strain increment. When $\sigma_v < \sigma_y$, deformation of material is considered elastic, otherwise plastic. Newton's method is used to calculate $\Delta\bar{\varepsilon}^{pl}$. Based on plastic flow law, the increment tensor of plastic strain can be calculated by Eq. 25 and the stress tensor is updated by Eq. 26:

$$\Delta\varepsilon_{ij}^{p} = \frac{3}{2}\Delta\bar{\varepsilon}^{pl}\frac{\sigma_{ij}'}{\sigma_v} \quad (25)$$

$$\sigma_{ij} = \sigma_{ij}^{tr} - 2\mu\Delta\varepsilon_{ij}^{p} \quad (26)$$

where σ_{ij}' is deviatoric stress of σ^{tr}. The overall calculation process is shown in Fig. 9.

5. RESULTS AND DISCUSSION

5.1 COMPARISON OF MATERIAL MODELS

Comparisons of Johnson-Cook model, Zerilli-Armstrong model and the combined JC and ZA model were performed. The operating temperature of hot rolling was from 1100 °C to 1000 °C, and the compressing strain rate was from 1 s^{-1} to 5 s^{-1}. Predictions of each material model at varying operating temperatures and strain rates are plotted in Fig. 10. The combined JC and ZA model shows better agreement with experimental data than either the Johnson-Cook or the Zerilli-Armstrong model. At 1100 °C and strain rates of 1

s^{-1} and 5 s^{-1}, predictions of Johnson-Cook model show significant deviation from experimental results, which is caused by the nonlinear coupled effect of temperature and strain rate. At 1000 °C and strain rates of 1 s^{-1} and 5 s^{-1}, the Zerilli-Armstrong model is incapable of predicting actual experimental results. The fixed C_0 greatly limits the flexibility of Zerilli-Armstrong model, producing the same yield stress at varying temperatures and strain rates. With the enhanced strain hardening effect and coupled effect of temperature and strain rate, the combined JC and ZA model demonstrated more accurate predictions.

The overall comparison of material models was performed using a coefficient of determination R^2, which indicated how well the predictions of each material model fit with experimental data. The best linear fit was plotted using a solid black line (Fig. 11), at which predicted flow stress is equal to experimental data. The red circles (Fig. 11) represented the actual predicted flow stresses at corresponding experimental flow stress. Greater deviation from the best linear fit line and a reduced R^2 value indicated a less accurate material model. In Fig. 11a, the partial predictions of Johnson-Cook model have significant differences from best linear fit line, while other predictions fit experimental data well. It indicates that Johnson-Cook model is insufficient to predict complex material behavior with coupled effect of temperature and strain rate. In Fig. 11b, the predicted yield stress of Zerilli-Armstrong model is constant. With increasing strain, the flow stress increases fast, and finally larger than experimental data. It indicates that Zerilli-Armstrong model has high strain hardening rate, which is not suitable for current study of low strain hardening rate. In Fig. 11c, with modified strain hardening behavior and couple effect of temperature and strain rate, the combined JC and ZA model performs much better prediction than other

material models. Based on Fig. 11, the R^2 values of Johnson-Cook model, Zerilli-Armstrong model, and combined JC and ZA model are 0.9078, 0.8685, and 0.9798, respectively, indicating better performance of combined JC and ZA model.

5.2 ROLLING TORQUE COMPARISON

The finite element model was verified by comparing predicted rolling torque with experimental data. The simulated rolling torques of Stand1 during hot rolling process are plotted in Fig. 12, comparing to a measured continuous rolling torque of 537 kN·m was provided by the Gerdau steel plant. In the beginning of the simulated hot rolling process, a steel bar took around 0.5 s to make contact with mills. As the bar was further deformed, the predicted torque increased quickly to reach a stable level. Simulated torques based on combined JC and ZA model were around 500 kN·m and within 7% of the reported rolling torque.

5.3 PLASTIC STRAIN DISTRIBUTION

Understanding plastic strain distribution during hot rolling process is important to control microstructure evolution, void closure, quality of steel, and optimization of the rolling process. The simulated deformation process of the steel bar during hot rolling is shown in Fig. 13. In the current study, the cross section of steel bar was deformed from round to oval in Stand1.The cross section of steel bar was perfect circle prior to deformation (reduction was 0%). Initially the steel bar is compressed vertically. The vertical radius of the cross section decreased while the horizontal radius almost remained the same

dimension with minor increase. The final shape of steel bar cross section was shown in an oval shape with 100% reduction.

Equivalent plastic strain, as well as plastic strain in specific directions, was recorded and investigated. Simulated equivalent plastic strain distributions after hot deformation are shown in Fig. 14a. The maximum equivalent plastic strain 0.65 occurred at top and bottom areas, and a minimum of 0.35 occurs along the center horizontal axis. Specific strain components of the strain tensor can be displayed for the three normal strains. In the x-direction (Fig. 14b), the maximum compressive plastic strain was at the bar center, while smallest plastic strain happened on the bar sides, which were not contacted with the mills. Plastic strain in the y-direction (Fig. 14c) was a mixture of tension at the bar center and compression on the surfaces. During this rolling process, material at the central portion of the bar moved towards the surface, while surface friction at the roll caused internal tension and compression at the surface in y-direction. In the z-direction (Fig. 14d), the steel bar was elongated parallel to the rolling direction, and plastic strain in z-direction varied in a small range (0.32-0.34).

A detailed study of the plastic strain distributions was conducted. Top surface nodes (from node 1 to node 24), and internal nodes (from node 1 to node 26) were monitored and relative plastic strain was plotted in Fig. 15. For the surface equivalent plastic strain distribution (see Fig. 15a), the maximum value was located at surface nodes 6 and node 19, which were in 45° and 135° directions rather than the top node at 13. For the internal equivalent plastic strain distributions (see Fig. 15b), the minimum value occurred at node 1 and node 26, and stable value with slight decline exhibited in center area (nodes 8 to 19). Surface plastic strain in x-direction and y-direction (see Fig. 15a) were in compression,

while plastic strain in z-direction (see Fig. 15a) was in tension. At the middle node 13, surface plastic strain in x-direction increased to the maximum compression strain -0.35, while surface plastic strain in y-direction decreased to minimum strain around 0. Similarly, internal plastic strain distributions in each direction were plotted in Fig. 15b. For both surface and internal plastic strain distribution, the plastic strain in the x-direction or rolling direction became the largest contributor to the equivalent plastic strain. Plastic strain in y-direction was 50%~80% magnitude of strain in other directions. Plastic strain in the z-direction, maintained relatively stable strain distribution for both surface and internal areas.

5.4 STRESS DISTRIBUTION AND ROLLING TORQUE

Investigation of stress distribution and rolling torque is essential to industrial practice, which may contribute to increased production efficiency and product quality. Viscoplastic material properties are dependent upon the rolling temperature and rolling speed, and thus can significantly influence the manufacturing process. Based on practical hot rolling conditions, the simulated rolling temperature was chosen as 1100 °C, 1050 °C, and 1000 °C, and the simulated rolling speed was chosen as 0.14 m/s, and 0.7 m/s, which corresponds to strain rates from 1 s^{-1} to 5 s^{-1}. At varying temperatures and rolling speeds, the stress distributions and rolling torques were calculated and investigated.

Stress distributions at different rolling temperatures are shown in Fig. 16. Stresses of nodes from 1 (center of bar) to 13 (surface of bar) were monitored. At center and surface (node 1 and node 13), the difference of stresses at different temperature is not significant and less than 10 MPa. However, at the middle of monitored nodes (from node 6 to node 12), the flow stresses are dependent on rolling temperature. At the lowest temperature of

1000 °C, stress increases to 65 MPa (node 10), and then decreases; at a temperature of 1050 °C, the stress increases to around 51 MPa from node 1 to node 7, and keeps nearly constant from node 7 to node 13; at temperature 1100 °C, the stress increases from the center to the surface of the bar. The stress difference is caused by temperature softening effect, under which stress is reduced at same deformation. The flow stress patterns indicate that stress is concentrated at nodes 7 through 12 of the bar, and the higher rolling temperature can reduce internal stress.

Roll torque was calculated as well. As temperature decreases from 1100°C to 1000°C, the roll torque increases from 500 kN·m to 740 kN·m (Fig. 17). Due to temperature softening effect, the rolling torque decreases around 120 kN·m with 50°C increase of temperature.

Similarly, rolling speed effect on stress distribution can be investigated and results are plotted in Fig. 18. Different from the temperature effect, however, rolling speed has limited effect on stress distribution of the steel bar. The stresses increase from the center (node 1) to the surface (node 13), and the stress difference between different rolling speeds is within 10 MPa. At different rolling speed, flow stresses at center and surface are similar, and from node 4 to node 7 flow stress at rolling speed 7 m/s is larger than flow stress at rolling speed 1.4 m/s. The corresponding rolling torque increased from 480 kN·m to 600 kN·m due to increase of rolling speed (Fig. 19).

6. CONCLUSION

In the current study, a Johnson-Cook model, a Zerilli-Armstrong model, and a combined JC and ZA model were developed based on Gleeble hot compression test results. The combined JC and ZA model considering the combined effect of temperature and strain rate, and modified strain hardening effect demonstrated better prediction on flow stress than original material models at elevated temperatures and varying strain rates.

A three-dimensional nonlinear finite element model incorporating combined JC and ZA model is developed to simulate steel bar hot rolling. Plastic strain distributions during hot deformation process were plotted and investigated. Maximum equivalent plastic strain occurs at 45° and 135° areas of cross section, instead of top and bottom areas of cross section. Plastic strain is in compression in the x-direction, tension in the z-direction, and both tension and compression in the y-direction. Flow stress and rolling toque at different temperatures and rolling speeds were studied. Stress distribution on cross section is significantly influenced by rolling temperature, while rolling speed has limited effect on stress distribution. As temperature increases, rolling torque decreases; as rolling speed increases, the rolling torque increases.

ACKNOWLEDGEMENT

This work was supported by the Peaslee Steel Manufacturing Research Center at Missouri University of Science and Technology. The authors would like to thank Geary W. Ridenour and Rafael Pizarro Sanz from Gerdau for technical input and Gleeble testing.

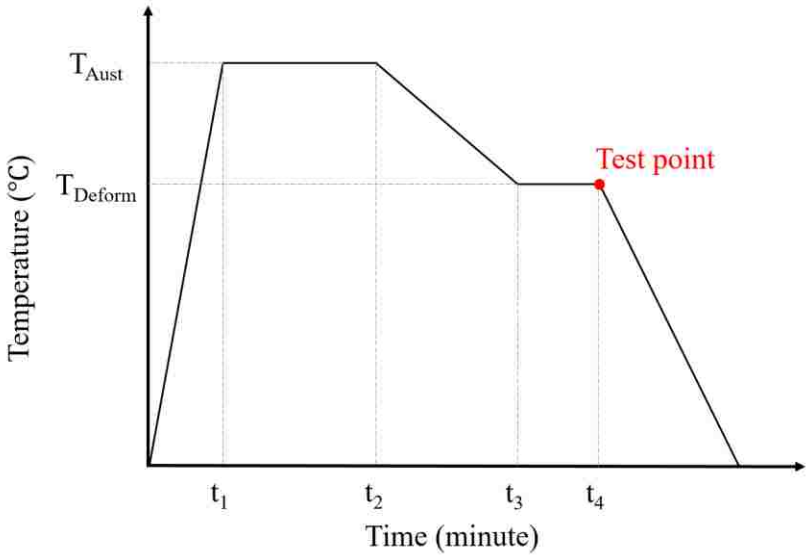

Fig. 1. Test profile for Gleeble hot compression test

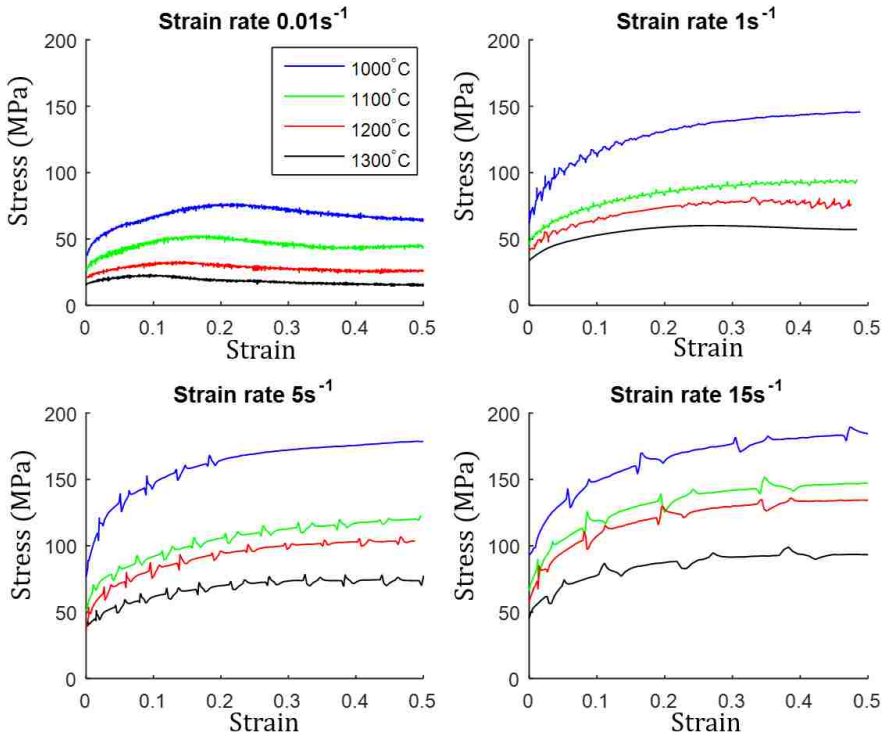

Fig. 2. Experimental results of Gleeble hot compression tests

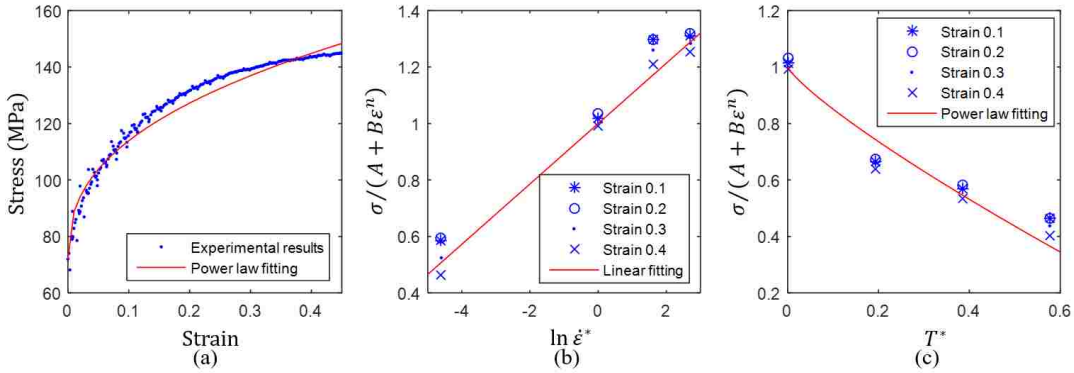

Fig. 3. (a) Power law fitting process of parameters B and n, (b) linear fitting process of parameter C, (c) power law fitting process of parameter m

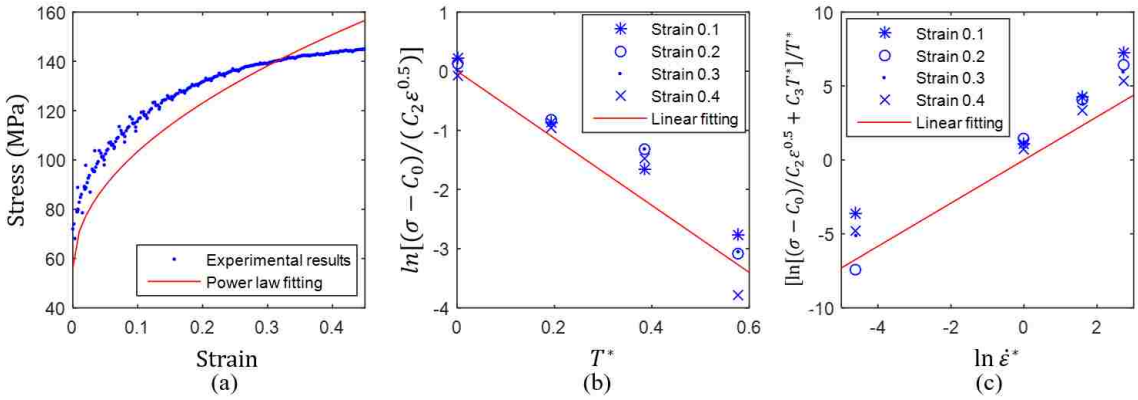

Fig. 4. (a) Power law fitting process of parameter C_0 and C_2, (b) linear fitting process of parameter C_3, (c) linear fitting process of parameter C_4

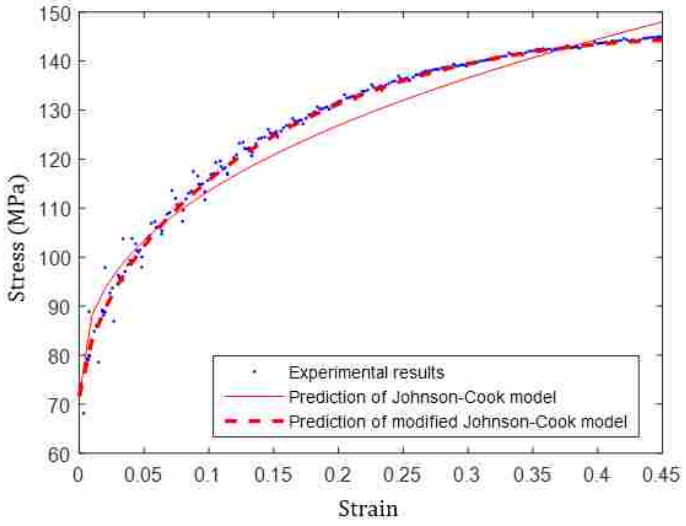

Fig. 5. Predictions of Johnson-Cook model and modified Johnson-Cook model

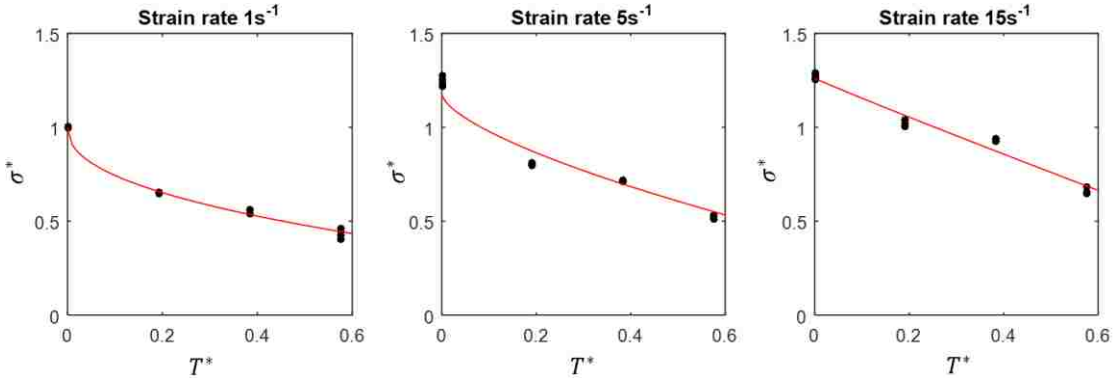

Fig. 6. Temperature effects on flow stress at different strain rates

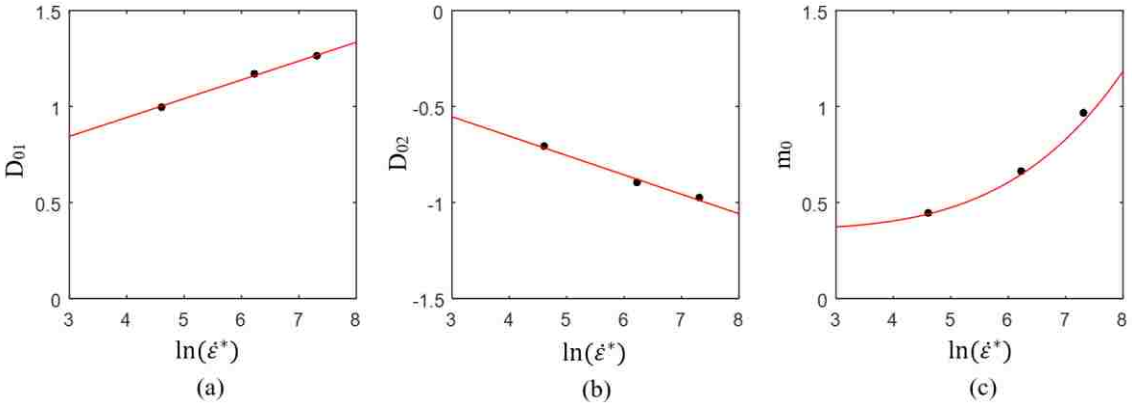

Fig. 7. Relationship between strain rate and temperature softening parameters

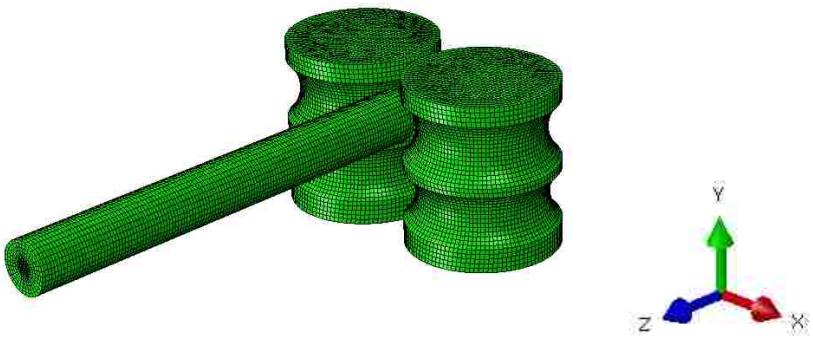

Fig. 8. Modeling of steel bar hot rolling process

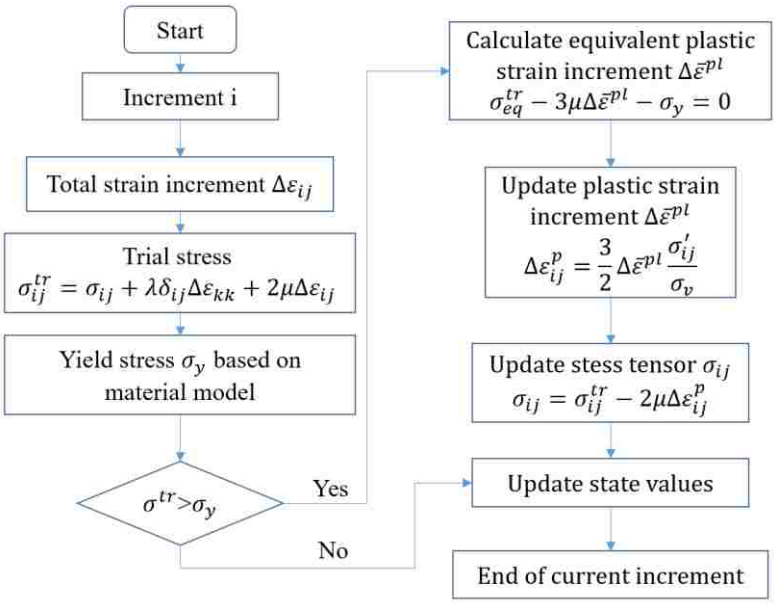

Fig. 9. Flowchart of VUMAT for combined JC and ZA model

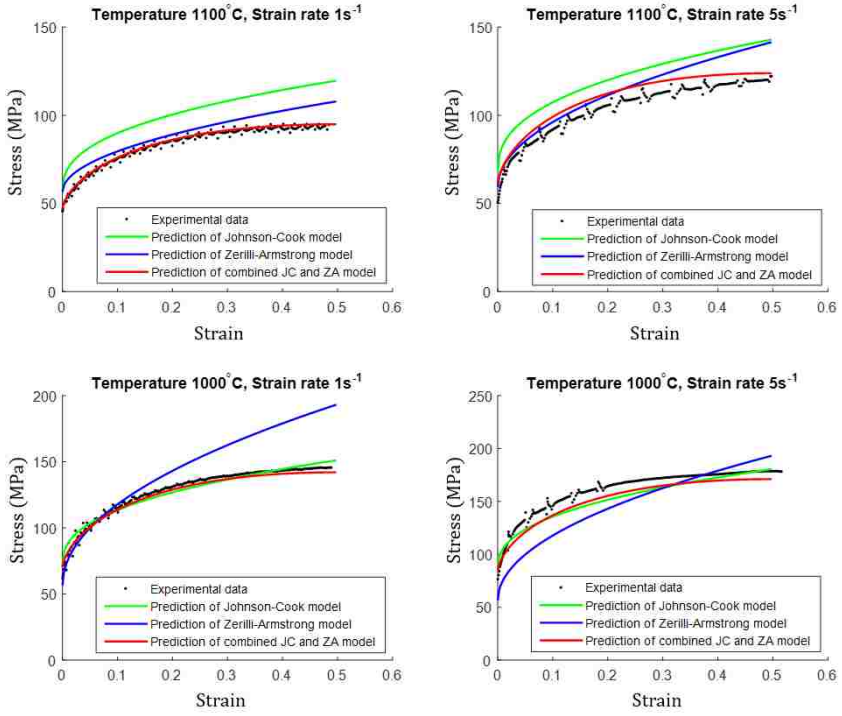

Fig. 10. Comparison of predicted stress-strain curves of different material models

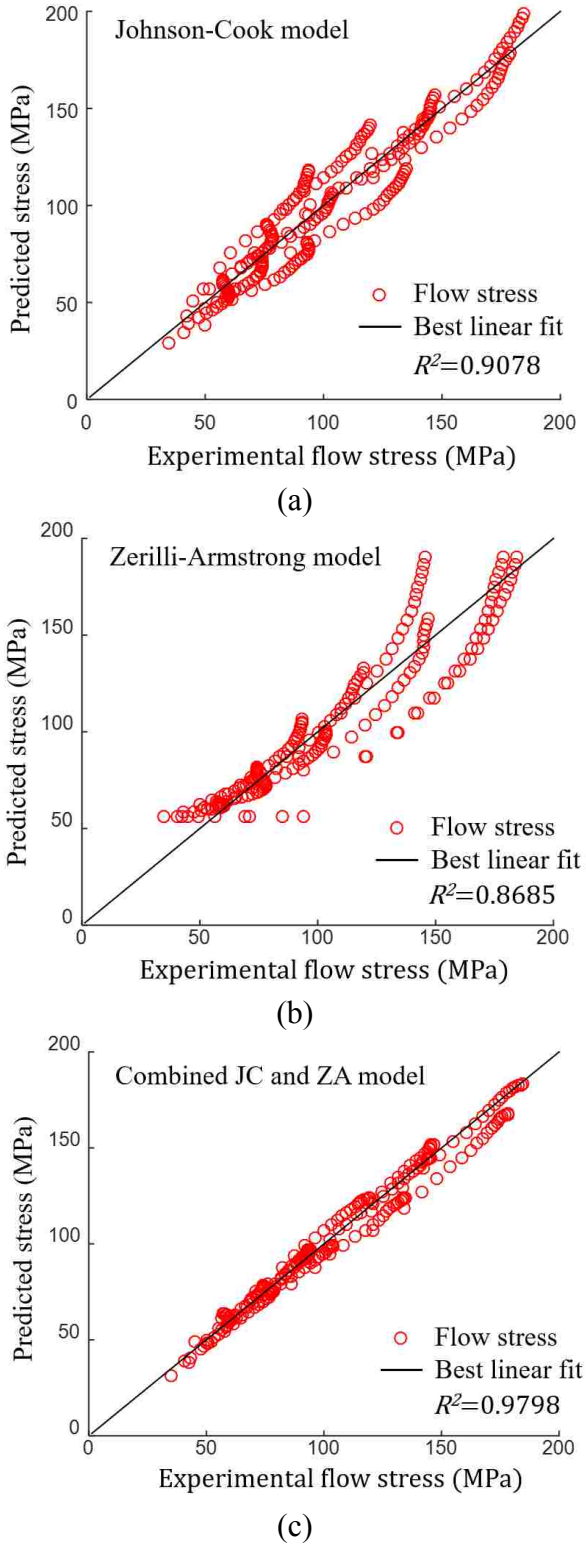

Fig. 11. Comparison of experimental data and (a) prediction of Johnson-Cook model, (b) prediction of Zerilli-Armstrong model, and (c) prediction of combined JC and ZA model

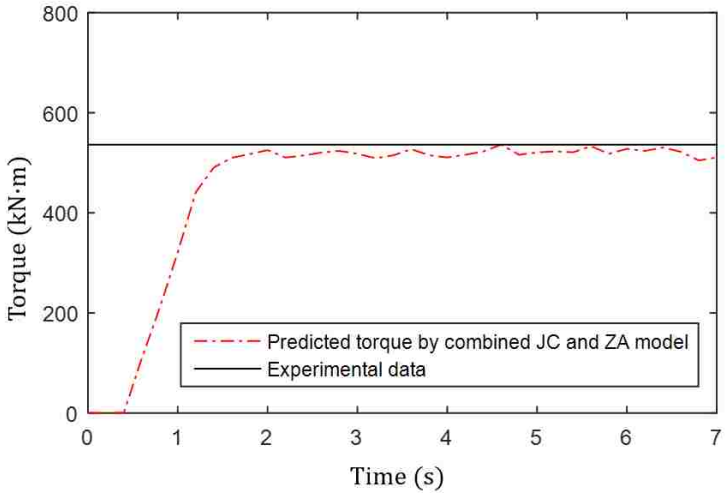

Fig. 12. Rolling torque comparison between measured and simulated results

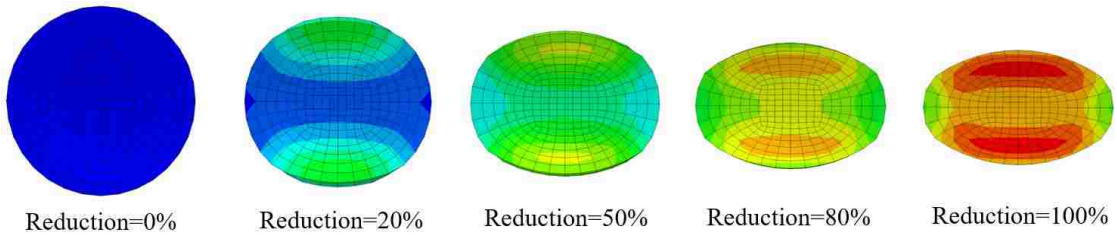

Fig. 13. Schematic deformation process of steel bar during hot rolling process

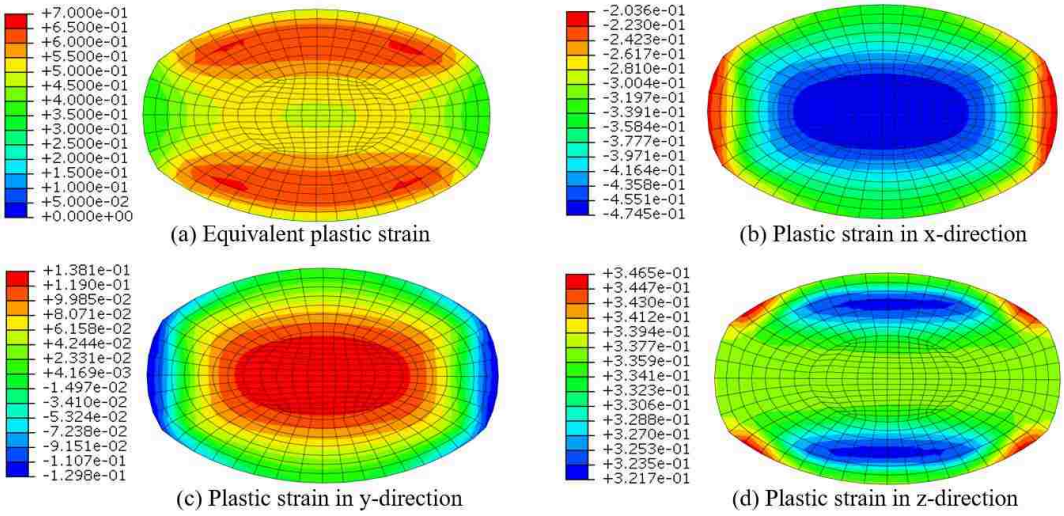

Fig. 14. Plastic strain distribution in specific direction and equivalent plastic strain distribution

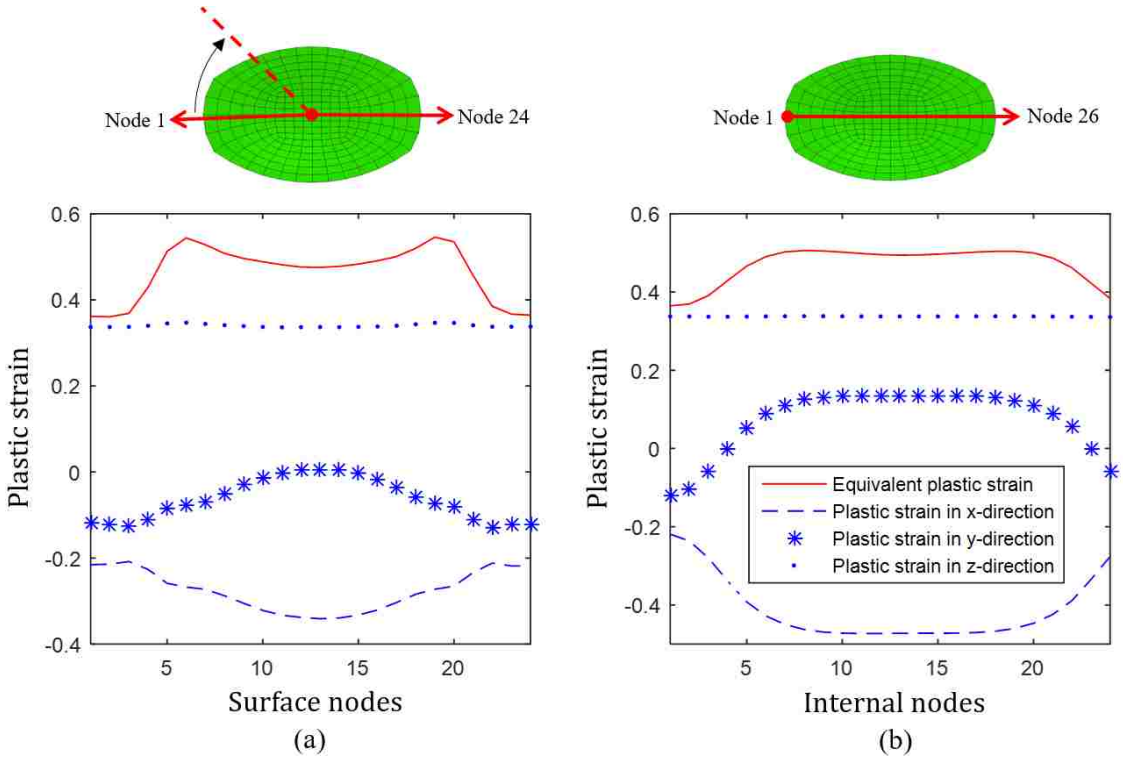

Fig. 15. (a) surface and (b) internal plastic strain distributions in specific direction

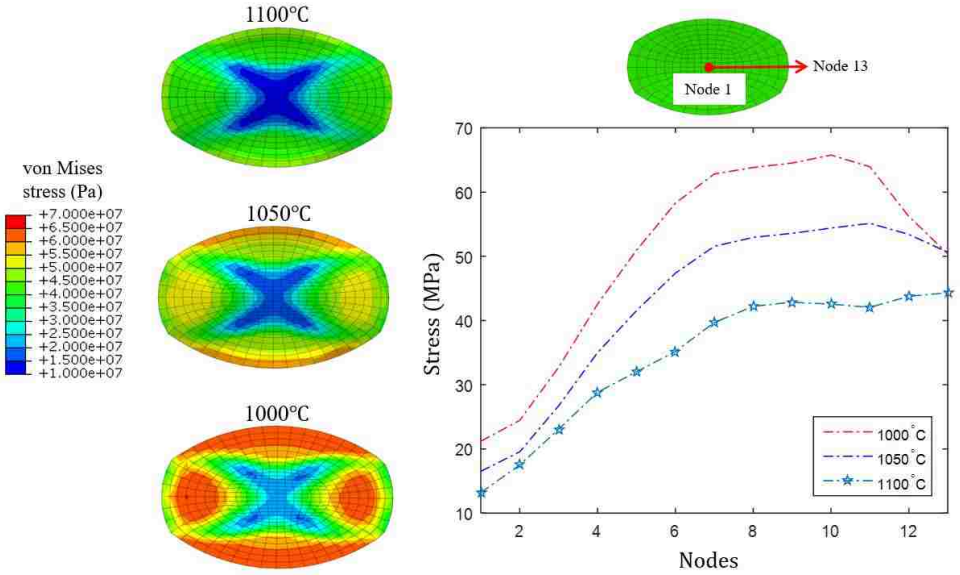

Fig. 16. Stress distribution at different temperatures

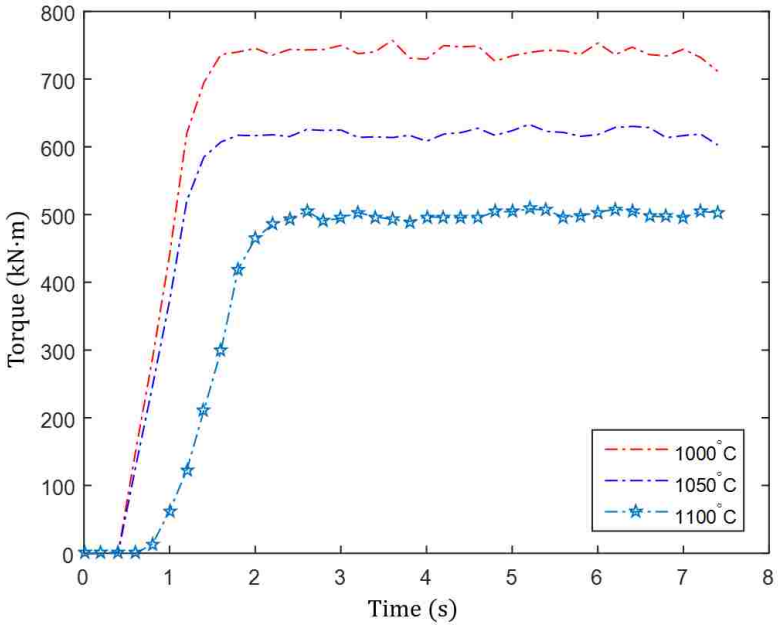

Fig. 17. Rolling torque at different temperatures

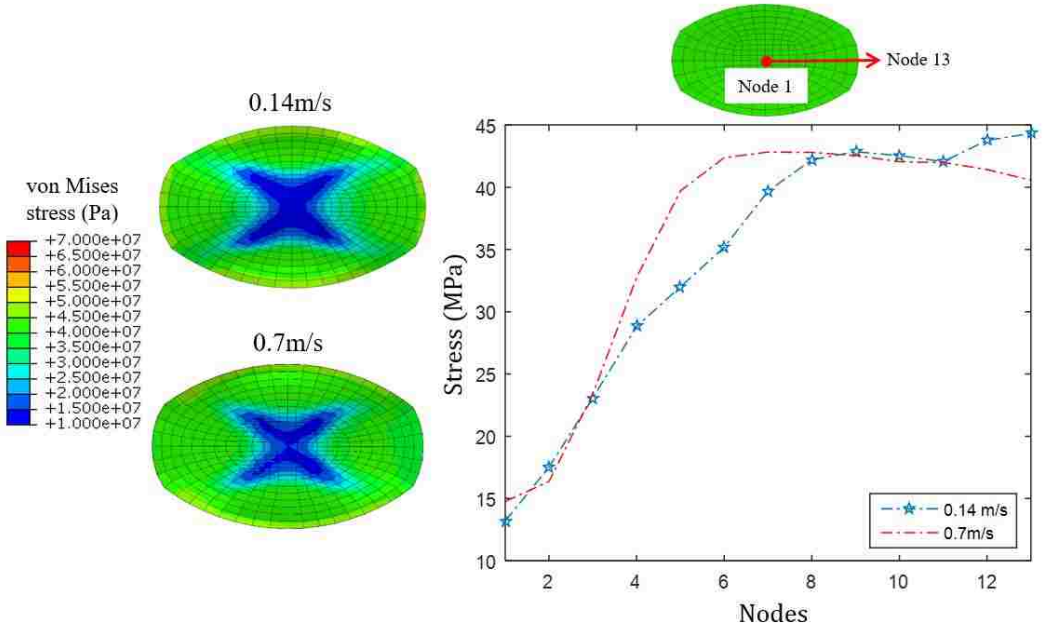

Fig. 18. Stress distribution at different rolling speed

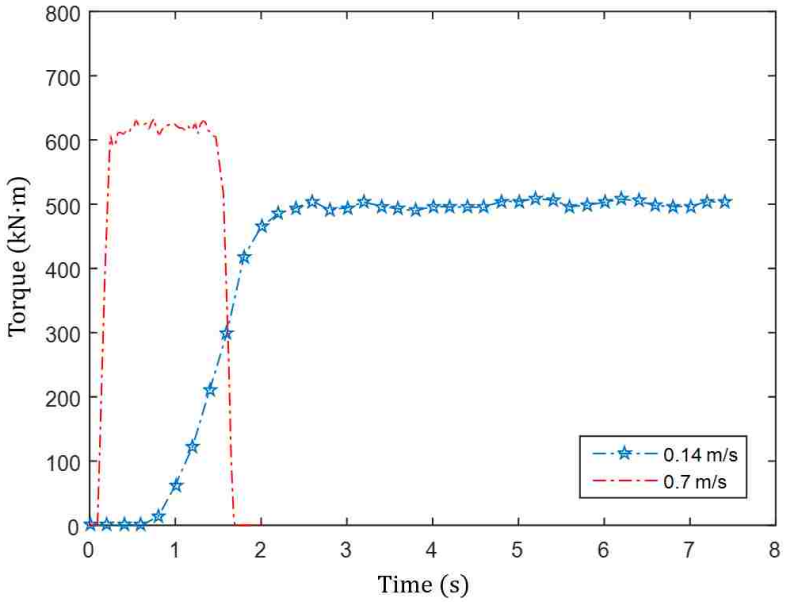

Fig. 19. Rolling torque at different rolling speed

Table 1. Test parameters for Gleeble hot compression test

Temperature (°C)		Time (min)		Heating rate (°C/min)
T_{Aust}	1300	t_1	5	260
		t_2	8	0
T_{Deform}	Varies	t_3	Varies	-50
		t_4	+2	0

Table 2. Determined parameters of Johnson-Cook model

	A	*B*	*n*	*C*	*m*	R^2
Value	71.59	105.03	0.39	0.12	0.95	0.9078
Variance-Covariance matrix diagonal	JC_{11}=0.07	JC_{22}=0.22	JC_{33}=0.12	JC_{44}=1.77e-6	JC_{55}=2.42e-5	

Table 3. Determined parameters of Zerilli-Armstrong model

	C_0	C_2	C_3	C_4	R^2
Value	56.54	193.6	5.087	1.359	0.8685
Variance-Covariance matrix diagonal	ZA_{11}=0.07	ZA_{22}=0.78	ZA_{33}=5.28e-4	ZA_{44}=8.86e-5	

Table 4. Parameters of strain hardening effect

	Original Johnson-Cook model			Lin's modified Johnson-Cook model			
Parameter	A	B	n	A_1	B_1	B_2	n_1
Value	71.59	105.03	0.39	71.59	-392.6	446.1	0.7283
R^2	0.967			0.999			

Table 5. Temperature softening parameters of combined JC and ZA model

Parameter	D_{01}	D_{02}	m_0
Strain rate $1s^{-1}$	0.997	-0.707	0.446
Strain rate $5s^{-1}$	1.172	-0.896	0.664
Strain rate $15s^{-1}$	1.261	-0.977	0.964

Table 6. Coupled effect parameters of combined JC and ZA model

Parameter	D_1	D_2	D_3	D_4	m_1	m_2	m_3
Value	0.551	0.098	-0.250	-0.101	0.360	1.3e-4	4.21

REFERENCES

[1] G. R. Johnson and W. H. Cook, "A constitutive model and data for metals subjected to large strains, high strain rates and high temperatures," 7th International Symposium on Ballistics, vol. 21, pp. 541–547, 1983.

[2] H. Zhang, W. Wen, and H. Cui, "Behaviors of IC10 alloy over a wide range of strain rates and temperatures: Experiments and modeling," Materials Science and Engineering A, vol. 504, no. 1–2, pp. 99–103, 2009.

[3] Y. Lin, X. Chen, and G. Liu, "A modified Johnson–Cook model for tensile behaviors of typical high-strength alloy steel," Materials Science and Engineering: A, vol. 527, no. 26, pp. 6980–6986, 2010.

[4] L. Gambirasio and E. Rizzi, "An enhanced Johnson – Cook strength model for splitting strain rate and temperature effects on lower yield stress and plastic flow," Computational Materials Science, vol. 113, pp. 231–265, 2016.

[5] Y. Lin and X. Chen, "A critical review of experimental results and constitutive descriptions for metals and alloys in hot working," Materials & Design, vol. 32, pp. 1733–1759, 2011.

[6] F. J. Zerilli and R. W. Armstrong, "Dislocation-mechanics-based constitutive relations for material dynamics calculations," Journal of Applied Physics, vol. 61, no. 5, pp. 1816–1825, 1987.

[7] D. Samantaray, S. Mandal, and A. K. Bhaduri, "A comparative study on Johnson Cook, modified Zerilli–Armstrong and Arrhenius-type constitutive models to predict elevated temperature flow behaviour in modified 9Cr–1Mo steel," Computational Materials Science, vol. 47, no. 2, pp. 568–576, 2009.

[8] D. Samantaray, S. Mandal, U. Borah, A. K. Bhaduri, and P. V. Sivaprasad, "A thermo-viscoplastic constitutive model to predict elevated-temperature flow behaviour in a titanium-modified austenitic stainless steel," Materials Science and Engineering A, vol. 526, no. 1–2, pp. 1–6, 2009.

[9] Y. C. Lin and X. M. Chen, "A combined Johnson-Cook and Zerilli-Armstrong model for hot compressed typical high-strength alloy steel," Computational Materials Science, vol. 49, no. 3, pp. 628–633, 2010.

[10] S. Shida, "Empirical formula of flow stress of carbon steels—resistance to deformation of carbon steels at elevated temperature," Journal of the Japan Society for Technology of Plasticity, vol. 10, pp. 610–617, 1969.

[11] S. Kim and Y. Im, “Three-dimensional finite element analysis of non-isothermal shape rolling,” Journal of Materials Processing Technology, vol. 127, pp. 57–63, 2002.

[12] X. Duan and T. Sheppard, “Three dimensional thermal mechanical coupled simulation during hot rolling of aluminium alloy 3003,” International Journal of Mechanical Sciences, vol. 44, pp. 2155–2172, 2002.

[13] H. Yang, M. Wang, L. Guo, and Z. Sun, “3D coupled thermo-mechanical FE modeling of blank size effects on the uniformity of strain and temperature distributions during hot rolling of titanium alloy large rings,” Computational Materials Science, vol. 44, no. 2, pp. 611–621, 2008.

[14] S. Rummel, D. Van Aken, R. O’Malley, X. Wang, and K. Chandrashekhara, “High strain rate hot deformation of steels: measurement and simulation,” in Proceedings of the International Conference on Advances in Product Metallurgy of Long and Forged Products, pp. 1–10, Vail, CO, 2015

[15] R. S. Nalawade, A. J. Puranik, G. Balachandran, K. N. Mahadik, and V. Balasubramanian, “Simulation of hot rolling deformation at intermediate passes and its industrial validity,” International Journal of Mechanical Sciences, vol. 77, pp. 8–16, 2013.

[16] D. Benasciutti, E. Brusa, and G. Bazzaro, “Finite elements prediction of thermal stresses in work roll of hot rolling mills,” Procedia Engineering, vol. 2, pp. 707–716, 2010.

[17] K. Li, P. Wang, G. Liu, P. Yuan, and Q. Zhang, “Development of simulation system for large H-beam hot rolling based on ABAQUS,” International Journal of Advanced Manufacturing Technology, vol. 85, no. 5, pp. 1649–1663, 2016.

[18] S. A. Hosseini Kordkheili, M. M. Ashrafian, and H. Toozandehjani, “A rate-dependent constitutive equation for 5052 aluminum diaphragms,” Materials and Design, vol. 60, pp. 13–20, 2014.

[19] C. Y. Gao, “FE realization of thermo-visco-plastic constitutive models using VUMAT in ABAQUS/Explicit Program,” Computational Mechanics ISCM2007, pp. 623–628, 2007.

[20] A. He, G. Xie, H. Zhang, and X. Wang, “A comparative study on Johnson-Cook, modified Johnson-Cook and Arrhenius-type constitutive models to predict the high temperature flow stress in 20CrMo alloy steel,” Materials and Design, vol. 52, pp. 677–685, 2013.

[21] N. Dusunceli, O. U. Colak, and C. Filiz, “Determination of material parameters of a viscoplastic model by genetic algorithm,” Materials & Design, vol. 31, no. 3, pp. 1250–1255, 2010.

[22] M. Awais, H. W. Lee, Y. T. Im, H. C. Kwon, S. M. Byon, and H. D. Park, “Plastic work approach for surface defect prediction in the hot bar rolling process,” Journal of Materials Processing Technology, vol. 201, no. 1984, pp. 73–78, 2008.

III. MODELING AND SIMULATION OF DYNAMIC RECRYSTALLIZATION BEHAVIOR IN ALLOYED STEEL 15V38 DURING HOT ROLLING

X. Wang and K. Chandrashekhara

Department of Mechanical and Aerospace Engineering

S. N. Lekakh, D. C. Van Aken and R. J. O'Malley

Department of Materials Science and Engineering

Missouri University of Science and Technology, Rolla, MO 65409, USA

ABSTRACT

Dynamic recrystallization (DRX) occurring during hot rolling significantly affects the microstructural evolution and final mechanical properties of steel. In this study, single hot compression tests were performed at temperatures between 1000°C and 1300°C with strain rates between 0.01 s^{-1} and 15 s^{-1} to investigate dynamic recrystallization behavior of a 15V38 steel. Critical strains for initiation of dynamic recrystallization and peak strains were identified through the analysis of work hardening rate from the measured stress-strain results. Dynamic recrystallization was identified by the softening in the flow stress during plastic deformation and quantified as the difference between a calculated dynamic recovery curve and the measured stress-strain curve. Dynamic recrystallization was modeled using calculated critical strain, peak strain, Zener-Hollomon (Z) parameter, and volume fraction of dynamic recrystallization. Subroutines accounting for dynamic recrystallization were developed and implemented into a three-dimensional finite element model for hot rolling of a round bar. Simulation results show that dynamic recrystallization is distributed

throughout the bar and exhibits a positive relationship with equivalent plastic strain. Temperature effects on dynamic recrystallization were also investigated using different rolling temperatures, and results show that the fraction of dynamic recrystallization is significantly increased as rolling temperature increases.

1. INTRODUCTION

Austenite grain size and shape are influenced by many factors during hot rolling including stored plastic deformation, static recovery, static recrystallization, dynamic recrystallization, and grain pinning by second phase carbides and nitrides. The final austenite grain size is an important aspect for controlling properties during steel manufacturing. In the absence of grain pinning agents, temperature, plastic strain, and the imposed strain rate control the evolution of the austenite grain structure. In a general sense, hot rolling plastically deforms the steel and energy is stored as point defects and dislocations. Recovery processes eliminate point defects and form dislocation subcells that act as nuclei for new grains. This process occurring during deformation is called dynamic recovery and recrystallization. Dynamic recrystallization (DRX) initiated during deformation often be completed by subsequent hot working or by static processes after deformation due to the short deformation time. Investigation of dynamic recrystallization is essential to optimize hot rolling schedules and produce steel with a homogeneous grain structure.

Sellars is one of the pioneers in modeling recrystallization using Avrami kinetics [1]. A dynamic recovery curve and the critical strain need to be determined to construct the

Avrami equation for dynamic recrystallization. Poliak and Jonas calculated a critical strain required to initiate recrystallization by identifying the minimum differential of work hardening rate [2]. Jonas et al. [3] provided an effective method to derive the dynamic recovery curve and then determined the softening associated with dynamic recrystallization using stress-strain curves measured during hot deformation. These findings provide a basis for mathematical modeling of dynamic recrystallization.

Dehghan-Manshadi et al. [4] characterized the microstructure evolution during dynamic recrystallization of 304 austenitic stainless steel. The results showed that the critical strain was around 60 % of peak strain and full dynamic recrystallization needs a high strain of around 4.5 times the critical strain. Chen et al. [5] modeled dynamic recrystallization behavior of 42CrMo steel using hot compression tests, and the experimental results indicated that initial austenitic grain size, as well as temperature and strain rate, affects dynamic recrystallization. Schambron et al. [6] studied the dynamic recrystallization of low carbon micro-alloyed steel using hot compression tests. The results showed that the ratio of critical strain to peak strain is 0.42. Chen et al. [7] developed a segmented model describing dynamic recrystallization behavior of a nickel-based alloy, which can accurately predict fraction of DRX below 980 °C. Competition between dynamic recovery and dynamic recrystallization were investigated by Souza et al. [8] and Ning et al. [9], and equations of dislocation energy and work hardening rate were used to identify the dynamic recovery curve. Wang et al. [10] performed hot compression tests of ultra-high strength stainless steel and found that critical strain decreases as strain rate increases for 1 s^{-1} to 10 s^{-1}. Results showed that strain rate has a complex effect on dynamic recrystallization due to the interaction between dynamic recrystallization and precipitation

during hot deformation. These studies demonstrate that the kinetics of DRX of different steel grades vary considerably, and modeling of dynamic recrystallization for the current study is necessary.

Numerical simulation provides an effective method to investigate dynamic recrystallization during hot rolling. Avrami equations representing dynamic recrystallization were successfully incorporated into finite element model [11], and the evolution of DRX during steel bar [12] and I-beam [13] hot rolling was simulated. Investigations of rolling parameter using finite element method were performed by Ding et al. [14] and it was found that rolling temperature has a more significant effect on dynamic recrystallization than rolling speed. Baron et al. [15] used a regression analysis method to determine the parameters of the dynamic recrystallization model and incorporated it into a finite element model to simulate the hot compression of high strength martensitic steel. These literatures provide valuable background for the modeling and simulation of DRX during steel bar hot rolling process in this study.

In the current study, Gleeble hot compression tests were performed at various temperatures and strain rates. Critical strain, peak strain, and Zener-Hollomon (Z) parameter were calculated based on experimental data, and dynamic recovery curves were determined using differentiation methods. Dynamic recrystallization behavior was modeled and implemented into a finite element model to simulate the hot rolling process. Critical strain, equivalent plastic strain, fraction of DRX, and the effect of temperature on dynamic recrystallization were investigated.

2. MODELING OF DYNAMIC RECRYSTALLIZATION

2.1 EXPERIMENTAL STRESS-STRAIN CURVES

As-cast 15V38 steel with chemical composition in mass % as shown in Table 1 was used in this study. Cylindrical specimens of 15 mm height and 10 mm diameter were machined from the as-cast steel bar and material flow behavior was measured in compression using a Gleeble 3500 simulation system. Test temperatures ranged from 1000°C to 1300°C and strain rates up to 15 sec^{-1} were used. A layer of tantalum foil with nickel paste was placed between the specimen and platens to minimize friction during compression.

Test specimens were heated up to 1300 °C (T_{Aust}) in 5 minutes (t_1) with a heating rate of 260 °C/min, held for 3 minutes for austenitizing and cooled to the desired test temperature (T_{Deform}). An additional hold of 2 minutes was included to eliminate temperature gradient, and then the compression test was performed at the selected temperature and strain rate (Fig. 1). Four temperatures (1000 °C, 1100 °C, 1200 °C, and 1300 °C) and four strain rates (0.01 s^{-1}, 1 s^{-1}, 5 s^{-1}, and 15 s^{-1}) were selected for hot compression testing based upon actual hot rolling conditions. Each combination of temperature and strain rate was repeated three times, with a total of 48 specimens being tested.

Examples of the hot compression test results are illustrated in Fig. 2. At low strain rate 0.01 s^{-1}, all stress-strain curves demonstrate work hardening with a maximum in the flow stress followed by softening. The peak flow stress and the strain at flow curves decreased as the test temperature increased. At other strain rates from 1 s^{-1} to 15 s^{-1},

softening behavior was only observed at the higher temperatures for strain rates of 1 s^{-1} and 5 s^{-1} and was absent for a strain rate of 15 s^{-1}.

Dynamic recrystallization contributes to the softening in stress-strain curves. Before hot deformation, large primary grains dominate the microstructure with low dislocation density. During initial hot deformation, large amounts of dislocation are generated and controlled by work hardening, dynamic recovery. With continue of hot deformation, dynamic recrystallization occurs when the accumulated dislocation density exceeds critical point. The dynamic recrystallized grains then nucleate at the grain boundary and grow on non-growing grains [16, 17] and results in a refined microstructure. With full dynamic recrystallization, a near steady state flow stress is observed. At higher strain rates, the flow stress curve demonstrates continued hardening with a parabolic shape or reaches a steady state value. An approximate peak stress can be determined from the steady state condition.

2.2 CRITICAL STRAIN

During deformation, dynamic recrystallization is initiated by a critical strain. Newly formed grains grow until impingement and an equiaxed grain structure can be obtained. Several methods were proposed to investigate the critical strain, and among these methods, Poliak and Jonas [2] demonstrated an effective method using flow curve analysis to determine the critical strain. Work hardening rate $\theta = \partial\sigma/\sigma\varepsilon$ (where σ is stress and ε is plastic strain) was calculated to identify a critical strain whereby the onset of dynamic recrystallization is identified. An example of the Poliak and Jonas method is shown in Fig. 3. Experimental data from the hot compression test performed at temperature 1100 °C and

strain rate 0.01 s^{-1} is plotted in Fig. 3a. Higher order polynomial smoothing was performed on raw stress-strain curves and work hardening rate was calculated based on $\theta = \partial\sigma/\sigma\varepsilon$ (see Fig. 3b). At stage I, the work hardening rate decreases in a linear fashion. At stage II, the reduction of work hardening rate becomes faster due to the initiation of dynamic recrystallization. The critical point is defined at the start of Stage II. Stage III is defined when a maximum is reached in the flow stress and softening is observed with continued straining. To accurately determine the critical point, the derivative of work hardening rate $-\partial\theta/\partial\sigma$ vs. σ was calculated in Fig. 3c and the minimum value of $-\partial\theta/\partial\sigma$ was found to be the critical point.

Work hardening curves at strain rates of 0.01 s^{-1} and 1 s^{-1} are plotted in Fig. 4. Critical points were located using minima of derivative of work hardening rate $-\partial\theta/\partial\sigma$ vs. σ. The critical strain was then determined as the corresponding strain associated with the critical point. The calculated critical points are marked in Fig. 4 using red circles. As temperature increases at low strain rate 0.01 s^{-1} (Fig. 4a), the critical stress and corresponding critical strains decrease, since higher temperature reduces the required dislocation energy for initiation of dynamic recrystallization. At a higher strain rate of 1 s^{-1} (Fig. 4b), the experimental stress-strain curves do not display stress-softening behavior as significantly as strain rate 0.01 s^{-1}. The critical strain increases due to less deformation time (reduced from 50 s at strain rate 0.01 s^{-1} to 0.5 s at strain rate 1 s^{-1}) for evolution of dynamic recrystallization. Work hardening curves at 5 s^{-1} and 15 s^{-1} are similar to that shown for 1 s^{-1}. The peak stresses and peak strains at strain rates 0.01 s^{-1} and 1 s^{-1} were determined directly from work hardening curve at $\theta = 0$.

2.3 ZENER-HOLLOMON PARAMETER

Critical strain, peak strain, and peak stress can be expressed in the form of a Zener-Hollomon parameter *Z*, which is proportional to the strain rate $\dot{\varepsilon}$ and has an Arrhenius dependence upon temperature:

$$Z = A[\sinh(\alpha\sigma)]^{n_0} = \dot{\varepsilon}\exp\left(\frac{Q}{RT}\right) \quad (1)$$

where σ is stress, *Q* is activation energy for deformation, *R* is gas constant (8.31 $J \cdot mol^{-1} \cdot K^{-1}$), *T* is the absolute temperature, and *A*, α, and n_0 are constants. The activation energy *Q* indicates the natural deformation ability of steel and can be calculated as:

$$Q = R * n_0 * \frac{\partial[lnsinh(\alpha\sigma_{pk})]}{\partial(1/T)} \quad (2)$$

$$n_0 = \frac{\partial(ln\dot{\varepsilon})}{\partial[lnsinh(\alpha\sigma_{pk})]} \quad (3)$$

where α is calculated as β/n'. [4] Parameter $n' = \frac{\partial\sigma_{pk}}{\partial\ln(\dot{\varepsilon})}$ was calculated as 12.505±1.85 MPa·s in Fig. 5a by the average slope of σ_{pk} vs $\ln(\dot{\varepsilon})$, and parameter $\beta = \frac{\partial ln\sigma_{pk}}{\partial\ln(\dot{\varepsilon})}$ was calculated as 0.156±0.013 MPa·s in Fig. 5b by the average slope of $ln\sigma_{pk}$ vs $\ln(\dot{\varepsilon})$. Parameter α is then calculated as β/n' =0.012. The parameter n_0 and $\frac{\partial[lnsinh(\alpha\sigma_{pk})]}{\partial(1/T)}$ were then calculated as 4.71±0.20 $s^{-1}\cdot MPa^{-1}$ and 9.517±0.49 MPa·°C in Fig. 5c and 5d by the average fitting slope, and the initial value of activation energy *Q* was calculated as 381.9 kJ/mol by Eq. 2. To optimize the value of activation energy *Q* and parameter n_0, least square optimization method was employed using all experimental data. Eq. 1 can be written:

$$ln\left[\dot{\varepsilon}\,exp\left(\frac{Q}{RT}\right)\right] = ln(A) + n_0 ln(sinh(\alpha\sigma)) \quad (4)$$

With initial value of *Q*=381.9 kJ/mol and n_0=4.71 $s^{-1}\cdot MPa^{-1}$, the fitting process is shown in Fig. 6 with optimized parameters *Q*=372 kJ/mol and n_0=4.65 $s^{-1}\cdot MPa^{-1}$.

With the identification of activation energy Q, the Z parameter was built considering temperature and strain rate effects. Peak stress σ_{pk}, peak strain ε_{pk}, and critical strain ε_c can be expressed in form of Z parameter. The peak stresses and Z parameters at varying temperatures and strain rates are plotted in Fig. 7a. A power law fitting was used to characterize the relationship between peak stress and Z parameter:

$$\sigma_{pk} = A_1 Z^{n_1} \tag{5}$$

where A_1 and n_1 are parameters. Similarly, the corresponding peak strains and Z parameters were plotted in Fig. 7b with power law fitting:

$$\varepsilon_{pk} = A_2 Z^{n_2} \tag{6}$$

where A_2 and n_2 are parameters. The critical strain was proved to be a fraction of the peak strain:

$$\varepsilon_c = B_1 \varepsilon_{pk} \tag{7}$$

where B_1 is parameter. The calculated parameters are shown in Table 2. The experimental results showed good agreement with power law fitting, and the parameter B_1 was calculated as 0.42, which is in the range of literature data [6].

2.4 DYNAMIC RECOVERY AND DYNAMIC RECRYSTALLIZATION

During hot compression testing, both dynamic recovery (DRV) and dynamic recrystallization (DRX) occurred and contributed to the softening in the flow stress curve. It is necessary to differentiate DRV from DRX to determine the accurate fraction of DRX. The dynamic recovery behavior can be characterized by the work hardening curve before the critical strain where dynamic recrystallization is absent. The measured flow stress during plastic deformation is a combination of hardening by the accumulation of

dislocations and softening by dynamic recovery. The differential increase in dislocation density is given by [3]

$$d\rho = hd\varepsilon - r\rho d\varepsilon \quad (8)$$

where ρ is dislocation density, ε is plastic strain, h is hardening parameter, and r is rate of dynamic recovery. In this equation, $hd\varepsilon$ represents the strain hardening, and $r\rho d\varepsilon$ represents the dynamic recovery. Based on Eq. 8, the dynamic recovery curve can be expressed as [3]

$$\sigma = [\sigma_{sat}^2 - (\sigma_{sat}^2 - \sigma_0^2)\exp(-r\varepsilon)]^{0.5} \quad (9)$$

where σ_{sat} is the steady stress in dynamic recovery curve and σ_0 is the yield stress. The stress σ_{sat} is calculated by extrapolation of the work hardening curve unaffected by dynamic recrystallization (prior to the critical point) to a value of $\theta = 0$. Work hardening measured at temperature 1100 °C and strain rate 0.01 s^{-1} was used to display σ_{sat} in Fig. 8a. To calculate the rate of dynamic recovery, Eq. 9 can be rewritten as Eq. 10.

$$\sigma\frac{d\sigma}{d\varepsilon} = 0.5r\sigma_{sat}^2 - 0.5r\sigma^2 \quad (10)$$

Replacing $\frac{d\sigma}{d\varepsilon}$ with θ and differentiating both sides of Eq. 10 with respect to σ^2:

$$\frac{d(\sigma\theta)}{d(\sigma^2)} = -0.5r \quad (11)$$

The rate of dynamic recovery can be calculated based on the slope of curve $\sigma\theta$ vs. σ^2, shown in Fig. 8b. The volume fraction of dynamic recrystallization can be expressed as

$$X_{DRX} = 1 - \exp(-k\left(\frac{\varepsilon-\varepsilon_c}{\varepsilon_{pk}}\right)^n) \quad (12)$$

where X_{DRX} is the fraction of DRX, ε is the strain, ε_c is critical strain, ε_{pk} is peak strain, and k and n are material dependent parameters. Points of peak stress/strain and stress equal

to critical stress were used to identify parameters k and n in Eq. 12. At low strain rate 0.01 s^{-1}, experimental stress-strain curves exhibited significant stress softening. However, at relatively high strain rates from 1 s^{-1} to 15 s^{-1} there was insufficient time for complete dynamic recrystallization. Therefore, the parameters k and n were determined from the lower strain rate test conducted at 0.01 s^{-1}. Based on the literature [3], the fraction of DRX at peak stress is 10%, and the fraction of DRX at a stress equal to critical strain is 90%. Curves $ln[(\varepsilon - \varepsilon_c)/\varepsilon_{pk}]$ vs. $ln[ln(1/(1-X))]$ at different temperatures were calculated. The slope is n and the intercept is lnk (Fig. 9). The average n and k values are 2.294 and 0.448, respectively.

3. FINITE ELEMENT MODELING

A nonlinear three-dimensional finite element model was developed to study hot rolling of a round steel bar. The first stand of the full hot rolling process, Stand-1, was modeled and simulated. The initial dimensions of the bar were 4 m in length with a diameter of 0.235 m and entered Stand-1 with an initial speed of 0.14 m/s. Stand-1 can be described as a two roller stand with roll diameters of 606 mm, a pass depth of 60.3 mm, a rotation speed of 5.75 rpm, and a roll gap of 33.1 mm. Roller plastically deforms the bar producing both an elongation parallel to the rolling direction and changes the cross-sectional shape from round to oval. Prior to entering the roll stand, the initial temperatures for steel bar and roller were 1100 °C and 150 °C, respectively. Finite element meshing of both the steel bar and the rollers was accomplished using ABAQUS 6.12 (Fig. 10). The steel bar was built as a three-dimensional deformable part using 8-node brick element

(C3D8RT), and rollers were modeled as rigid parts using 4-node rigid element (R3D4). Friction behavior between contact pairs (roller and bar) was defined by Coulomb friction law with a friction coefficient 0.6 [18]. In order to describe viscoplastic behavior, a number of constitutive models for steel have been proposed in the last few decades [19]. Johnson-Cook (JC) model is one of most widely used phenomenological constitutive models that considers independently the effects of strain hardening, strain rate hardening, and temperature softening on flow stress. A Johnson-Cook model of steel grade 15V38 was built based on experimental stress-strain curves to serve as the material model for steel (Table 3) [18].

In the present study, the dynamic recrystallization model was coded in a user defined subroutine VUSDFLD of ABAQUS. For each increment of hot rolling simulation, simulated plastic strains of each node were updated and compared with calculated critical strain of the corresponding node. Once the plastic strain becomes larger than the critical strain, a dynamic recrystallization calculation is activated. The differential form of DRX is expressed as:

$$\mathrm{d}X_{DRX} = [-\exp(-\mathrm{k}\left(\frac{\varepsilon-\varepsilon_c}{\varepsilon_{pk}}\right)^n) \cdot (-\mathrm{kn}\left(\frac{\varepsilon-\varepsilon_c}{\varepsilon_{pk}}\right)^{n-1}) \cdot \frac{1}{\varepsilon_{pk}}]\mathrm{d}\varepsilon \qquad (13)$$

where critical strain ε_c and peak strain ε_{pk} were calculated based on the Z parameter of each node. After activation of dynamic recrystallization, the fraction of DRX is accumulated during deformation. If the plastic strain is larger than critical strain and strain rate is larger than zero, the fraction of DRX of each node is accumulated from the last increment:

$$X_{DRX}^{i+1} = X_{DRX}^{i} + \mathrm{d}X_{DRX}, \text{ if } \varepsilon^p > \varepsilon_c \text{ and } \dot{\varepsilon} > 0 \qquad (14)$$

Otherwise, fraction of DRX will remain the same as last increment:

$$X_{DRX}^{i+1} = X_{DRX}^{i}, \text{ if } \varepsilon^{p} < \varepsilon_{c} \text{ or } \dot{\varepsilon} = 0 \quad (15)$$

where strain rate $\dot{\varepsilon}$ is used to detect whether elements and nodes are under deformation. The flow chart of calculation process is shown in Fig. 11.

4. RESULTS AND DISCUSSION

4.1 VERIFICATION OF DYNAMIC RECRYSTALLIZATION MODEL

A dynamic recovery curve was calculated (Fig. 12) based on calculation of σ_{sat} and *r*. The difference between the dynamic recovery curve and experimental stress-strain curve is stress softening purely caused by dynamic recrystallization. Based on the literature [3], the fraction of DRX is 10% at peak stress, and 90% at stress equal to critical stress. In this study, the calculated fractions of DRX at the peak stress and the stress equal to the critical stress are 9.5% and 89.6%, which are very close to that reported in literature. Also, fractions of DRX at critical strain and steady state are treated as 0% and 100%, respectively. Based on critical strain, peak strain, *Z* parameter, and parameters *k* and *n*, a strain dependent model of dynamic recrystallization was built at different temperatures and different strain rates (Fig. 13). This dynamic recrystallization model was implemented into the finite element model. The developed dynamic recrystallization model and finite element model considered the practical hot rolling condition, including rolling temperature from 1000°C to 1200°C, strain rate from 0.01 s^{-1} and 1 s^{-1} , strain from 0 to 0.65. For single rolling pass under 1100°C, the temperature variation is from 1120°C to 1060°C.

4.2 DEFORMATION DURING HOT ROLLING

Hot rolling of a steel bar at 1100 °C was modeled based on industrial hot rolling condition. The dynamic recrystallization model developed in sections 3 and 4 was incorporated into a finite element model. The steel bar cross section was deformed from round to oval by a pair of horizontal rollers, and the calculated plastic strain and strain rate distributions of a cross section is plotted in Fig. 14. The cross section of steel bar was significantly reduced in the vertical direction with material flow into the rolling gap causing slight increase in the horizontal dimension. The maximum plastic strain located at the top and bottom areas of cross section, and the minimum plastic strain located at the sides. The rolling strain rate is from 0 to 1.35 s^{-1}.

4.3 DYNAMIC RECRYSTALLIZATION DURING HOT ROLLING

During hot rolling, dynamic recrystallization is activated due to sufficient plastic deformation. Investigation of dynamic recrystallization is critical to study steel product quality, microstructure evolution, and static recrystallization during hot rolling. Critical strain and equivalent plastic strain during hot rolling were investigated and the results are presented in Fig. 15. In Fig. 15a, the critical strain at each node is calculated based on temperature and strain rate condition. Critical strain is zero at the non-deformation area since the corresponding strain rate is zero. At the beginning of deformation, the surface of steel is deformed with large deformation and the critical strain quickly increases in the simulation. As rolling proceeds, the interior area starts to deform and the corresponding critical strain at the interior increases, while the surface critical strain decreased as strain rate decreased in the simulation. In Fig. 15b, the equivalent plastic strains are accumulated

throughout the deformation process. At the start of deformation, equivalent plastic strain of steel bar is relatively small and close to corresponding critical strain and a small amount of dynamic recrystallization is accomplished. As further rolling, the equivalent plastic strain increases rapidly due to large deformation and accumulating effect, providing sufficient energy for dynamic recrystallization.

Detailed comparisons between critical strain and equivalent plastic strain at surface and interior of steel bar are plotted in Fig. 16. At the surface, large deformation occurs and the equivalent plastic strain continuously increases from 0 to 0.5. Large dislocation density generated on the surface. The corresponding critical strain is in a low range of 0 to 0.2. Similarly, the internal equivalent plastic strain gradually increases from 0 to 0.5, and the internal critical strain increases to 0.2 before decreasing.

Once the dynamic recrystallization is onset, the fraction of DRX will accumulate during the deformation process. On the top and bottom surfaces of round bar (Fig. 16), significant deformation and plastic strain generate large dislocation density. Dynamic recrystallization initiates and accumulates by dislocation energy and relatively small critical strain. Conversely, at the center of round bar, plastic strain gradually increases. From node 1 to node 5 (Fig. 16), the plastic strain is very close to critical strain and minimal dynamic recrystallization is accumulated. From node 6 to node 10, the different between plastic strain and critical strain increases and dynamic crystallization accumulates significantly. Depending on the strain, strain rate, and temperature conditions of each node, the fraction of DRX at each node will be different even on the same cross section of steel bar (Fig. 17). The maximum fraction is located at the top and bottom areas, where strain and strain rate increase rapidly during deformation. The minimum fraction is at the side

region with minimal deformation. The fraction value is in the range of 7% to 41%, indicating that complete dynamic recrystallization is not accomplished during hot rolling due to very short deformation time (around 1 s).

Plastic strain exhibits significant influence on the fraction of DRX. During single pass simulation, the temperature and strain rate variation are small comparing with plastic strain. To investigate this strain effect, a comparison between fraction of DRX and equivalent plastic strain is plotted in Fig. 18. Due to symmetric shape, eleven nodes on a quarter of cross section are monitored to display strain effect on dynamic recrystallization. As equivalent plastic strain increases the fraction of DRX increases with a maximum in each at node 7. Results show that dynamic recrystallization is highly dependent on plastic strain, which reflects the extent of deformation.

4.4 TEMPERATURE EFFECT

Temperature is an important factor in dynamic recrystallization during hot rolling. However, temperature variation is relatively limited to one rolling pass due to the short deformation time. To study the effect of temperature on dynamic recrystallization, hot rolling processes with different rolling temperatures (1000 °C, 1100 °C, and 1200 °C) were modeled and simulated with DRX fraction plotted in Fig. 19. As rolling temperature increases, the fraction of DRX on whole cross section significantly increases. At 1000 °C, the fraction of DRX is in the range of 0 to 10%, while at 1200 °C, the fraction of DRX increases from 40% to 70%. Eleven nodes were monitored to display the variation of fraction at different rolling temperatures. At varying temperature, the maximum fraction always occurs at top and bottom area, and the minimum fraction occurs at side areas as

expected based upon the accumulated strain. At a temperature of 1000 °C, the fraction reaches maximum value at node 7, while at higher temperature 1200 °C, the fraction reaches maximum value at node 5. Results show that increasing rolling temperature increases the fraction of DRX of each node.

5. CONCLUSION

In the current study, a dynamic recrystallization model of steel grade 15V38 was built based on Gleeble hot compression tests. Critical strain, peak strain, and Zener-Hollomon parameter were calculated to construct a strain dependent equation of dynamic recrystallization. A three-dimensional nonlinear finite element model incorporating dynamic recrystallization model was built to simulate the practical hot rolling. Critical strains of each node during deformation were calculated and compared to equivalent plastic strains.

Experimental results showed that at low strain rate, significant dynamic crystallization occurs. The activation energy for dynamic recrystallization is calculated as 372 kJ/mol and the ratio of critical strain and peak strain is found as 0.42. The kinetics of dynamic recrystallization is model as Avrami equation. Based on experimental results, fraction of DRX at peak stress was calculated as 9.5% and fraction of DRX at stress equal to critical stress was calculated as 89.6%. The developed model shows good agreement with experimental data and available data in literature.

Simulation results show that for the entire deformation area except near the neutral point, equivalent plastic strains are larger than critical strain, indicating initiation of

dynamic recrystallization. The fraction of DRX after hot rolling was simulated and compared to the corresponding plastic strain of each node. Plastic strains exhibit significant positive correlation with fraction of DRX. The effect of temperature on fraction of DRX was investigated through modeling of hot rolling with different rolling temperatures. Results show that under the same deformation, high rolling temperature significantly increases the fraction of DRX of each node.

ACKNOWLEDGEMENTS

This work was supported by the Peaslee Steel Manufacturing Research Center at Missouri University of Science and Technology. The authors would like to thank Geary W. Ridenour and Eduardo Scheid from Gerdau-Fort Smith for technical input, and also Rafael Pizarro Sanz from Gerdau-Spain for Gleeble testing.

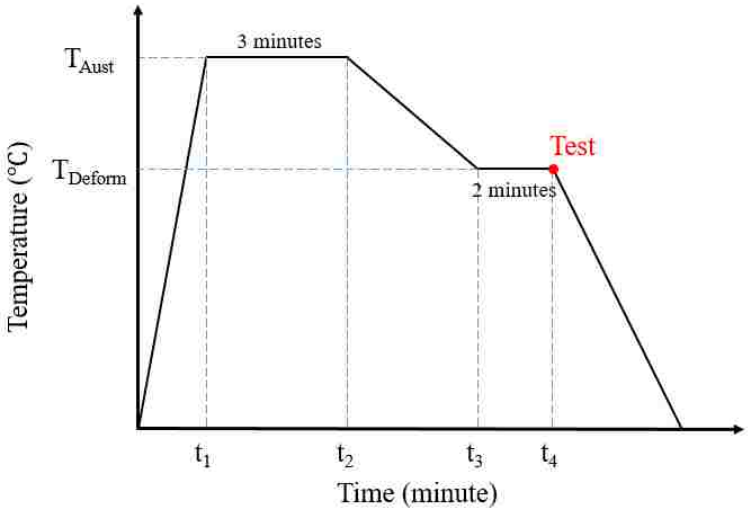

Fig. 1. Test profile for hot compression test

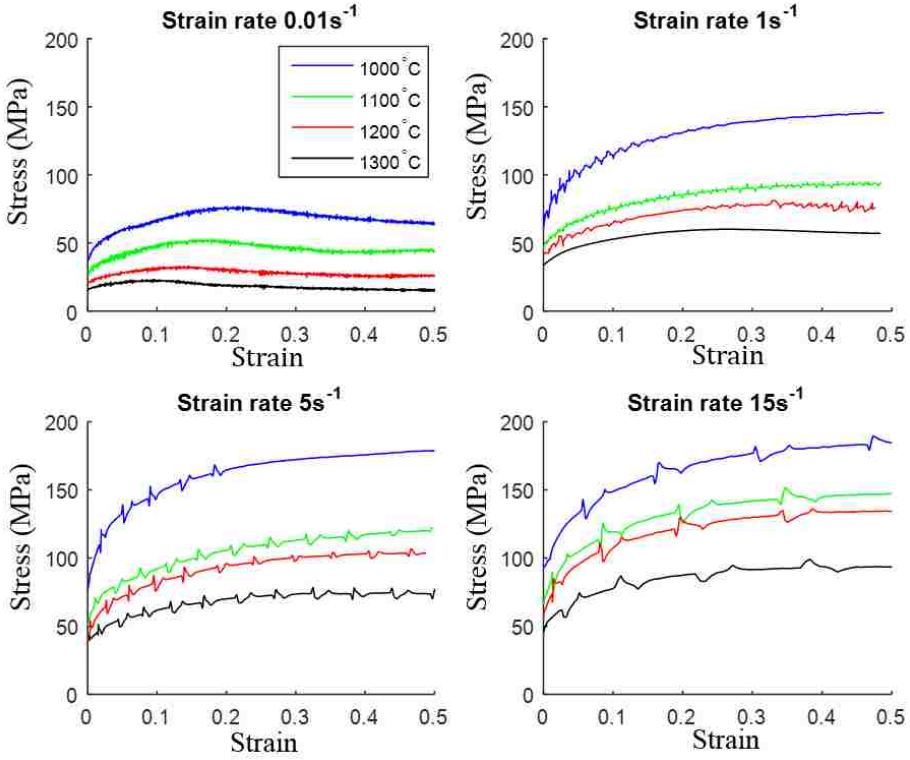

Fig. 2. Hot compression test results at varying strain rates and temperatures

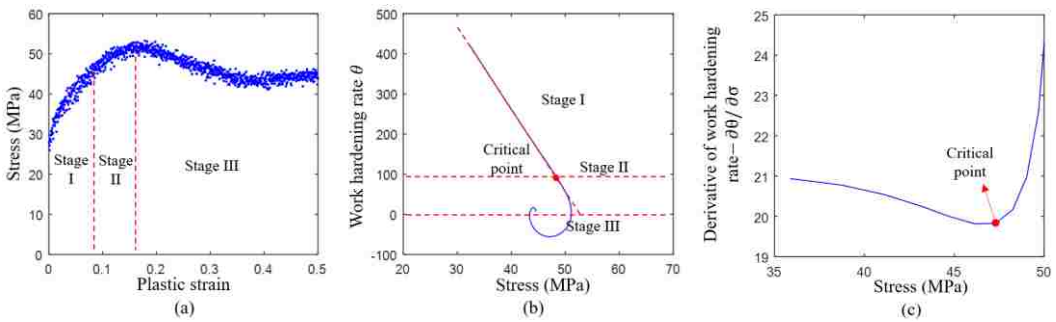

Fig. 3. Determination of critical strain: (a) raw stress-strain curve (1100° C and 0.01 s^{-1}), (b) work hardening curve, and (c) derivative of work hardening rate curve.

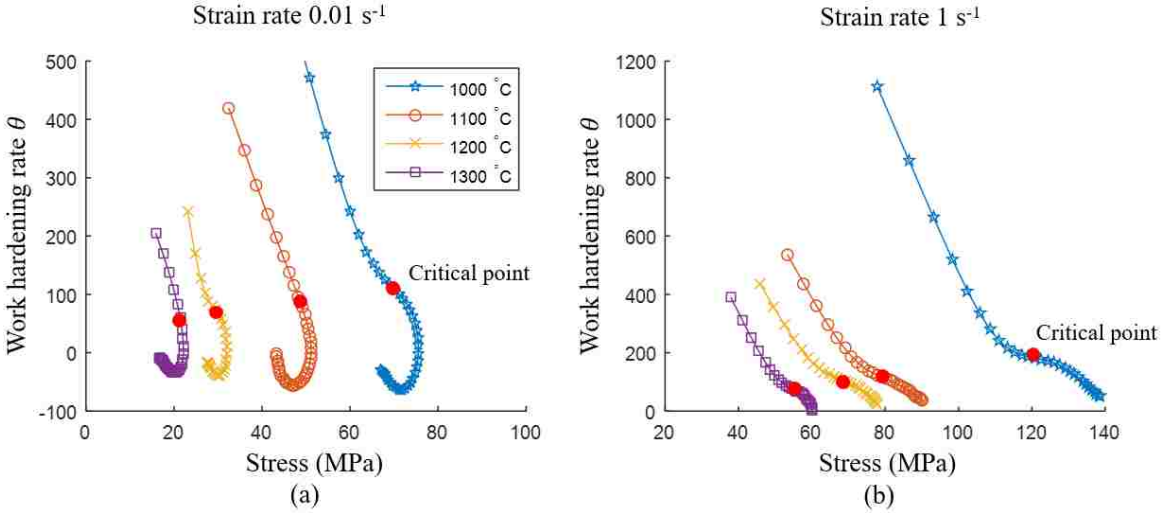

Fig. 4. Work hardening curve at low strain rates 0.01 s^{-1} and 1 s^{-1}

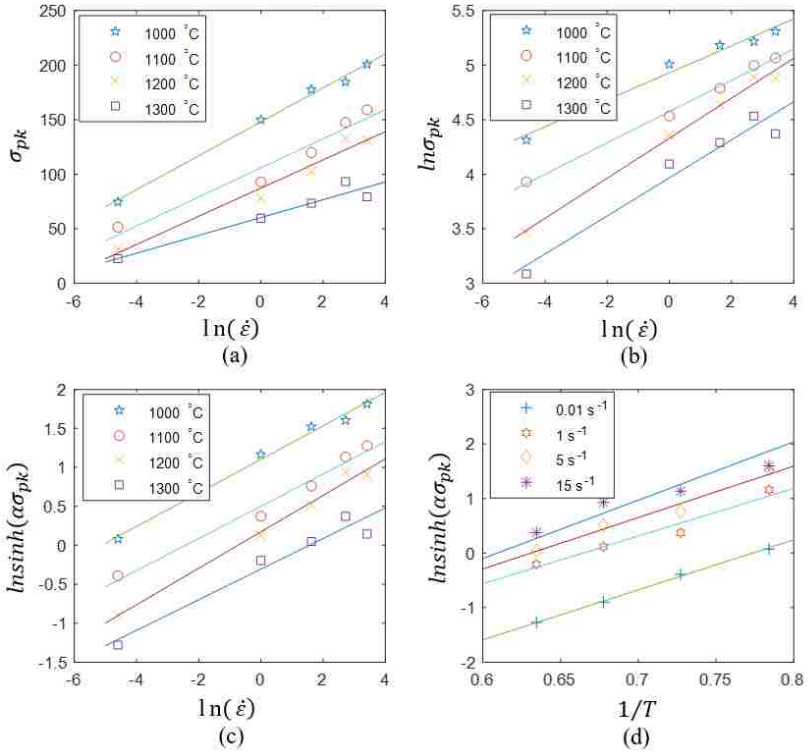

Fig. 5. Calculation of activation energy for deformation

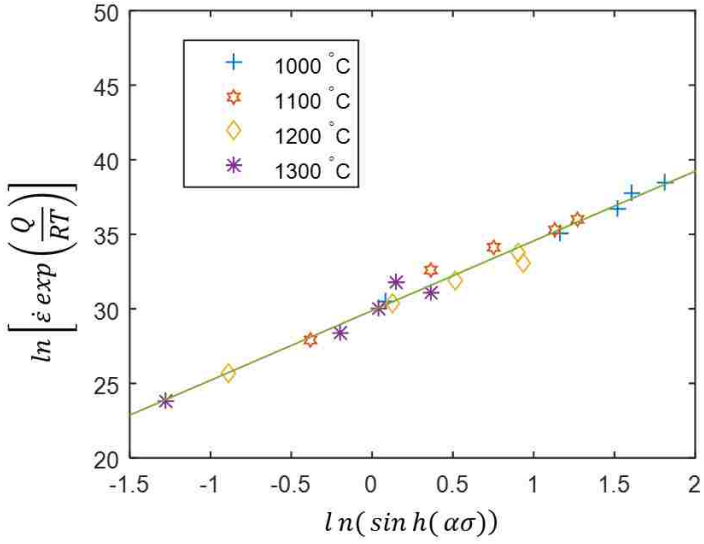

Fig. 6. Optimization of the values of activation energy Q and parameter n_0

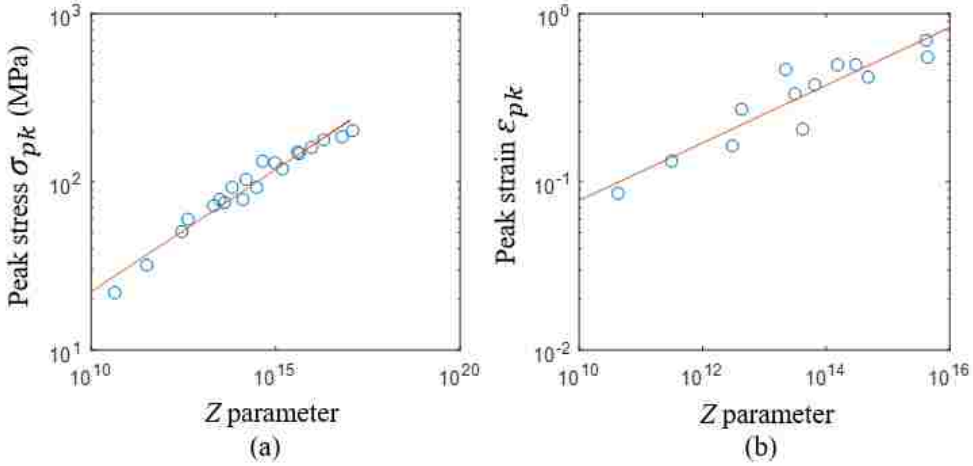

Fig. 7. Relationship between peak stress and peak strain vs. *Z* parameter

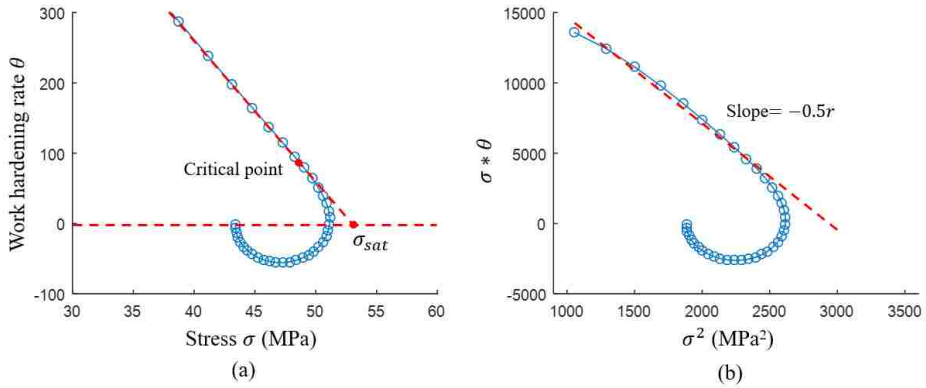

Fig. 8. Determination of rate of dynamic recovery: (a) calculation of the steady stress σ_{sat}, (b) calculation of the rate of dynamic recovery r

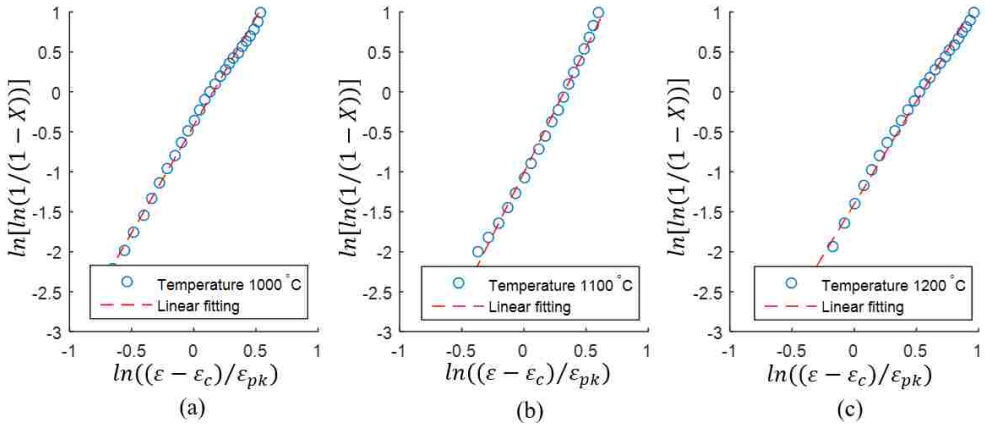

Fig. 9. Determination of parameters of dynamic recrystallization

Fig. 10. Modeling of steel bar hot rolling process

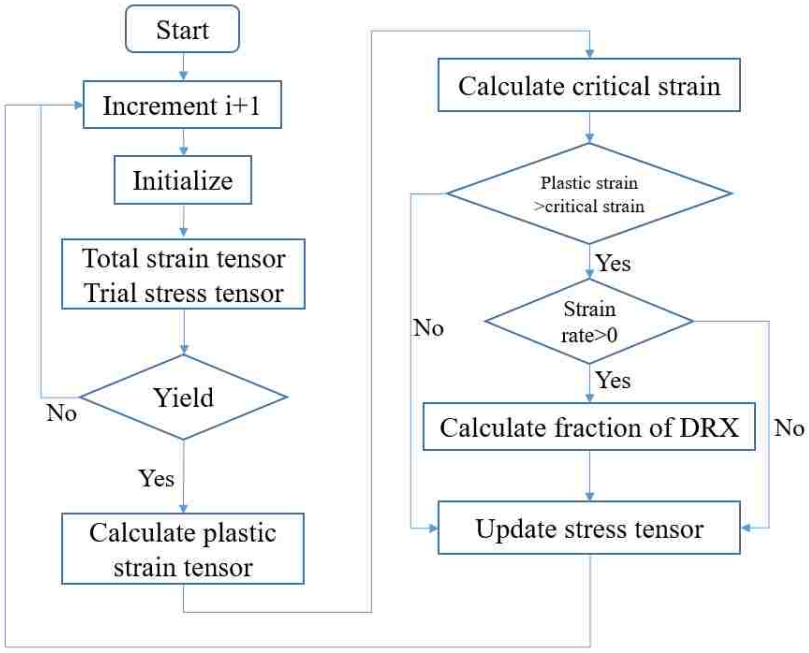

Fig. 11. Schematic of dynamic recrystallization calculation during hot rolling

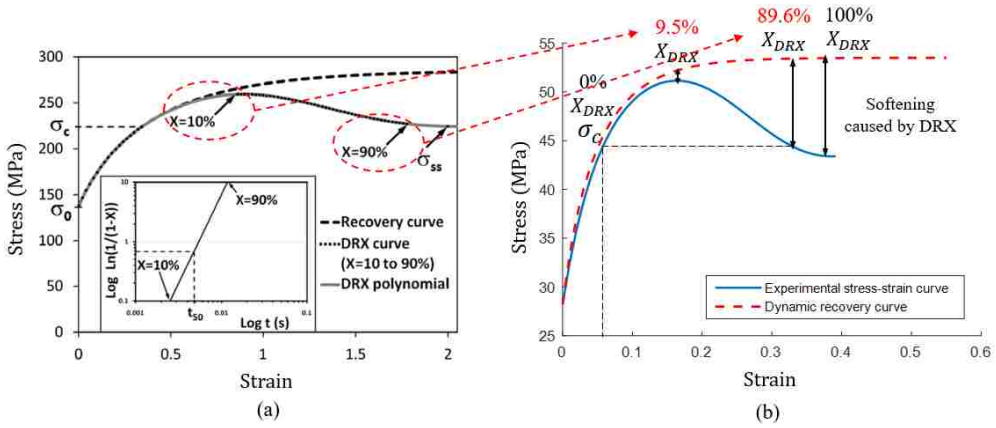

Fig. 12. Dynamic recovery curve and fraction of DRX (a) literature [3] (b) current study

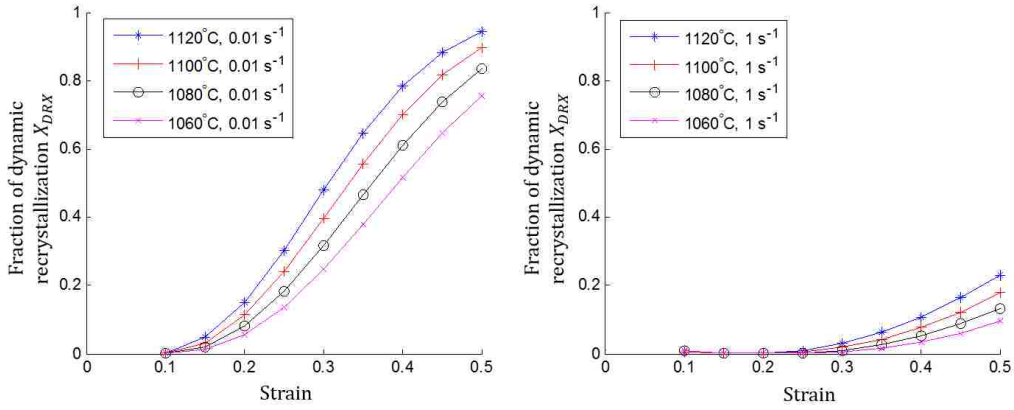

Fig. 13. Predictions of developed dynamic recrystallization model

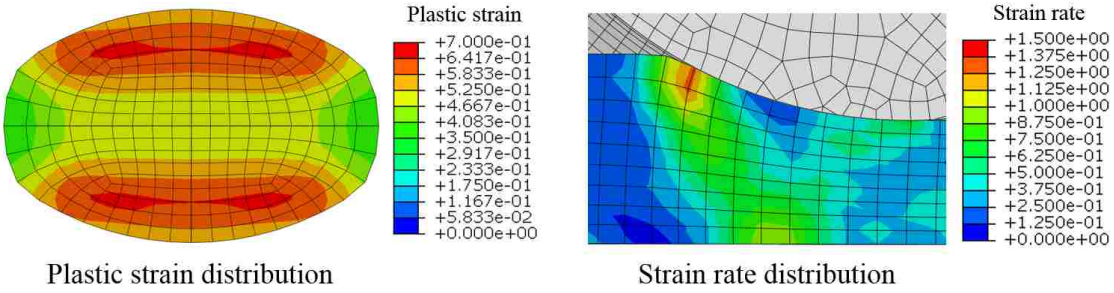

Fig. 14. Plastic strain distribution of steel cross section after hot rolling

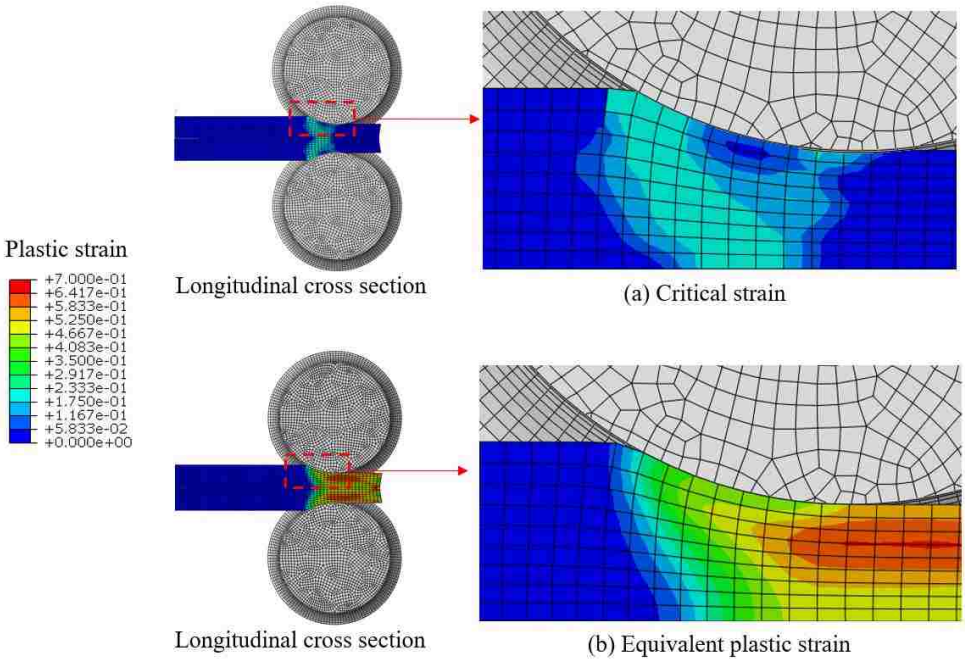

Fig. 15. Critical strain and equivalent plastic strain distribution during hot rolling

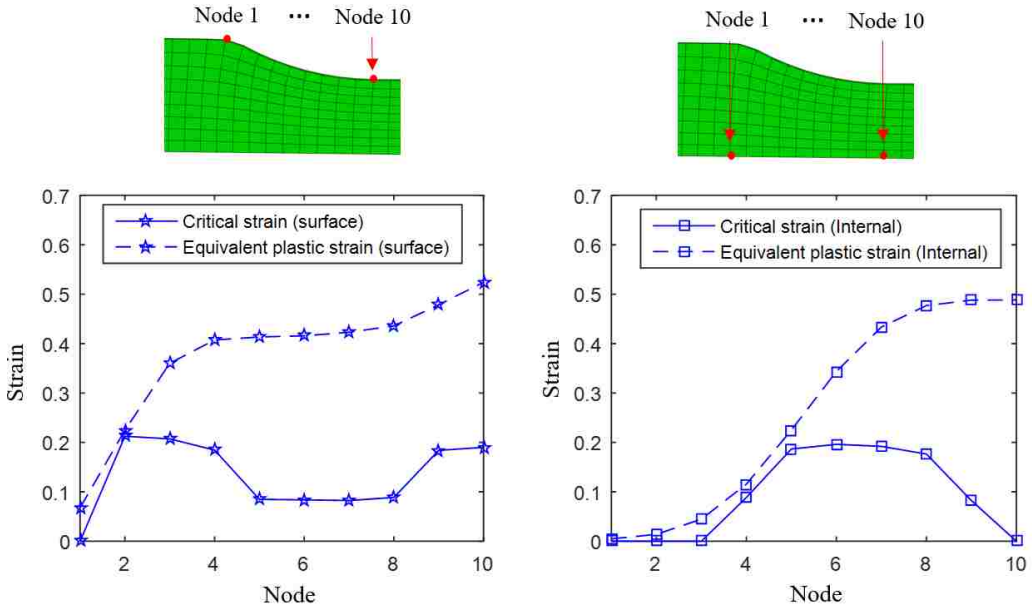

Fig. 16. Surface and internal critical strain and equivalent plastic strain distributions

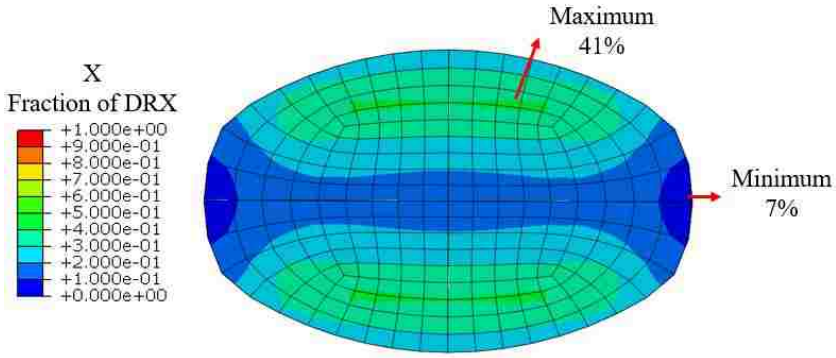

Fig. 17. Fraction of DRX after hot rolling

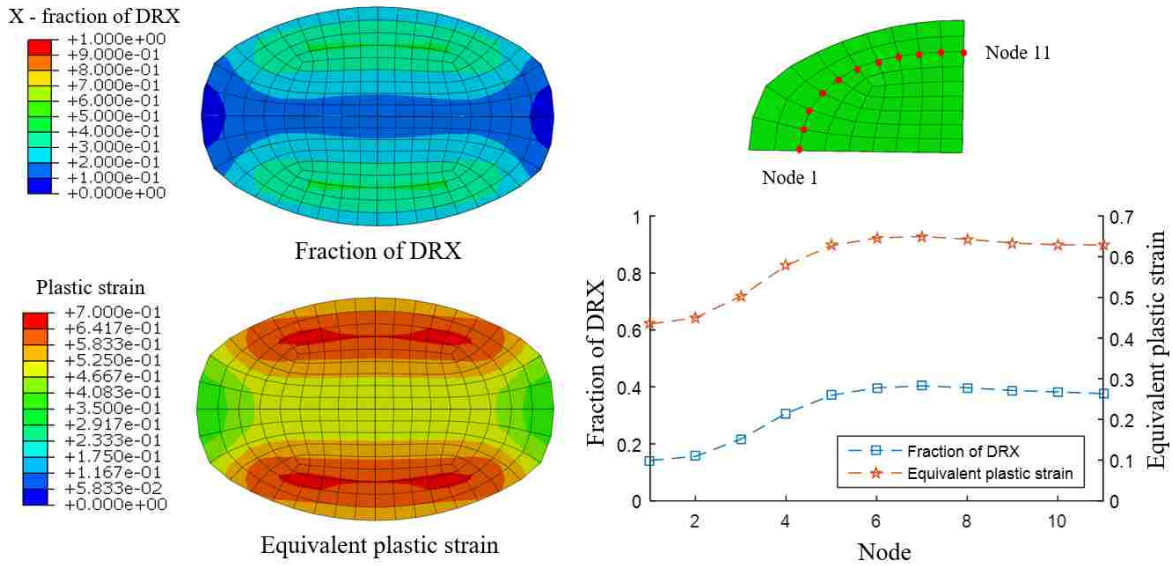

Fig. 18. Comparison between fraction of DRX and equivalent plastic strain

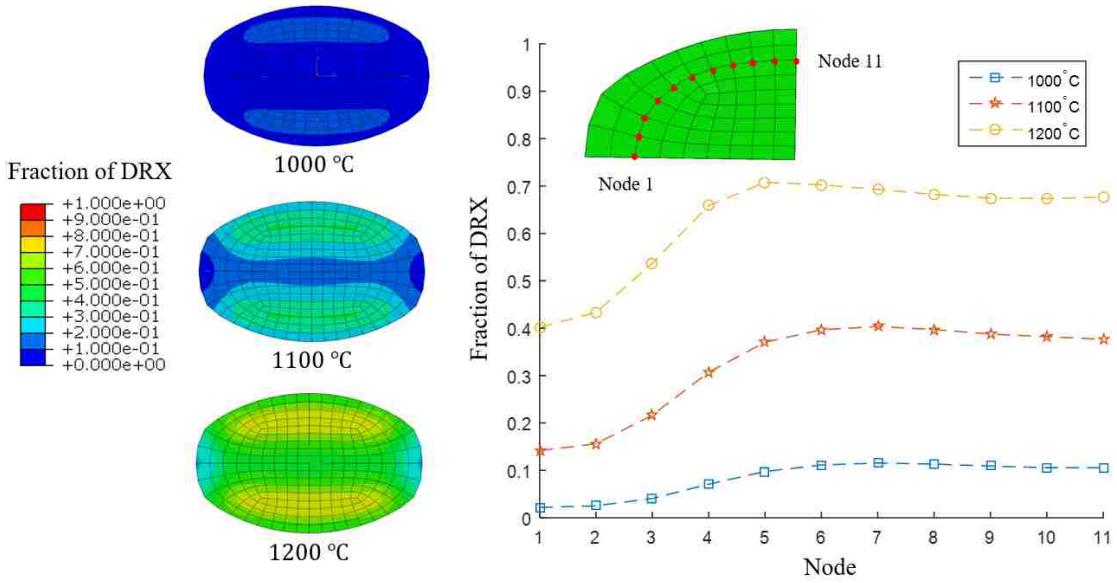

Fig. 19. Fraction of DRX at different rolling temperature

Table 1. Chemical composition of studied medium carbon alloyed steel

	C	Mn	Si	Cr	V	Al
mass %	0.38	1.3	0.57	0.13	0.08	0.018

Table 2. Determined parameters of relationships among peak stress, peak strain, critical strain, and Z parameter

	A_1	n_1	A_2	n_2	B_1
Value	0.783	0.145	0.00148	0.171	0.420

Table 3. Determined parameters of Johnson-Cook model

	A_{JC}	B_{JC}	C_{JC}	n_{JC}	m_{JC}
Value	71.59	105.03	0.12	0.39	0.95

REFERENCES

[1] C. M. Sellars, “Modelling microstructural development during hot rolling,” Mater. Sci. Technol., vol. 6, no. 11, pp. 1072–1081, 1990.

[2] E. I. Poliak and J. J. Jonas, “A one-parameter approach to determining the critical conditions for the initiation of dynamic recrystallization,” Acta Mater., vol. 44, no. 1, pp. 127–136, 1996.

[3] J. J. Jonas, X. Quelennec, L. Jiang, and É. Martin, “The Avrami kinetics of dynamic recrystallization,” Acta Mater., vol. 57, no. 9, pp. 2748–2756, 2009.

[4] A. Dehghan-Manshadi, M. R. Barnett, and P. D. Hodgson, “Hot deformation and recrystallization of austenitic stainless steel: Part I. dynamic recrystallization,” Metall. Mater. Trans. A Phys. Metall. Mater. Sci., vol. 39 A, no. 6, pp. 1359–1370, 2008.

[5] M. S. Chen, Y. C. Lin, and X. S. Ma, “The kinetics of dynamic recrystallization of 42CrMo steel,” Mater. Sci. Eng. A, vol. 556, pp. 260–266, 2012.

[6] T. Schambron, L. Chen, T. Gooch, A. Dehghan-Manshadi, and E. V. Pereloma, “Effect of Mo concentration on dynamic recrystallization behavior of low carbon microalloyed steels,” Steel Res. Int., vol. 84, no. 12, pp. 1191–1195, 2013.

[7] X. Chen, Y. C. Lin, D. Wen, J. Zhang, and M. He, “Dynamic recrystallization behavior of a typical nickel-based superalloy during hot deformation,” Mater. Des., vol. 57, pp. 568–577, 2014.

[8] R. C. Souza, E. S. Silva, A. M. Jorge, J. M. Cabrera, and O. Balancin, “Dynamic recovery and dynamic recrystallization competition on a Nb- and N-bearing austenitic stainless steel biomaterial: Influence of strain rate and temperature,” Mater. Sci. Eng. A, vol. 582, pp. 96–107, 2013.

[9] Y. Q. Ning, X. Luo, H. Q. Liang, H. Z. Guo, J. L. Zhang, and K. Tan, “Competition between dynamic recovery and recrystallization during hot deformation for TC18 titanium alloy,” Mater. Sci. Eng. A, vol. 635, pp. 77–85, 2015.

[10] X. Wang, Z. Liu, and H. Luo, “Complicated Interaction of Dynamic Recrystallization and Precipitation During Hot Deformation of Ultrahigh-Strength Stainless Steel,” Metall. Mater. Trans. A Phys. Metall. Mater. Sci., vol. 47, no. 12, pp. 6248–6258, 2016.

[11] F. Yin, L. Hua, H. Mao, X. Han, D. Qian, and R. Zhang, “Microstructural modeling and simulation for GCr15 steel during elevated temperature deformation,” Mater. Des., vol. 55, pp. 560–573, 2014.

[12] J. H. Bianchi and L. P. Karjalainen, “Modelling of dynamic and metadynamic recrystallisation during bar rolling of a medium carbon spring steel,” J. Mater. Process. Technol., vol. 160, no. 3, pp. 267–277, Mar. 2005.

[13] K. Li, P. Wang, G. Liu, P. Yuan, and Q. Zhang, “Development of simulation system for large H-beam hot rolling based on ABAQUS,” Int. J. Adv. Manuf. Technol., vol. 85, no. 5–8, pp. 1649–1663, 2016.

[14] H. Ding, K. Hirai, T. Homma, and S. Kamado, “Numerical simulation for microstructure evolution in AM50 Mg alloy during hot rolling,” Comput. Mater. Sci., vol. 47, no. 4, pp. 919–925, 2010.

[15] T. J. Baron, K. Khlopkov, T. Pretorius, D. Balzani, D. Brands, and J. Schröder, “Modeling of Microstructure Evolution with Dynamic Recrystallization in Finite Element Simulations of Martensitic Steel,” Steel Res. Int., vol. 87, no. 1, pp. 37–45, 2016.

[16] Y. X. Liu, Y. C. Lin, and Y. Zhou, “2D cellular automaton simulation of hot deformation behavior in a Ni-based superalloy under varying thermal-mechanical conditions,” Mater. Sci. Eng. A, vol. 691, no. January, pp. 88–99, 2017.

[17] Y. C. Lin, S. C. Luo, L. X. Yin, and J. Huang, “Microstructural evolution and high temperature flow behaviors of a homogenized Sr-modified Al-Si-Mg alloy,” J. Alloys Compd., vol. 739, pp. 590–599, 2018.

[18] X. Wang, K. Chandrashekhara, S. A. Rummel, S. Lekakh, D. C. Van Aken, and R. J. O. Malley, “Modeling of mass flow behavior of hot rolled low alloy steel based on combined Johnson-Cook and Zerilli- Armstrong model,” J. Mater. Sci., vol. 52, no. 5, pp. 2800–2815, 2017.

[19] Y. C. Lin and X. M. Chen, “A critical review of experimental results and constitutive descriptions for metals and alloys in hot working,” Mater. Des., vol. 32, no. 4, pp. 1733–1759, 2011.

IV. MODELING OF STATIC SOFTENING OF ALLOYED STEEL DURING HOT ROLLING BASED ON MODIFIED KINETICS

X. Wang and K. Chandrashekhara

Department of Mechanical and Aerospace Engineering

M. F. Buchely, S. Lekakh, D. C. Van Aken and R. J. O'Malley

Department of Materials Science and Engineering

Missouri University of Science and Technology, Rolla, MO 65409

ABSTRACT

Static softening is a crucial mechanism during hot rolling to relax residual stress and strain, refine microstructure, and improve steel thermo-mechanical properties. In this study, double hit tests with varying temperature, strain rate, interpass time, and pre-strains, were performed using Gleeble machine to investigate static softening behavior. Based on experimental results, a modified kinetics of static softening was developed to represent inerpass softening during hot rolling. Explicit subroutines of developed static softening model was developed and implemented into a three-dimensional finite element model of steel bar hot rolling. The static softening of round bar during hot rolling was simulated. The simulation results show that static softening occurs quickly in the beginning of interpass time and then slows down. Also, temperature and rolling speed effects on static softening were simulated and the results show that temperature has more significant influence on static softening that rolling speed.

1. INTRODUCTION

Static softening is a critical phenomenon during hot rolling. Due to static softening, the microstructure of steel grows equalized to gain both ductility and strength. Full static softening removes residual stress and strain generated at each pass of hot rolling. Investigation of static recrystallization is important for steel manufacturing to improve product quality. However, controlling static recrystallization is challenging during plant hot rolling and it is influenced by many parameters, such as rolling temperature, rolling speed, plastic deformation, and rolling time. Finite element method demonstrates advantages in investigation of static softening comparing with inefficient and costly plant trials.

Various studies were performed on static softening behavior. Andrade et al. [1] investigated precipitation effect on static recovery and static recrystallization, and provided methods to calculate fraction of static softening. Hodgson et al. [2, 3] studied the static softening effect on mechanical properties, and modeled the kinetics of static softening and microstructure evolution. Zurob et al. [4, 5] developed a comprehensive model considering recrystallization, recovery and precipitation to describe microstructure evolution during hot deformation. Also, mechanism maps were developed to predict the shape of softening curve. Zhang et al. [6] studied both dynamic and static softening behavior during multiple hot deformation of alloyed aluminum and the results showed static softening of 5182 alloy is more sensitive to deformation parameters, such as temperature and time, than 1050 and 7075 alloys. Najafizadeh et al. [7] performed double hit tests to investigate postdynamic recrystallization behavior in stainless steel, and the results showed that large pre-strain

significantly increase the speed the static softening. Jiang et al. [8] performed multistage hot deformation to investigate static softening behavior and found that static recovery is the main softening effect at temperature 300°C. Khoddam and Hodgson [9] proposed a revised method to represent static recrystallization behavior and the prediction of developed model showed better prediction than conventional model. These literatures on modeling of static softening provide technical backgrounds for the current study.

Hot rolling simulations considering static softening were performed by many researchers. Jung et al. [10] modeled steel bar hot rolling including static softening to predict the microstructure evolution. Yue et al. [11] developed three-dimensional finite element model to simulate rod hot rolling and related recrystallization behavior. The distribution of effective strain and temperature were simulated and verified by experimental data. He et al. [12] simulated multiple pass H-beam hot rolling considering microstructure evolution and recrystallization to optimize hot rolling process. Hore et al. [13] simulated microstructure evolution during static recrystallization in hot strip rolling process and the simulation results show good agreement with literature data. Besides simulation of hot rolling, plenty of simulations on microstructure are reported. Lin et al. [14] proposed a cellular automaton model to simulated microstructure during static recrystallization; Guvenc et al. [15] combined crystal plasticity finite element method and phase field method to simulate microstructure of static recrystallization; Orend et al. [16] developed a comprehensive method to model recrystallization during hot rolling. Among these studies, the simulation of static softening during multi-pass rod hot rolling is limited and it is necessary to perform corresponding investigation to optimize hot rolling schedule and improve product quality.

In the current study, double hit tests were performed to investigate static softening behavior. Interpass time, pre-strain, temperature, and strain rate effects on static softening were analyzed and plotted. A modified kinetics of static softening was built to simulate the round bar hot rolling. A three-dimension finite element model was developed to present a multi-pass hot rolling. The progress of static softening during hot rolling was studied, and the temperature and strain rate effects on static softening were simulated and investigated.

2. EXPERIMENTS – DOUBLE HIT TEST

A medium carbon alloyed steel 15V38 with chemical composition in mass % as shown in Table 1 was investigated in this study. Cylindrical specimens of 15 mm height and 10 mm diameter were machined from the as-cast steel bar. To investigate the static softening behavior, double hit tests are designed and performed using a Gleeble 3500 simulation system. Temperature (1000°C and 1100°C), pre-strain (0.1, 0.25, and 0.4), strain rate (1 s^{-1} and 5 s^{-1}), and interpass time (varies from 0.5s to 50s) were used as testing parameters according to industrial rolling condition.

The design of double hit test is shown in Fig. 1. Test specimens were heated up to 1150℃ with a heating rate of 260℃/minute. A hold of 5 minutes is then performed to anstenitizing and the specimen is cooled to desired testing temperature. An extra hold of 5 minutes is included to eliminate temperature gradient. The first hit was performed followed an interpass time before the second hit. Depending on the testing temperature, strain rate, and pre-strain, the interpass time will be different to present the kinetics of static softening. Under faster kinetics of static softening, the interpass time is chosen shorter to catch the

fraction of static softening; otherwise the interpass time is chosen longer. After the holding of interpass time, the second hit is performed with same temperature and strain rate of first hit.

To investigate specific parameter effect on static softening, three group of experiments were designed to investigate effects of interpass time, pre-strain, temperature, and strain rate (Table 2). In group 1, temperature and strain rate effect were tested under varying interpass time; in group 2 and 3, temperature and pre-strain effects were tested. Interpass-time effect was included in each group and testing sets.

3. MODELING OF STATIC SOFTENING

3.1 ANALYSIS OF EXPERIMENTAL STRESS-STRAIN CURVES

During double hit test, the first deformation produces a pre-strain on the specimen. Dynamic softening including dynamic recovery and dynamic recrystallization occurs during this deformation. After the first deformation, a holding for static softening is perform. The fraction of static softening depends on the testing temperature, strain rate, pre-strain during first deformation, and the holding time. The second deformation is then performed after the holding until reaching designed maximum strain 0.6. An example of raw experimental curve at temperature 1100°C, strain rate 1 s^{-1}, pre-strain 0.1, and interpass time 3s is shown in Fig. 2a.

In Fig. 2a, the first deformation was performed until plastic strain 0.1. The corresponding stress-strain curve exhibits a yield stress σ_o and a peak stress σ_m marked in red circle. After the first hit, a holding of 3 second was performed for static softening and

then second deformation was performed. The second stress-strain curve in Fig. 2a shows a new yield stress σ_r. Due to static softening during 3 seconds holding, peak stress σ_m at first stress-strain curve decreases to σ_r. The fraction of static softening is defined as

$$X = \frac{\sigma_m - \sigma_r}{\sigma_m - \sigma_o} \quad (1)$$

Under different testing conditions, *X* value varies from 0 to 100%. When the yield stress σ_r of second hit is equal to the peak stress σ_m of first hit, fraction of static softening is zero (*X*=0); when the yield stress σ_r is equal to the yield stress σ_o, the fraction of static softening is 100% (*X*=100%). Determination of these two yield stress is done by shifting second yield stress to the first yield stress (Fig. 2b). By shifting the second stress-strain curve (yellow line) to the first stress-strain curve (blue line), the elastic part of two overlaps and the two yield stresses are identified.

3.2 PARAMETER EFFECTS ON STATIC SOFTENING

Four parameters including time, temperature, strain rate, and pre-strain were considered in modeling of static softening. Interpass time effect is included in each test sets to plot the kinetics of time versus fraction of static softening. Experimental results of temperature 1000°C, strain rate 1 s^{-1}, pre-strain 0.25 and varying interpass time is shown in Fig. 3. The first deformation curves of these four tests are same since they were performed at same temperature and strain rate. During the first deformation, subgrains start to nucleate on the grain boundary and dislocation density increases with residual stress and strain. During the interpass time, these subgrain grows and dislocation density decreases to remove residual stress and strain. The second flow curves then show softening behavior depending on the length of interpass time.

The interpass time in Fig. 3 varies from 1s to 10s and generates four different second stress-strain curves (Fig. 4a). At short interpass time 1s, second stress strain curve is much higher than other second stress-strain curves, indicating small fraction of static softening and large amount of residual stress and strain is passed to second deformation. As interpass time increases to 3s, the second curve significantly decreases and close to first curve (Fig. 4a). At interpass time 5s and 10s, the second curve is almost overlap the first curve, showing nearly full static softening (Fig. 4a). A fraction of static softening is calculated at each interpass time, and then the kinetics of static softening at temperature 1000°C, strain rate 1 s^{-1}, pre-strain 0.25 is plotted in Fig. 4b.

Similarly, kinetics of static softening at other pre-strain, tempeature, and strain rate were calcualted and plotted in Fig. 5. According to practical rolling condition, temperature is chosen as 1000°C and 1100°C, strain rate is chosen as 1 s^{-1} and 5 s^{-1}, and pre-strain is chosen as from 0.1 to 0.4. In Fig. 5a, the temperature and strain rate are fixed at 1000°C and 1 s^{-1}, the pre-strain vaires from 0.1 to 0.4. As pre-strain increase, the fraction of static softening increases. Also, the slope of kinetics increases as pre-strain increases, because large pre-strain introduces significant dynamic recrystallization and nuclated grain, accelerating the kinetics of static softening during interpass time. In Fig. 5b, fraction of static softening increases as temperature increases from 1000°C to 1100°C. However, the change of X value caused by temperature is much smaller than pre-strain. Also, strain rate effect on fraction of static softening is similar to temperatue and is smaller than pre-strain effect. During hot rolling, large deformation occurs on steel product causing large plastic strain range, while the variation of temperature and strain rate in one signle pass is limited. Pre-strain demenstrates main effect on static softening.

3.3 MODELING OF KINETICS OF STATIC SOFTENING

Avrami equation is widely used to describe the kinetics of static softening:

$$X = 1 - \exp(k(\frac{t}{t_{0.5}})^n) \quad (2)$$

$$t_{0.5} = A\dot{\varepsilon}^p \varepsilon^q \exp(\frac{Q}{RT}) \quad (3)$$

where X is fraction of static softening, t is time, $t_{0.5}$ is the time when fraction of static softening reaches 50%, $\dot{\varepsilon}$ is strain rate, ε is strain, R is the gas constant 8.314 J/(molK), T is temperature, and Q is activation energy. Parameters k, n, A, p, and q are constants. $t_{0.5}$ at different pre-strain, temperature, and strain rate was directly determined from experimental results (Fig. 5). The kinetics parameter k and n is determined using nonlinear curve fitting based on experimental results (Fig. 6). Values of k and n are determined as 0.757 and 0.782, respectively.

However, the parameters k and n in traditional Avrami equation are constants, while the experimental results show that pre-strain has significant influence on the slope of kinetics, indicating that n value is a strain dependent value. A modified kinetics is proposed to address this shortcoming:

$$X = 1 - \exp(k(\frac{t}{t_{0.5}})^{n'}) \quad (4)$$

$$n' = f(\varepsilon) \quad (5)$$

where $f(\varepsilon)$ is strain effect on parameter n'. In the current study, linear relationship is used for $n' = f(\varepsilon)$. Values of n' are determined at strain 0.1, 0.25, and 0.4 separately, and $f(\varepsilon)$ is calculated as 1.718 ε +0.39 (Table 3). This modified kinetics of static softening model was implemented into finite element model.

4. FINITE ELEMENT MODELING

A nonlinear three-dimensional finite element model was developed to study hot rolling of a round steel bar. Four passes of a steel bar hot rolling, from P1 to P4, were modeled as continuous rolling process. The initial dimensions of the bar were 4 m in length with a diameter of 0.235 m and entered P1 with an initial speed of 0.14 m/s. The rolling information is shown in Table 4. The rolling information includes roller rotation speeds, roller diameters, pass depths, and roll gaps.

Each pass has one pair of rollers plastically deforming the steel bar from round to oval or from oval to round, producing an elongation parallel to the rolling direction. Prior to entering the rolling pass, the initial temperatures for steel bar and rollers were 1100 °C and 150 °C, respectively. The steel bar and the rollers were meshed using ABAQUS 6.12 (Fig. 7). The steel bar was built as a three-dimensional deformable part using 8-node brick element (C3D8RT), and rollers were modeled as rigid parts using 4-node rigid element (R3D4). Friction behavior between roller and bar was defined by Coulomb friction law with a friction coefficient 0.6 [17]. A Johnson-Cook model of steel grade 15V38 was built [17] based on experimental stress-strain curves and implemented into finite element model (Table 5).

In the present study, the static softening model was coded in a user defined subroutine VUSDFLD of ABAQUS. When the node just exit the rolling gap, the static softening calculation starts. For each calculation increment during the interpass time, the fraction of static softening of each node is updated by adding the increment of static softening:

$$dX = [-\exp(-k\left(\frac{t}{t_{0.5}}\right)^{n}) \cdot (-kn\left(\frac{t}{t_{0.5}}\right)^{n-1}) \cdot \frac{1}{t_{0.5}}]dt \quad (6)$$

$$X^{i} = X^{i-1} + dX \quad (7)$$

where dX is the increment of static softening, dt is time increment of each step, X^{i} is current accumulated fraction of static softening, and X^{i-1} is fraction of static softening at last step.

5. RESULTS AND DISCUSSION

5.1 VERIFICATION OF MODIFIED KINETICS OF STATIC SOFTENING

A modified Avrami equation was proposed to address the complicated strain effect on kinetics of static softening. The comparison between traditional model and modified model is shown in Fig. 8. The experimental results from double hit tests are shown by dot markers and the predictions of static softening models are represented by lines. In Fig. 8a, the traditional model predicts kinetics of static softening as fixed slope. At higher pre-strain 0.4, the experimental data shows significant quicker kinetics than prediction of traditional model while at low pre-strain 0.1 the experimental static softening is slower than prediction of traditional model. The predictions of modified model is shown in Fig. 8b. With modified *n* parameter considering pre-strain effect, the modified model shows better predictions than traditional model at both large and small pre-strain.

5.2 SIMULATION RESULTS OF STATIC SOFTENING

The deformation process during P1 is shown in Fig. 9. According to industrial hot rolling, the rolling temperature is set as 1100 °C. The cross section of steel bar was

deformed from round to oval and the corresponding plastic strain distribution is shown in Fig. 9. With significant deformation in vertical direction, the maximum plastic strain located at the top and bottom areas of cross section, and the minimum plastic strain located at the sides.

The corresponding static softening simulation results of P1 is shown in Fig. 10. As the steel was deformed by P1, the static softening started to accumulate. The interpass time between P1 and P2 is designed as 8s. The residual strain relaxes while the fraction of static softening increases. From 0s to 2s, the residual strain quickly relaxes from 0.6 to 0.1, and the fraction of static softening increases from 0 to above 50%. From 2s to 4s, the majority of fraction of static recrystallization reaches 80%, and from 4s to 8s, the progress of static softening slows down. The final residual strain after 8s varies from 0.017 to 0.05 and the final fraction of static softening varies from 86% to 98%. The pre-strain effect is also exhibited in Fig. 10. At large plastic strain areas, top and bottom areas, the fraction of static softening quickly increases to 90% in 2s, while the small pre-strain areas, the sides of bar, has a very slow softening speed, showing 86% softening at the end of interpass.

The static softening results of whole simulation from P1 to P4 are shown in Fig. 11. From P1 to P4, the rolling temperature decreases from 1100 °C to 1045 °C. Pre-strain and temperature show important influence during hot rolling. From round to oval at P1 and P3, the deformation and pre-strain are larger than deformation from oval to round at P2 and P4, causing larger fraction of static softening at P1 and P3. Also, due to higher temperature at P1 than P3, P1 exhibits larger fraction of static softening than other passes. From 0s to 8s, the fraction of static softening increases fast in large pre-strain areas and slow in small pre-strain areas. As rolling from P1 to P4, the rolling speed increases and interpass time

decreases. By comparing P1 at 8s and P4 at 6s, the fraction of static softening at P4 6s is much lower than P1 8s, causing significant residual stress. Increasing distance between passes and rolling temperature will help to increase the fraction of static softening.

5.3 TEMPERATURE AND ROLLING SPEED EFFECTS ON STATIC SOFTENING

To investigate the temperature effect on static softening during hot rolling, three rolling temperature including 1165 °C, 1065 °C, and 965 °C were used in simulating P2. The corresponding static softening and residual strain are shown in Fig. 12. As temperature decreases from 1165 °C to 965 °C, the fraction of static softening decreases and residual strain increases. From 1165 °C to 1065 °C, the change of static softening and residual strain is not significant: the fraction of static softening decreases to 83% and residual strain increases to 0.057, which is minimal for next pass. However, when temperature decreases to 965 °C, the fraction of static softening significantly decreases, and the minimal fraction of static softening is 50%. Also, the corresponding residual strain increases to 0.12, which will has impact on next pass.

On the other hand, roll speed effect on static softening was simulated. According to industrial rolling schedule, the rolling speed was chosen as 0.1 m/s and 0.3 m/s for P2. As it is mentioned in Fig. 5c, the strain rate has small influence on static softening when it was changed from 1 s^{-1} to 5 s^{-1}. The simulation results of rolling speeds 0.1 m/s and 0.3 m/s show very similar fraction of recrystallization. Both of them have similar fraction of static softening to Fig. 12b, and the variation among them is less than 5%. Therefore, comparing to rolling speed, temperature has more significant influence on static softening.

6. CONCLUSION

In the current study, double hit tests were performed to investigate the static softening behavior during multipass hot rolling. Parameters including interpass time, pre-strain, temperature, and strain rate are analyzed and the results showed that these parameters have significant influence on static softening. A modified kinetics model describing the static softening behavior during hot rolling was developed and implemented into a three-dimensional finite element model. The modified kinetics model of static softening shows better prediction than traditional model. The simulation results based on the developed modified kinetics was performed to simulate the softening progress of P1. Results show that static softening occurs very fast in the beginning 2s and then slow down until the end of interpass time. The final fraction of static softening during P1 is around 86%~98%, and the corresponding residual strain is as low as 0.05.Hot rolling from P1 to P4 was simulated and the results show that the P1 and P3 with vertical deformation causes higher fraction of static softening. Also, temperature exhibits more significant effect on static softening than rolling speed.

ACKNOWLEDGEMENTS

This work was supported by the Peaslee Steel Manufacturing Research Center at Missouri University of Science and Technology. The authors would like to thank Geary W. Ridenour and Eduardo Scheid from Gerdau-Fort Smith for technical input, and also Carolina Conter Elgert from Gerdau-Brazil for Gleeble testing.

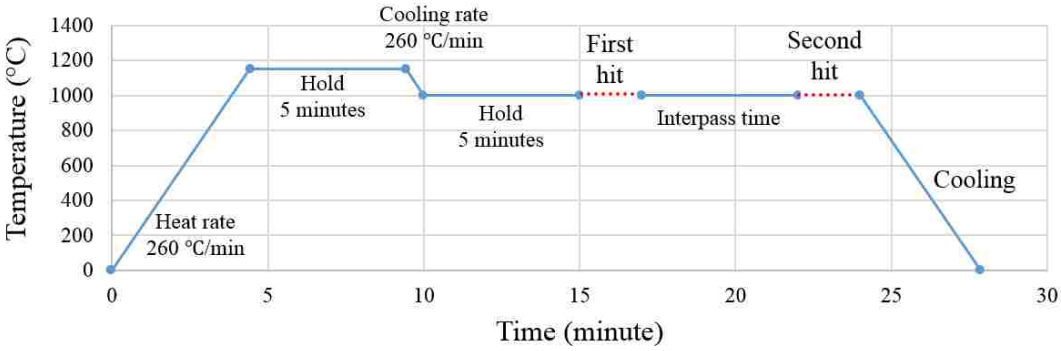

Fig. 1. The experimental design of double hit test procedure

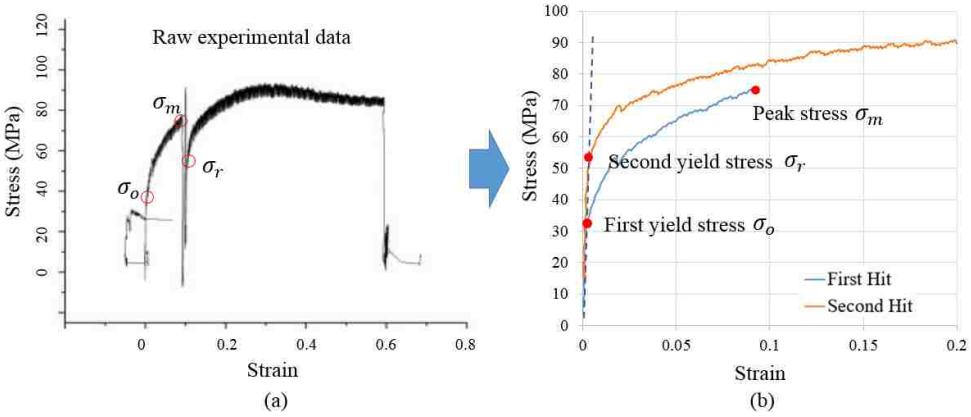

Fig. 2. Analysis of raw experimental results of double hit test

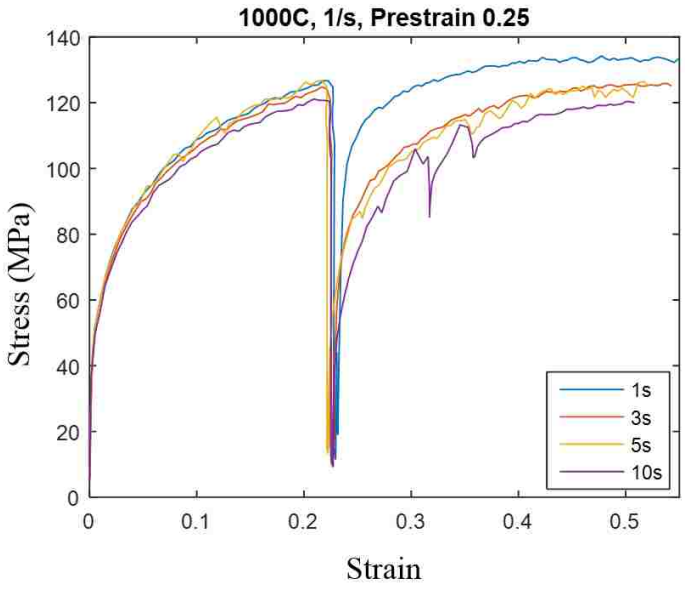

Fig. 3. Experimental results at temperature 1000°C, strain rate 1 s^{-1}, pre-strain 0.25, and varying interpass time

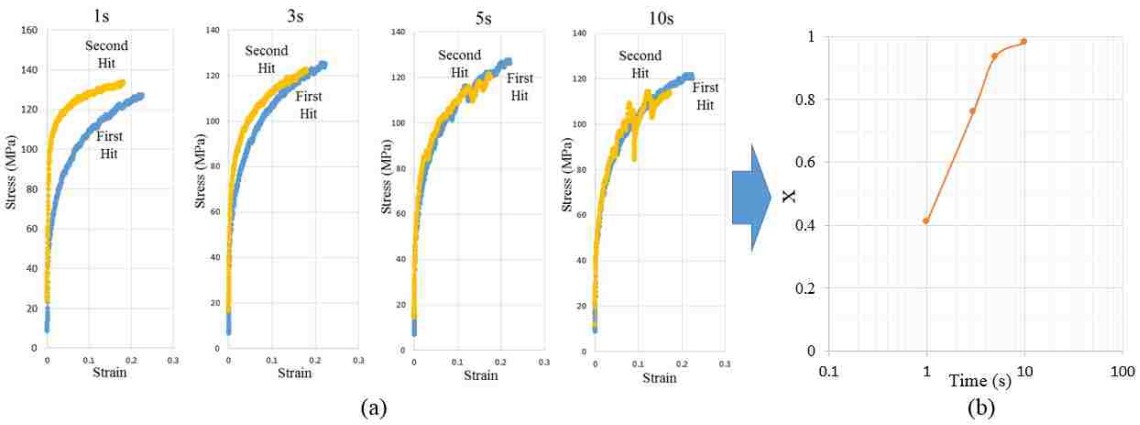

Fig. 4. Calculation of time effect on static softening

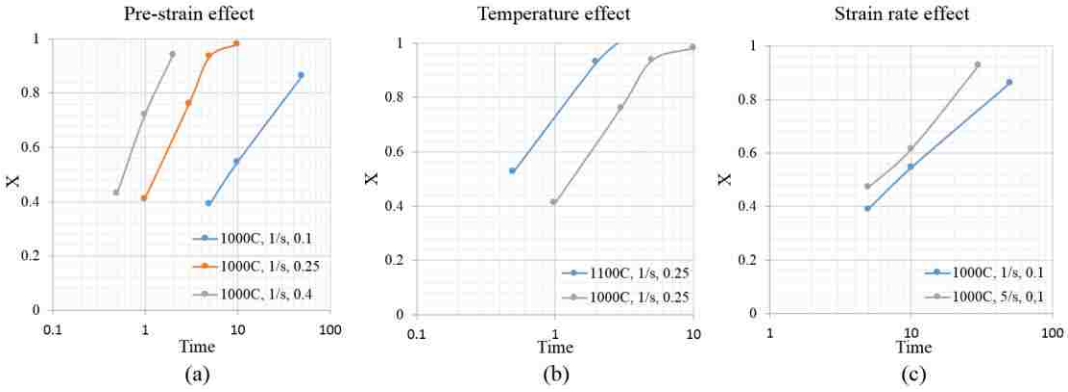

Fig. 5. Kinetics of static softening based on double hit test: (a) pre-strain effect, (b) temperature effect, and (c) strain rate effect

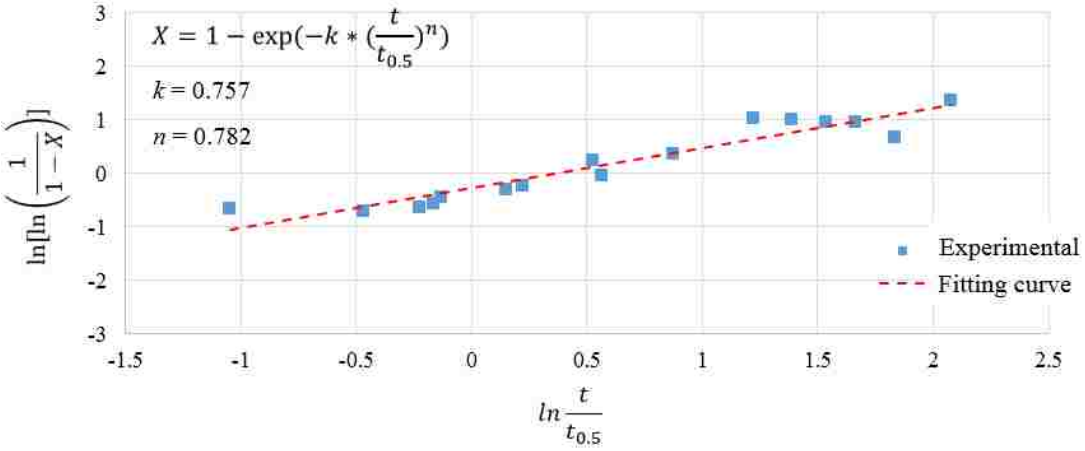

Fig. 6. Determination of kinetics parameters *k* and *n*

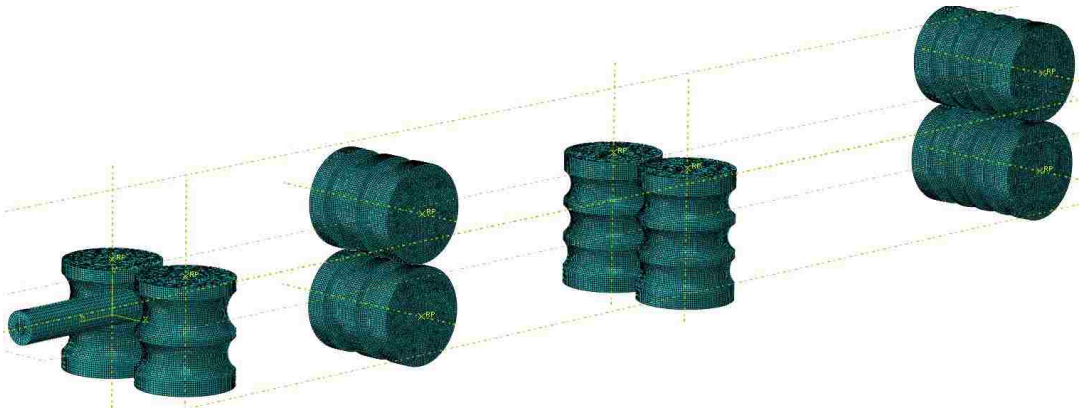

Fig. 7. Modeling of multi-pass steel bar hot rolling

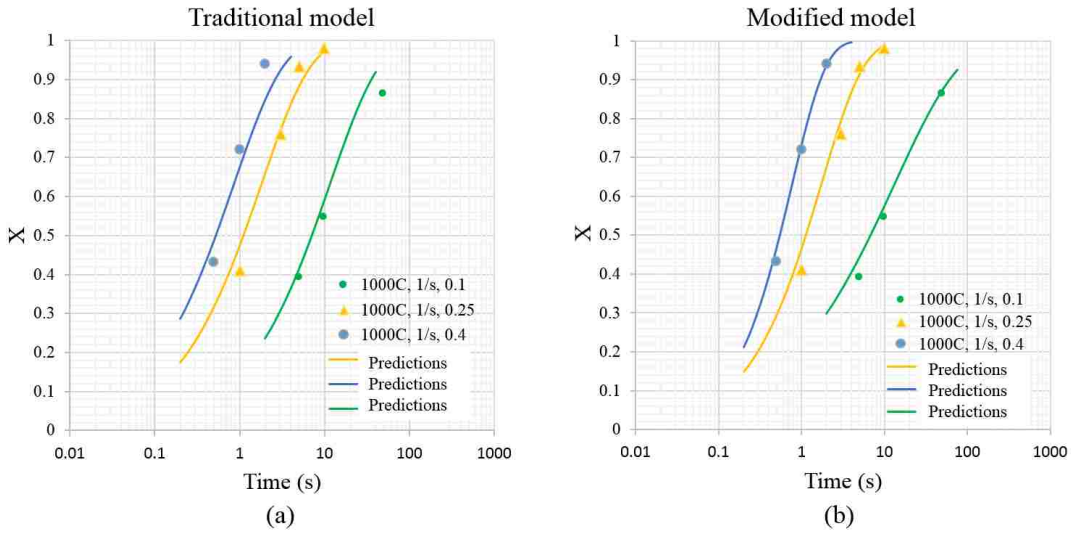

Fig. 8. Comparison between traditional model and modified model

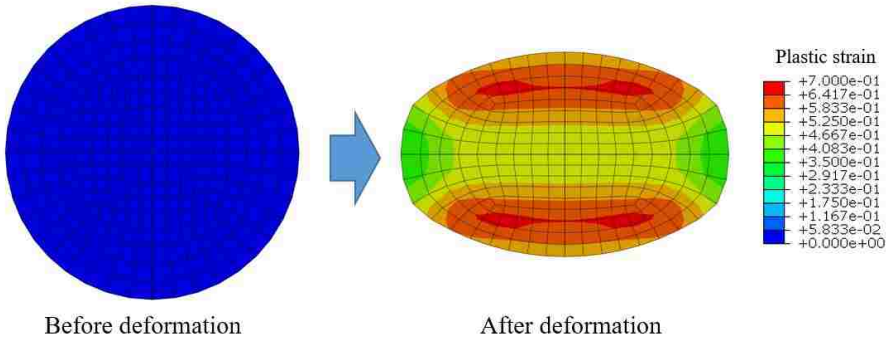

Fig. 9. Plastic strain distribution of steel cross section after hot rolling

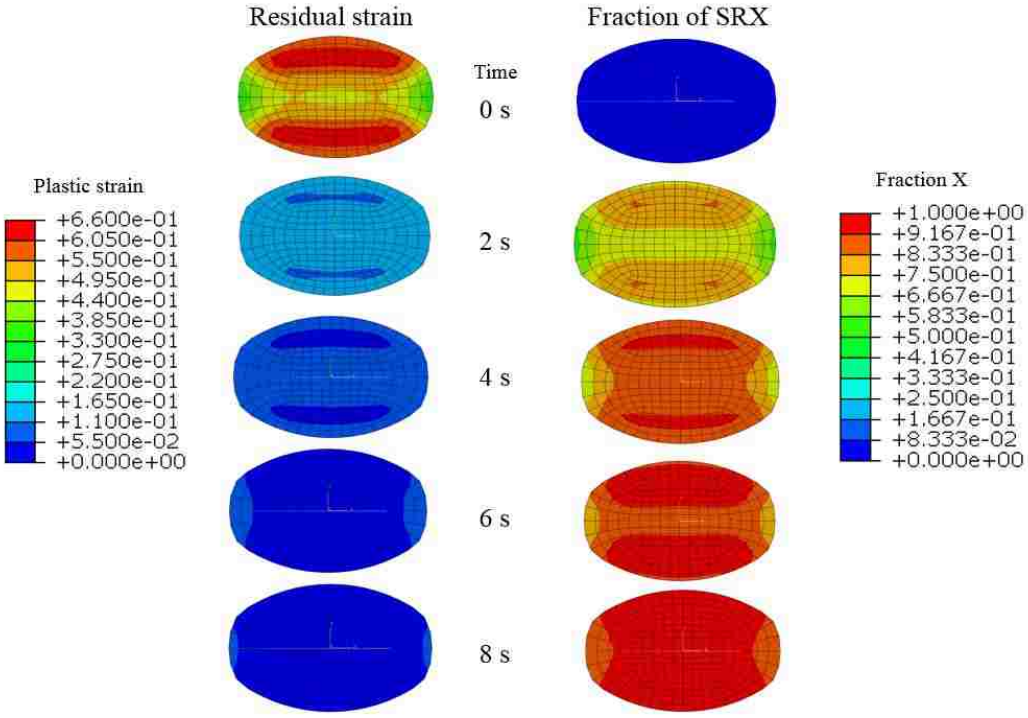

Fig. 10. Static softening progress after P1

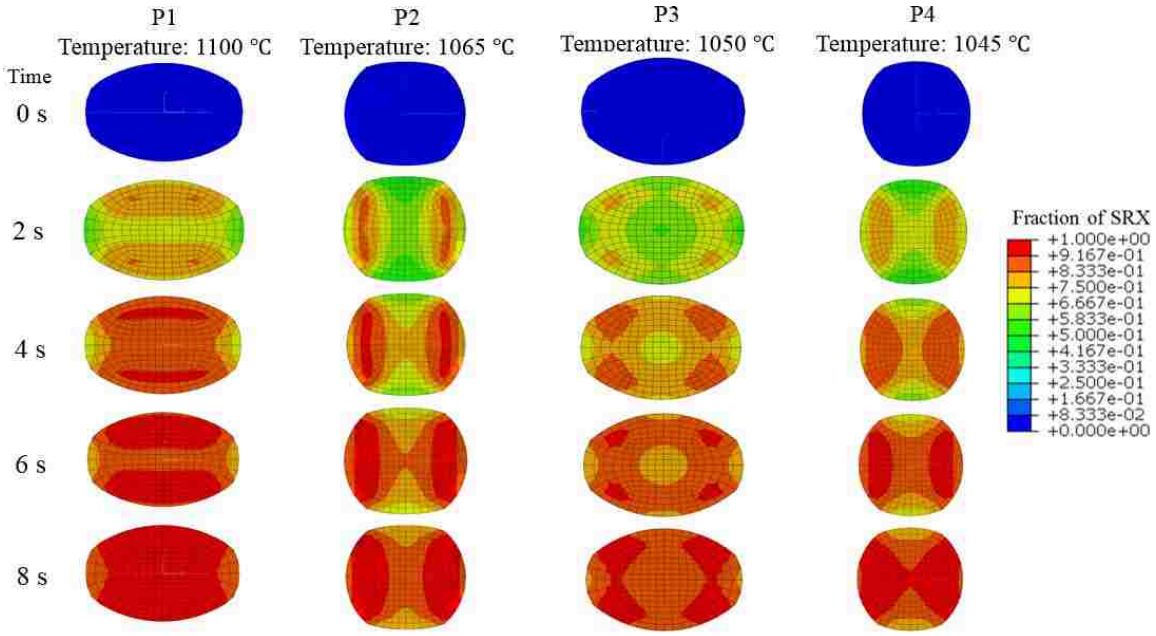

Fig. 11. Simulation results of static softening from P1 to P4

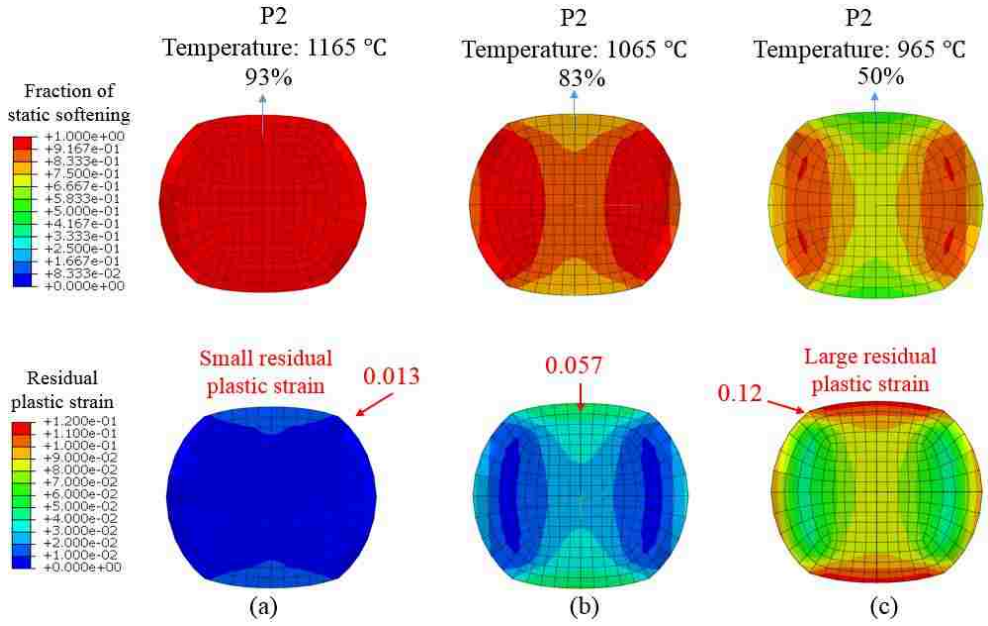

Fig. 12. Temperature effect on static softening during hot rolling

Table 1. Chemical composition of studied medium carbon alloyed steel

	C	Mn	Si	Cr	V	Al
mass %	0.38	1.3	0.57	0.13	0.08	0.018

Table 2. Experimental design of testing groups

	Temperature	Strain rate	Interpass time (s)	Pre-strain
Group 1	1100℃	1 s^{-1}	1, 3, 5, 10	0.1
	1100℃	5 s^{-1}	0.5, 1, 2, 3	
	1000℃	1 s^{-1}	5, 10, 30, 50	
	1000℃	5 s^{-1}	2, 5, 10, 30	
Group 2	1100℃	1 s^{-1}	0.5, 1, 2, 3	0.25
			0.5, 1, 1.5, 2	0.4
Group 3	1000℃	1 s^{-1}	1, 3, 5, 10	0.25
			0.5, 1, 2, 3	0.4

Table 3. Determination of parameter n' and $f(\varepsilon)$

Pre-strain	0.1	0.25	0.4
n'	0.5487	0.8456	1.064
$f(\varepsilon)$	1.718ε+0.39		

Table 4. Rolling parameters of four rolling passes

	Roller rotation speed (rpm)	Roller diameter (mm)	Pass depth (mm)	Rolling gap (mm)
P1	5.8	606	60.3	33.1
P2	7.2	590	79.4	26.5
P3	8.6	638	52.4	22.7
P4	10.3	649	66.7	8.76

Table 5. Determined parameters of Johnson-Cook model

	A_{JC}	B_{JC}	C_{JC}	n_{JC}	m_{JC}
Value	71.59	105.03	0.12	0.39	0.95

REFERENCES

[1] H. L. Andrade, M. G. Akben, and J. J. Jonas, “Effect of niobium, molybdenum and vanadium on static recovery and recrystallization in microalloyed steels,” Metall. Trans. A, vol. 14, no. October, pp. 1967–1977, 1983.

[2] P. D. Hodgson and R. K. Gibbs, “A Mathematical Model to Predict the Mechanical Properties of Hot Rolled C-Mn and Microalloyed Steels,” ISIJ Int., vol. 32, no. 12, pp. 1329–1338, 1992.

[3] P. D. Hodgson, “Microstructure modelling for property prediction and control,” J. Mater. Process. Technol., vol. 60, no. 1–4, pp. 27–33, 1996.

[4] H. S. Zurob, C. R. Hutchinson, Y. Brechet, and G. Purdy, “Modeling recrystallization of microalloyed austenite: effect of coupling recovery, precipitation and recrystallization,” Acta Mater., vol. 50, no. 12, pp. 3077–3094, 2002.

[5] H. S. Zurob, C. R. Hutchinson, Y. Brechet, and G. R. Purdy, “Rationalization of the softening and recrystallization behaviour of microalloyed austenite using mechanism maps,” Mater. Sci. Eng. A, vol. 382, no. 1–2, pp. 64–81, 2004.

[6] H. Zhang, G. Y. Lin, D. S. Peng, L. B. Yang, and Q. Q. Lin, “Dynamic and static softening behaviors of aluminum alloys during multistage hot deformation,” J. Mater. Process. Technol., vol. 148, no. 2, pp. 245–249, 2004.

[7] A. Najafizadeh, J. J. Jonas, G. R. Stewart, and E. I. Poliak, “The strain dependence of postdynamic recrystallization in 304 H stainless steel,” Metall. Mater. Trans. A, vol. 37, no. 6, pp. 1899–1906, 2006.

[8] F. Jiang, H. S. Zurob, G. R. Purdy, and H. Zhang, “Static softening following multistage hot deformation of 7150 aluminum alloy: Experiment and modeling,” Mater. Sci. Eng. A, vol. 648, pp. 164–177, 2015.

[9] S. Khoddam and P. D. Hodgson, “The need to revise the current methods to measure and assess static recrystallization behavior,” Mech. Mater., vol. 89, pp. 85–97, 2015.

[10] K. H. Jung, H. W. Lee, and Y. T. Im, “A microstructure evolution model for numerical prediction of austenite grain size distribution,” Int. J. Mech. Sci., vol. 52, no. 9, pp. 1136–1144, Sep. 2010.

[11] C. Yue, L. Zhang, J. Ruan, and H. Gao, “Modelling of recrystallization behavior and austenite grain size evolution during the hot rolling of GCr15 rod,” Appl. Math. Model., vol. 34, no. 9, pp. 2644–2653, Sep. 2010.

[12] Q. Q. He, J. Sun, J. Y. Zhao, B. M. Yuan, and L. J. Xu, “Numerical analysis of multi-pass h-beam hot rolling processing,” Appl. Mech. Mater., vol. 190–191, pp. 385–389, Jul. 2012.

[13] S. Hore, S. K. Das, S. Banerjee, and S. Mukherjee, “Computational modelling of static recrystallization and two dimensional microstructure evolution during hot strip rolling of advanced high strength steel,” J. Manuf. Process., vol. 17, pp. 78–87, 2015.

[14] Y. C. Lin, Y. X. Liu, M. S. Chen, M. H. Huang, X. Ma, and Z. L. Long, “Study of static recrystallization behavior in hot deformed Ni-based superalloy using cellular automaton model,” Mater. Des., vol. 99, pp. 107–114, 2016.

[15] O. Güvenç, M. Bambach, and G. Hirt, “Coupling of crystal plasticity finite element and phase field methods for the prediction of SRX kinetics after hot working,” Steel Res. Int., vol. 85, no. 6, pp. 999–1009, 2014.

[16] J. Orend, F. Hagemann, F. B. Klose, B. Maas, and H. Palkowski, “A new unified approach for modeling recrystallization during hot rolling of steel,” Mater. Sci. Eng. A, vol. 647, pp. 191–200, 2015.

[17] X. Wang, K. Chandrashekhara, S. A. Rummel, S. Lekakh, D. C. Van Aken, and R. J. O. Malley, “Modeling of mass flow behavior of hot rolled low alloy steel based on combined Johnson-Cook and Zerilli- Armstrong model,” J. Mater. Sci., vol. 52, no. 5, pp. 2800–2815, 2017.

SECTION

4. CONCLUSIONS

The first paper of this work provides an inverse finite element method to revise experimental stress-strain curves with barreling effect. Gleeble hot compression tests were performed and the specimens after compression exhibited significant barreling shape. The corresponding experimental stress-strain curves differs from actual material properties due to barreling. An inverse finite element analysis was performed and effectively modified experimental stress-strain curves to minimize the errors from barreling. Three parameters including friction coefficient, temperature, and strain rate were considered in parametric studies. The friction coefficient shows a significant effect on barreling and changes the experimental stress-strain curve. As friction decreases, the accuracy of experimental curve increases. On the other hand, as temperature increases the accuracy of experimental curve increases due to temperature softening effect. Strain rate shows complex influence on barreling. At lower strain rate, the barreling effect increases as strain rate increases, while at higher strain rate, the barreling effect decreases as strain rate increases. The presented studies can be used to modify experimental data and develop accurate material models for simulation.

The second paper developed a revised viscoplastic model to describe complex interacting effects of strain hardening, temperature softening, and strain rate hardening. Gleeble hot compression tests were performed at high temperature and varying strain rate. A traditional Johnson-Cook (JC) model, a traditional Zerilli-Armstrong (ZA) model, and a

combined JC and ZA model were developed based on experimental data. The combined JC and ZA model demonstrated better prediction on flow stress than traditional material models. A three-dimensional finite element model including developed material model was built to simulate round bar hot rolling. The simulation results show that the maximum plastic strain occurs at 45° and 135° areas of cross section. Plastic strain in x-direction and z-direction show compression and tension, respectively, while plastic strain in y-direction show combined compression and tension. Temperature demonstrates significant influence on stress distribution while the rolling speed has limited effect on stress. Due to temperature softening, the rolling torque decreases as temperature increases. Due to strain rate hardening, the rolling torque increases as rolling speed increase.

In the third paper, a dynamic recrystallization model was developed and implemented into finite element to simulation round bar hot rolling process. Based single hot compression tests, critical strain, peak strain, and Zener-Hollomon (Z) parameter were identified through analysis of work hardening curve. The activation energy for dynamic recrystallization is calculated as 372 kJ/mol and the ratio of critical strain and peak strain is found as 0.42. The dynamic recovery was also calibrated to determine the softening caused by dynamic recrystallization. The kinetics of dynamic recrystallization is model as Avrami equation and implemented into finite element model. The simulation results show that plastic stain during compression exceed critical strain for most area of steel bar, and the dynamic crystallization occurs during hot rolling. The maximum fraction of dynamic recrystallization reaches 41%, while the minimum value is 7% on the sides of bar cross section. Large plastic strain contributes to the large fraction of dynamic recrystallization. Also, the fraction of dynamic recrystallization increases as temperature increases.

In the fourth paper, static softening model was developed and implemented into finite element model. Double hit test was designed and performed at varying interpass time, pre-strain, temperature, and strain rate. A modified kinetics of static softening was developed to simulate a multi-pass hot rolling. The modified kinetics demonstrates better prediction than traditional kinetics comparing to experimental results. The simulation results showed that at the beginning of P1, static softening occurs quickly and then slows down in later interpass time. The final fraction of static softening during P1 is around 86%~98%, and the corresponding residual strain is 0.05, which is negligible for next pass. The simulation results from P1 to P4 show that the vertical deformation pass P1 and P3 have larger fraction of static softening than horizontal deformation pass P2 and P4. Also, the temperature and rolling speed effects on static softening were investigated and the results show that temperature has more significant effect on static softening than rolling speed.

BIBLIOGRAPHY

[1] G. R. Johnson and W. H. Cook, “A constitutive model and data for metals subjected to large strains, high strain rates and high temperatures,” 7th International Symposium on Ballistics, vol. 21, pp. 541–547, 1983.

[2] H. Zhang, W. Wen, and H. Cui, “Behaviors of IC10 alloy over a wide range of strain rates and temperatures: Experiments and modeling,” Materials Science and Engineering A, vol. 504, no. 1–2, pp. 99–103, 2009.

[3] Y. Lin, X. Chen, and G. Liu, “A modified Johnson–Cook model for tensile behaviors of typical high-strength alloy steel,” Materials Science and Engineering: A, vol. 527, no. 26, pp. 6980–6986, 2010.

[4] F. J. Zerilli and R. W. Armstrong, “Dislocation-mechanics-based constitutive relations for material dynamics calculations,” Journal of Applied Physics, vol. 61, no. 5, pp. 1816–1825, 1987.

[5] D. Samantaray, S. Mandal, and A. K. Bhaduri, “A comparative study on Johnson Cook, modified Zerilli–Armstrong and Arrhenius-type constitutive models to predict elevated temperature flow behaviour in modified 9Cr–1Mo steel,” Computational Materials Science, vol. 47, no. 2, pp. 568–576, 2009.

[6] D. Samantaray, S. Mandal, U. Borah, A. K. Bhaduri, and P. V. Sivaprasad, “A thermo-viscoplastic constitutive model to predict elevated-temperature flow behaviour in a titanium-modified austenitic stainless steel,” Materials Science and Engineering A, vol. 526, no. 1–2, pp. 1–6, 2009.

[7] Y. C. Lin and X. M. Chen, “A combined Johnson-Cook and Zerilli-Armstrong model for hot compressed typical high-strength alloy steel,” Computational Materials Science, vol. 49, no. 3, pp. 628–633, 2010.

[8] C. M. Sellars, “Modelling microstructural development during hot rolling,” Mater. Sci. Technol., vol. 6, no. 11, pp. 1072–1081, 1990.

[9] J. J. Jonas, X. Quelennec, L. Jiang, and É. Martin, “The Avrami kinetics of dynamic recrystallization,” Acta Mater., vol. 57, no. 9, pp. 2748–2756, 2009.

[10] A. Dehghan-Manshadi, M. R. Barnett, and P. D. Hodgson, “Hot deformation and recrystallization of austenitic stainless steel: Part I. dynamic recrystallization,” Metall. Mater. Trans. A Phys. Metall. Mater. Sci., vol. 39 A, no. 6, pp. 1359–1370, 2008.

[11] X. Chen, Y. C. Lin, D. Wen, J. Zhang, and M. He, “Dynamic recrystallization behavior of a typical nickel-based superalloy during hot deformation,” Mater. Des., vol. 57, pp. 568–577, 2014.

[12] T. Schambron, L. Chen, T. Gooch, A. Dehghan-Manshadi, and E. V. Pereloma, “Effect of Mo concentration on dynamic recrystallization behavior of low carbon microalloyed steels,” Steel Res. Int., vol. 84, no. 12, pp. 1191–1195, 2013.

[13] Y. L. Gao, X. X. Xue, and H. Yang, “Effect of Titanium on Hot Deformation Behaviors of Boron Microalloyed Steel,” vol. 56, no. 4, pp. 619–627, 2016.

[14] P. D. Hodgson and R. K. Gibbs, “A Mathematical Model to Predict the Mechanical Properties of Hot Rolled C-Mn and Microalloyed Steels,” ISIJ Int., vol. 32, no. 12, pp. 1329–1338, 1992.

[15] P. D. Hodgson, “Microstructure modelling for property prediction and control,” J. Mater. Process. Technol., vol. 60, no. 1–4, pp. 27–33, 1996.

[16] H. S. Zurob, C. R. Hutchinson, Y. Brechet, and G. Purdy, “Modeling recrystallization of microalloyed austenite: effect of coupling recovery, precipitation and recrystallization,” Acta Mater., vol. 50, no. 12, pp. 3077–3094, 2002.

[17] H. S. Zurob, C. R. Hutchinson, Y. Brechet, and G. R. Purdy, “Rationalization of the softening and recrystallization behaviour of microalloyed austenite using mechanism maps,” Mater. Sci. Eng. A, vol. 382, no. 1–2, pp. 64–81, 2004.

[18] S. Khoddam and P. D. Hodgson, “The need to revise the current methods to measure and assess static recrystallization behavior,” Mech. Mater., vol. 89, pp. 85–97, 2015.

[19] H. Zhang, G. Y. Lin, D. S. Peng, L. B. Yang, and Q. Q. Lin, “Dynamic and static softening behaviors of aluminum alloys during multistage hot deformation,” J. Mater. Process. Technol., vol. 148, no. 2, pp. 245–249, 2004.

[20] A. Najafizadeh, J. J. Jonas, G. R. Stewart, and E. I. Poliak, “The strain dependence of postdynamic recrystallization in 304 H stainless steel,” Metall. Mater. Trans. A, vol. 37, no. 6, pp. 1899–1906, 2006.

[21] S. Kim and Y. Im, “Three-dimensional finite element analysis of non-isothermal shape rolling,” Journal of Materials Processing Technology, vol. 127, pp. 57–63, 2002.

[22] X. Duan and T. Sheppard, “Three dimensional thermal mechanical coupled simulation during hot rolling of aluminium alloy 3003,” International Journal of Mechanical Sciences, vol. 44, pp. 2155–2172, 2002.

[23] H. Yang, M. Wang, L. Guo, and Z. Sun, “3D coupled thermo-mechanical FE modeling of blank size effects on the uniformity of strain and temperature distributions during hot rolling of titanium alloy large rings,” Computational Materials Science, vol. 44, no. 2, pp. 611–621, 2008.

[24] R. S. Nalawade, A. J. Puranik, G. Balachandran, K. N. Mahadik, and V. Balasubramanian, “Simulation of hot rolling deformation at intermediate passes and its industrial validity,” International Journal of Mechanical Sciences, vol. 77, pp. 8–16, 2013.

[25] D. Benasciutti, E. Brusa, and G. Bazzaro, “Finite elements prediction of thermal stresses in work roll of hot rolling mills,” Procedia Engineering, vol. 2, pp. 707–716, 2010.

[26] K. Li, P. Wang, G. Liu, P. Yuan, and Q. Zhang, “Development of simulation system for large H-beam hot rolling based on ABAQUS,” International Journal of Advanced Manufacturing Technology, vol. 85, no. 5, pp. 1649–1663, 2016.

[27] K. H. Jung, H. W. Lee, and Y. T. Im, “A microstructure evolution model for numerical prediction of austenite grain size distribution,” Int. J. Mech. Sci., vol. 52, no. 9, pp. 1136–1144, Sep. 2010.

[28] C. Yue, L. Zhang, J. Ruan, and H. Gao, “Modelling of recrystallization behavior and austenite grain size evolution during the hot rolling of GCr15 rod,” Appl. Math. Model., vol. 34, no. 9, pp. 2644–2653, Sep. 2010.

[29] Q. Q. He, J. Sun, J. Y. Zhao, B. M. Yuan, and L. J. Xu, “Numerical analysis of multi-pass h-beam hot rolling processing,” Appl. Mech. Mater., vol. 190–191, pp. 385–389, Jul. 2012.

[30] S. Hore, S. K. Das, S. Banerjee, and S. Mukherjee, “Computational modelling of static recrystallization and two dimensional microstructure evolution during hot strip rolling of advanced high strength steel,” J. Manuf. Process., vol. 17, pp. 78–87, 2015.

[31] J. Orend, F. Hagemann, F. B. Klose, B. Maas, and H. Palkowski, “A new unified approach for modeling recrystallization during hot rolling of steel,” Mater. Sci. Eng. A, vol. 647, pp. 191–200, 2015.

VITA

Mr. Xin Wang was born in Qingzhou, Shandong, the People's Republic of China. He was admitted to Beijing Institute of Technology, Beijing, China in 2006 and received his B.S. degree in Mechanical Engineering in 2010. After that, he began his graduate study in Beijing Institute of Technology, Beijing, China and received his M.S. degree in Mechanical Engineering in 2013.

Since August 2013, Mr. Xin Wang has been enrolled in the Ph.D. Program in Mechanical Engineering at Missouri University of Science and Technology, Rolla, Missouri, USA. He has served as Graduate Research Assistant between August 2013 and May 2018 in the Department of Mechanical and Aerospace Engineering. In May 2018, he received his Ph.D. degree in Mechanical Engineering from Missouri University of Science and Technology, Rolla, Missouri.